Exciting the Low Permittivity Dielectric Resonator Antenna Using Tall Microstrip Line Feeding Structure and Applications

A Thesis

Submitted to the College of Graduate Studies and Research

in Partial Fulfillment of the Requirements

for the Degree of

Master of Science

in the Department of Electrical Engineering

University of Saskatchewan

Saskatoon

By

Xun Liu (Diamond Leo)

PERMISSION TO USE

In presenting this thesis in partial fulfilment of the requirements for a Postgraduate degree from the University of Saskatchewan, I agree that the Libraries of this University may make it freely available for inspection. I further agree that permission for copying of this thesis in any manner, in whole or in part, for scholarly purposes may be granted by the professor or professors who supervised my thesis work or, in their absence, by the Head of the Department or the Dean of the College in which my thesis work was done. It is understood that any copying or publication or use of this thesis or parts thereof for financial gain shall not be allowed without my written permission. It is also understood that due recognition shall be given to me and to the University of Saskatchewan in any scholarly use which may be made of any material in my thesis.

Requests for permission to copy or to make other use of material in this thesis in whole or part should be addressed to:

Head of the Department of Electrical Engineering

University of Saskatchewan

Saskatoon, Saskatchewan S7N 5A9

ABSTRACT

The development of wireless communications increases the challenges on antenna performance to improve the capability of the whole system. New fabrication technologies are emerging that not only can improve the performance of components but also provide more options for materials and geometries. One of the advanced technologies, referred to as deep X-ray lithography (XRL), can improve the performance of RF components while providing interesting opportunities for fabrication.

Since this fabrication technology enables the objects of high aspect ratio (tall) structure with high accuracy, it offers RF/microwave components some unique advantages, such as higher coupling energy and compacted size. The research presented in that thesis investigates the properties of deep XRL fabricated tall microstrip transmission line and describes some important features such as characteristic impedance, attenuation, and electromagnetic field distribution. Furthermore, since most of traditional feeding structure cannot supply enough coupling energy to excite the low permittivity DRA element ($\varepsilon_r \leq 10$), three novel feeding schemes composed by tall microstrip line on exciting dielectric resonator antennas (DRA) with low permittivity are proposed and analyzed in this research. Both simulation and experimental measured results exhibit excellent performance.

Additionally, a new simulation approach to realize Dolph-Chebyshev linear series-fed DRA arrays by using the advantages of tall microstrip line feeding structure is proposed. By using a

novel T shape feeding scheme, the array exhibits wide band operation due to the low permittivity (ε_r=5) DRA elements and good radiation pattern due to the novel feeding structure. The tall metal transmission line feed structure and the polymer-based DRA elements could be fabricated in a common process by the deep XRL technology.

This thesis firstly illustrates properties and knowledge for both DRA element and the tall transmission line. Then the three novel feeding schemes by using the tall transmission line on exciting the low permittivity DRA are proposed and one of the feeding structures, side coupling feeding, is analyzed through the simulation and experiments. Finally, the T shape feeding structure is applied into low permittivity linear DRA array design work. A novel method on designing the Dolph-Chebyshev array is proposed making the design work more efficient.

ACKNOWLEDGMENTS

I would like to acknowledge my genuine gratitude to my supervising professor, Dr. David M. Klymyshyn for his valuable support, assistance throughout the whole research and preparation of this thesis with his patience and knowledge during my M.Sc program at the University of Saskatchewan.

Also, I would like to appreciate my parents Luya Ma and Hongtao Liu, my wife Hengli, for their persistent encouragement and support throughout my M.Sc program.

Contents

List of Tables

List of Figures

LIST OF ABBREVIATIONS

CPW – Coplanar Waveguide

DXRL – Deep X-Ray Lithography

EBG – Electromagnetic Band-Gap

FEM – Finite Element Method

HFSS – High Frequency Structure Simulator

HVAR – High Vertical Aspect Ratio

KIT – Karlsruhe Institute of Technology

LIGA – Roentgen-Lithography Galvanik Abformung (German for "X-ray Lithography Electrodeposition Moulding")

MEMS – Micro-Electro-Mechanical Systems

PMMA – Poly-Methyl-Methacrylate

RF – Radio Frequency

RIE – Reactive Ion Etching

SEM – Scanning Electron Microscopy

SyLMAND –Synchrotron Laboratory for Micro and Nano Devices

TEM – Transverse ElectroMagnetic

TE – Transverse Electric

TM – Transverse Magnetic

VNA – Vector Network Analyzer

Chapter 1
Introduction

1.1 Background and Motivation

1.1.1 Background Introduction

Nowadays, people cannot survive in the fast-paced and modern world without communication tools. Meanwhile, modern communication technology has transitioned from hulking analog devices to smart digital devices with the development of high technology. Recent advanced communication applications such as the satellite communication, military, national security or radar have been thrust toward microwave or millimeter-wave frequency bands due to the severe overcrowding in the electromagnetic spectrum resource. Correspondingly, it also raises many challenges on antenna performance, such as high gain, wide-band application, high power efficiency, high power handling, and so on. Improving the performance of the antenna becomes one necessary and difficult task.

For fulfilling these demands, the dielectric resonator antenna (DRA) was proposed in the 1980s to cover from lower frequency commercial bands to higher frequency military bands [1]. It is one type of microwave resonating structure composed of ceramic material and mounted on the ground plane. Fields are not contained in the resonator but radiate outside. Since the DRA has many excellent advantages over the other traditional antennas, such as low loss, high gain, and ease of circuit integration, it has became popular to be utilized into designing high performance

transceivers and improving the performance of the communication system.

1.1.2 Motivation

Currently, difficult problems accompany the development of wireless communication technology, such as size miniaturization, performance improvement, high level integration, cost reduction, and effective fabrication feasibility. Among these different challenges, component size and performance are an important trade-off when comparing wireless devices, and also a design priority. Many researchers put efforts on miniaturization as well as performance enhancement, using approaches such as Electromagnetic Band-Gap (EBG) structures [2], loaded transmission lines as slow wave structures [3], Micro-Electro-Mechanical Systems (MEMS) [4] and others. Suitable technologies not only must consider practical issues during the fabrication but also improve the functional performance. The devices which can be fabricated by the advanced fabrication technology is known as deep X-ray lithography (XRL), available at the Synchrotron Laboratory for Micro and Nano Devices (SyLMAND) at the Canadian Light Source at the University of Saskatchewan, show outstanding RF performance and compact structure, such as couplers [5], filters [6], MEMS elements [7], antennas [8], cavity resonators [9] and other structures. This advanced technology not only can miniature the target size but also can enhance the performance of the system and the single device as well. The motivation of this research is to apply the advantages of deep XRL technology to the low permittivity DRA ($\varepsilon_r \leq 10$) feeding design to enhance the antenna performance and apply the proposed novel feeding structure into low permittivity DRA array design.

1.2 Deep X-Ray Lithography

The term LIGA comes from German acronym with English translation of lithography, electroforming, and molding. This method is one of the micro-techniques to fabricate miniature 3-D structures and was invented at IBM combined with X-ray lithography and electroplating to produce gold structures with high aspect ratios (ratio of the maximum height to the minimum horizontal dimension of a structure) [19]. However, due to cost issues, this method is sometimes less ideal for large scale structure production. In order to confront this issue, in the 1980's the modern LIGA process was developed at Nuclear Research Center Karlsruhe (presently, Karlsruhe Institute of Technology, KIT) in Germany by introducing a third procedure known as plastic molding that allows, in principle, large-scale production [20], [21]. This LIGA micro-fabrication method includes three procedures, where LI stands for "Roentgen-Lithographie" which means X-ray lithography, G represents "Galvanoformung" that is electro-deposition, A means "Abformung" which is molding.

Recently, application of this technique to RF components which are widely used in a variety of wireless communication areas has drawn much attention. It is especially suitable for fabricating tall (hundreds of microns) structures with micron scale lateral features and vertical structures (typically 89.9^{o}) with smooth side walls (optical quality roughness). These special properties make LIGA a potential powerful tool in the development of high performance microwave devices. Fig. 1.1(a)~(d) show some samples which were made by University of Saskatchewan research group using deep X-ray lithography with electroplating (part of the LIGA process) .

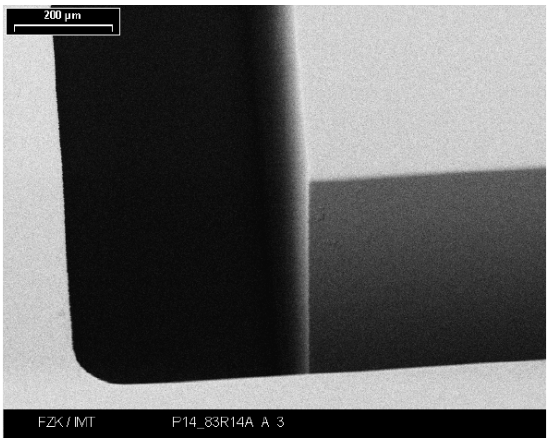

(a) Vertical cavity structure [9]

(b) SU8/Alumina composite DRA sample [12]

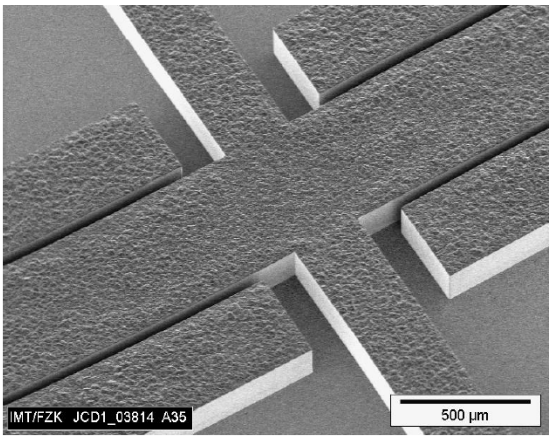

(c) LIGA CPW bandpass filter [26]

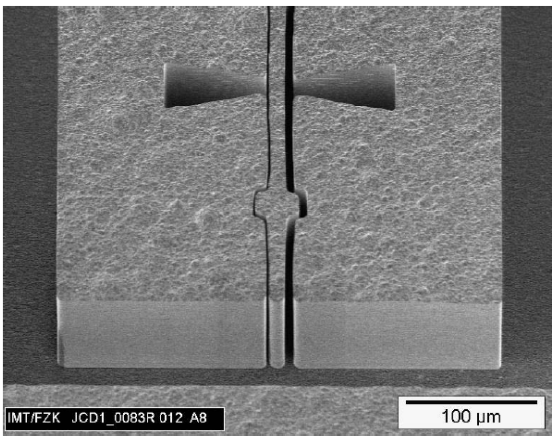

(d) Tunable MEMS capacitor [7]

Fig. 1.1 Various RF components made by deep XRL

The initial steps in the deep XRL process include coating the substrate with photoresist material, synchrotron radiation, and developing. If metal structures are required, electroplating of metals follows, plus possible further development to remove the photoresist if required. Since the materials or the structures of devices vary, the basis process steps also vary. In this research, deep XRL would be used to fabricate both the polymer composite DRA elements and also the metal feeding network. The detailed fabrication process steps for both types of structures used to fabricate microwave devices are well explained (Illustrated in appendix) and other works in

university of saskatchewan research group, for instance, the metal structures of the 3dB CPW coupled line coupler [5], bandpass filter [6], cavity resonator [13], and poly DRA structures [12].

1.3 Literature Review

There are limited research works on the application of deep XRL for microwave and RF devices. One such application to metal microwave devices is in [25], introducing the stepped-impedance low-pass filter which operates at X-band (8~12.4 GHz) and a broadband bandpass filter based on LIGA microstrip lines. Both of these two filters are realized with 200μm thick nickel conductors on 420μm thick fused quartz (relative permittivity 3.81 at 30 GHz) substrate. Following, more applications to metal device have been made, such as the 3-dB LIGA coupled-line coupler in [5], the CPW band-pass filter with compact unit cells in [26], MEMS variable capacitors in [7] and use of MEMS lumped elements to made complex circuit [74]. All of these microwave and RF devices show excellent performance.

Recently, deep XRL has been extended to fabricate dielectric structures and most of these devices have been used for DRA applications [12], [14]. These DRAs are made by using composite materials to achieve different low permittivity values than obtainable with pure resists. Good performance can be obtained; however, traditional planar feeding schemes have been problematic due to difficulties, such as low coupling energy on exciting low permittivity materials [15] ~ [18].

Various traditional methods of exciting the dielectric resonator (DR) as a radiating element and using these to build arrays are summarized in [27]. Recently, there is considerable research on

how to excite DRAs to improve the performance for a wide range of commercial wireless applications, for instance combining two DRAs together to make a multi-mode antenna covering different frequency bands [28], or using a hybrid structure to enhance the impedance bandwidth [29]. Using the notched DRA to produce the multimode in [30] and [31] also can improve the impedance bandwidth and produce outstanding performance. However, most of these methods result in complicated feeding structures, making them difficult to apply to DRA array design. On the other hand, for the traditional feeding schemes, it is difficult to achieve critical coupling for excitation due to the DRA with low permittivity value. These limitations are obstructions on the current research of feeding schemes for DRAs with very low permittivity value ($\varepsilon_r \leq 10$).

1.4 Research Objective

The main target of this research focuses on applying the advantages of tall transmission line fabricated by deep XRL technology to develop the novel feeding scheme on exciting the DRA with low permittivity value ($\varepsilon_r \leq 10$). The characteristics of tall transmission lines are investigated. The rectangular DRA with low permittivity values will be investigated and different feeding schemes and field distributions are shown in this research. After mastering both the properties of tall transmission line and DRA, how to apply the tall transmission lines to excite the rectangular DRA with low permittivity value becomes the primary target of this research. Three novel feeding schemes: side coupling feeding, direct feeding and T shape feeding are proposed and show promising performance in exciting rectangular DRAs with low permittivity ($\varepsilon_r \leq 10$), making these novel feeding schemes not only simple to use but also more effective. Further, the

T shape feeding structure is applied to design a linear rectangular DRA array with low permittivity (ε_r=5). This linear DRA array presents wide band operation and also a good radiation pattern, and the extremely low permittivity makes the direct use of non-ceramics materials such as pure polymers or polymer-composites feasible. During this process, the advantages of T shape feeding structure are shown, making the simulation more effective than the traditional way.

1.5 Thesis Organization

The contents of this thesis discuss the DRA, a new feeding scheme for low permittivity rectangular DRAs and application to linear array design.

Chapter 2 discusses the basic fundamentals and the properties of DRA. It mainly focuses on the rectangular DRA, including a variety of typical feeding schemes, corresponding modes, field distributions, and radiation patterns.

Chapter 3 describes the characteristics of the deep XRL fabricated tall transmission line. The performance of the tall transmission line is presented.

Chapter 4 proposes three novel feeding structures composed by the tall microstrip line for exciting the rectangular DRAs with low permittivity ($\varepsilon_r \leq 10$). Analysis of the simulation and experimental measurement are presented in this chapter.

Chapter 5 presents the T shape feeding scheme to build the very low permittivity linear rectangular DRA array. Dolph-Chebyshev array is designed. A new simulation method by using the advantages of T shape feeding structure is proposed and the simulation results show the

effectiveness and feasibility of tall feeding structure in designing the low permittivity linear DRA arrays.

Finally, Chapter 6 gives the conclusions of this research and description of the future work.

Chapter 2
Dielectric Resonator Antenna (DRA)

2.1 Introduction--Overview of DRA

With the development of modern wireless communication and the ever increasing requirements for modern wireless devices and applications, novel advanced antennas with improved performance are essential. Initially, Dielectric Resonators (DR) were treated primarily as energy storage devices and used in microwave circuits, such as the filters and oscillators. These DRs with the high quality-factor were made by high permittivity (ε_r) material with ε_r higher than 20, such as crystal TiO_2 or ceramics. Many DRs are placed into a closed metallic cavity to maintain the high Q-factor and avoid the radiation [32]. At that time, the concept that the DR could be used as the radiation element was not appreciated by most researchers.

Since the DR resonates at different modes and different frequencies, with the proper feeding mechanism the DR can act as a radiation element. In 1983, the cylindrical dielectric resonator was proposed as a dielectric resonator antenna by Long et al. [33]. Subsequently, other papers on the investigation of different shapes of DRA, such as rectangular DRA [34] and hemispherical DRA [35] were published. These contributions laid the foundation for future investigations of DRA performance, including novel shapes, new feeding schemes, and different modes, which created many new and attractive features for novel antenna design.

In this Chapter, the various geometries of DRA will be shown and its outstanding advantages

will be discussed firstly. These features can explain why the DRA has become so popular in advanced antenna design. The Rectangular DRA will be the focused analysis target, for example, describing its properties based on the classic wave equations, and computing the resonant frequency based on a fixed dimension, various mode distributions, and so on. The 3D finite element software Ansoft HFSS will be applied to practical design and for comparing with the theoretical calculations. Finally, different feeding schemes and their characteristics will be discussed.

2.2 Geometries and Advantages

One of the attractive features of the DRA is that it can be made in various shapes and in a variety of different materials. Correspondingly, different geometries provide different modes and performance, and various geometries have been tried experimentally to get the best radiation performance. The systematic, theoretical, and experimental investigations on cylindrical disk DRA shapes are illustrated in [33]. Other geometries such as split cylinder, sectored cylinder, metalized DRAs, cylindrical rings, conical, elliptical, spherical, hemispherical, triangular, rectangular, notched rectangular, chamfered, spherical cap, tetrahedral, perforated, stepped, and hybrid DRAs, have been reported. Fig. 2.1 illustrates various shapes possible as examples.

Although many different shapes of DRA have been made, the radiation pattern for the most of the DRAs performs like an electric or magnetic dipole. In addition, this radiation pattern is affected by some critical factors, such as feeding schemes, mode distribution, and dielectric material. Most research focuses on the cylindrical and rectangular DRAs due to their simplicity

Fig. 2.1 Various shapes of DRA (Picture comes from NTK Technologies Incorporated [76])

in design, fabrication, and analysis. DRAs with different shapes also offer many advantages to allow the designers to fulfill many requirements easily.

- ✓ *Design Flexibility*. For a rectangular DRA as an example, for given resonant frequency, two aspect ratios (height/length and width/length) can be chosen independently in terms of bandwidth control [36]. This offers high degree of flexibility in designing work.
- ✓ *Ease of Fabrication*. The simple shapes of DRAs such as circular cylinder, rectangular, and hemisphere not only offer the outstanding performance, but also can be easily fabricated. Additionally, most of the circular cylinder or rectangular DRAs are applied for commercial purposes.
- ✓ *Size and Bandwidth Control.* The DRA dimension is related to the wavelength λ_0 of the free space resonant frequency and the dielectric constant ε_r as:

$$D \propto \lambda_0 \varepsilon_r^{-0.5} \tag{2.1}$$

In addition, the bandwidth of the DRA is inversely related to the dielectric constant ε_r. So the size of DRA made of high permittivity material is smaller than the DRA made of low permittivity material under the same resonant frequency; moreover, the bandwidth of DRA bandwidth made of high permittivity material is narrower as well. Thus, for the same resonant frequency there is natural reduction in size comparing with the traditional antenna like the microstrip antenna.

- ✓ *Various Feeding Schemes.* There are many feeding schemes that can be used to excite the DRA basing on different requirements, such as probes, slots, microstrip line, dielectric image guide, and so on. These different feeding mechanisms make DRAs easy to integrate with existing technologies.
- ✓ *Various Resonance Modes.* There are various resonance modes excited by using different DR shapes that can produce different radiation patterns. Further, Q-factor for some special modes is also determined by the aspect ratio of the DRA, providing an additional degree of flexibility to the design work.
- ✓ *High Efficiency.* High radiation efficiency can be achieved because there is no inherent metallic conductor loss. This attractive characteristic is very useful for millimeter wave antenna applications, where the loss from metallic antennas can be high.
- ✓ *Wide Impedance Bandwidth.* Since the DRA radiates the energy through the whole surface comparing with the traditional microstrip antenna, it has the wider impedance bandwidth. Moreover, the impedance bandwidth also can be varied by changing the dielectric constant of the material and the aspect ratio, making the DRA a good

- ✓ *High Power Handling and Temperature Stable.* DRAs have high power handling ability due to the high dielectric strength. Since ceramics are typically excellent materials for temperature stability, DRAs can operate over a wide temperature range.

In this thesis, the main research and application will focus on the rectangular DRA (RDRA), including the different radiation modes, various feeding schemes, and theoretical calculations on the geometry.

2.3 Analysis and Simulation of Rectangular DRA

2.3.1 Analysis for the Rectangular DRA

The RDRA is the most common DRA for practical applications, because it offers some attractive features. It is easy to fabricate and more flexible for design than the other geometries, and it avoids mode degeneracy and offers bandwidth control. In order to model the dielectric resonator antenna, the approximate dielectric waveguide model (DWM) [37] is employed into this analysis. After truncating along the *z*-direction at $\pm d/2$ along the DWM and applying the boundary condition of magnetic walls on the surfaces, the isolated DRA model in free space can be obtained. Fig. 2.2 shows both the truncated waveguide model and isolated rectangular DRA model.

This RDRA can support two different modes, *TM* mode and *TE* mode; however, it is suggested that lowest order *TM* modes have not been observed experimentally [38]. Since the RDRA has

three independent dimensions, the resonant *TE* modes can be designed as TE^x, TE^y, TE^z.

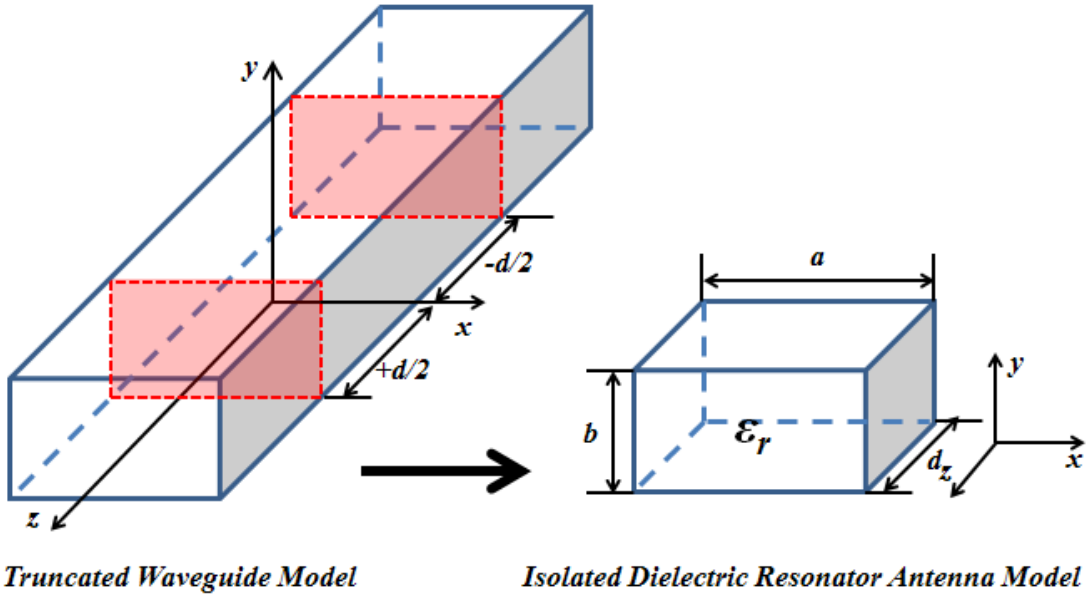

Fig. 2.2 Truncated waveguide model & isolated RDRA model

In Fig. 2.2, under these coordinates, the RDRA with the dimension *a*, *b*, *d*, where *a* and *b*> *d,* the lowest order mode will be $TE^z_{11\delta}$. The following wave equations describe the field distribution [32]:

$$H_x = \frac{k_x k_z}{j\omega\mu_0}\sin(k_x x)\cos(k_y y)\sin(k_z z) \tag{2.2}$$

$$H_y = \frac{k_y k_z}{j\omega\mu_0}\cos(k_x x)\sin(k_y y)\sin(k_z z) \tag{2.3}$$

$$H_z = \frac{k_x^2 + k_y^2}{j\omega\mu_0}\cos(k_x x)\cos(k_y y)\cos(k_z z) \tag{2.4}$$

$$E_x = k_y \cos(k_x x)\sin(k_y y)\cos(k_z z) \tag{2.5}$$

$$E_y = -k_x \sin(k_x x)\cos(k_y y)\cos(k_z z) \tag{2.6}$$

$$E_z = 0 \tag{2.7}$$

Where E_x, E_y, E_z, are the electrical field along *x*, *y*, and *z* directions respectively inside the DR

and the H_x, H_y, H_z are magnetic field along *x*, *y*, and *z* direction respectively inside the DR. The k_x, k_y, and k_z denote the wave numbers along the *x, y* and *z* directions respectively inside the DR and they can be obtained from these corresponding formulas by enforcing the magnetic wall boundary condition $E \cdot n = 0$ at the resonator surface, i.e., at $x=\pm a/2$ and $y=\pm b/2$ [36]:

$$k_x = \frac{\pi}{a} \quad k_y = \frac{\pi}{b} \quad k_0 = \frac{2\pi f_0}{c} \tag{2.8}$$

Where $c=3\times10^8$ *m/s*. These wave-numbers also satisfy the conditions that [36]:

$$k_x^2 + k_y^2 + k_z^2 = \varepsilon_r k_0^2 \tag{2.9}$$

$$k_z \tan\left(\frac{k_z d}{2}\right) = \sqrt{(\varepsilon_r - 1)k_0^2 - k_z^2} \tag{2.10}$$

k_z can be obtained by solving the transcendental equation (2.10) through the simple numerical method; then the expression which only includes k_0 can be obtained by substituting the equation (2.8) into (2.9). The resonant frequency can be achieved by solving k_0 expression using the result of k_z in the first step.

2.3.2 Fields within the Rectangular DRA

Ideally the DRA element is mounted on an infinite conducting ground plane (see Fig. 2.3). Based on the image theory [39], the height of the DRA can be modeled as half that in the DWM, which is: $H=b/2$. If the DRA dimension in Fig. 2.3 fulfills the condition that $a > b/2 > d$, the dominant mode will be $TE^z_{11\delta}$ [27] with $m=n=1$, where the Greek letter δ can be defined as the fraction of a half-cycle of the field variation in the *z*-direction and is given by [27]:

$$\delta = \frac{k_z}{\pi / d} \tag{2.11}$$

Fig. 2.4 shows the fields distribution of the dominant mode of $TE^{z}_{11\delta}$.

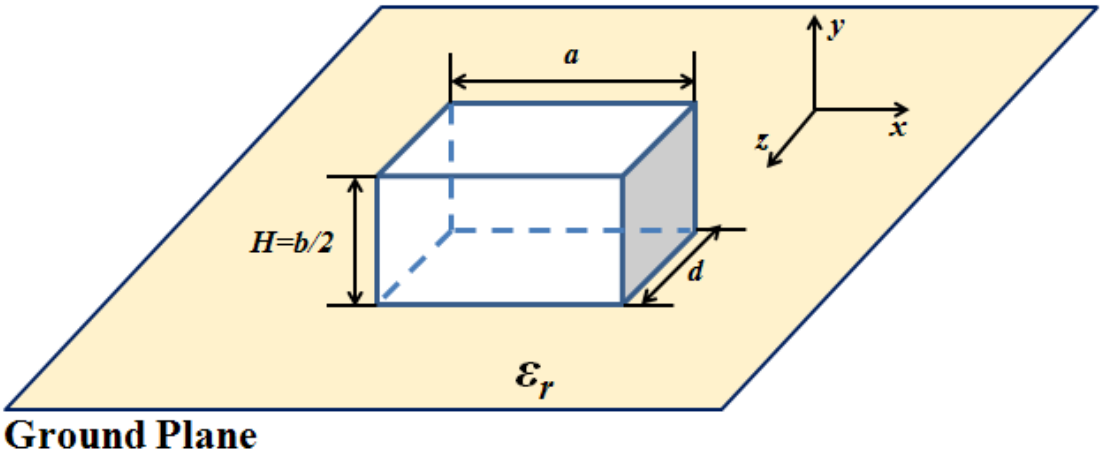

Fig. 2.3 DRA mounted on the infinite ground plane

The components of the magnetic field will dominate along the center inside the DRA, while the electric fields in other directions such as *y* and x components will circulate around the magnetic fields. This distribution is similar to that of a short magnetic dipole, which results a radiation pattern like in Fig. 2.5. This ideal radiation pattern assumes the condition that DRA is placed on the infinite ground plane; while in practical application, the finite ground plane will have the effects on the radiation pattern, introducing the ripples in the radiation pattern and the back-lobe radiation due to the diffraction from the finite ground plane [32].

Through modifying the aspect ratio of DRA dimension, some higher order modes can be excited. Recently many researchers in [28-31] use this property to enhance the impedance bandwidth, producing the advanced multimode antenna to meet with the requirements of the modern wireless communication. Fig. 2.6 shows different higher-order modes. As described in [27], for both higher order mode $TE^{z}_{31\delta}$ and $TE^{z}_{13\delta}$, their radiation patterns which have the peak in the broadside direction (along the *z*-axis) is similar as the $TE^{z}_{11\delta}$ mode. While the mode $TE^{z}_{21\delta}$ will have a null at the broadside direction; peak will appear at the end-fire direction (along the *x*-axis).

Since the tangential of the E-field at the y=0 is zero, so the mode $TE^{z}_{12\delta}$ does not exist in this case, because it requires the maximum E-field at the location where y=0.

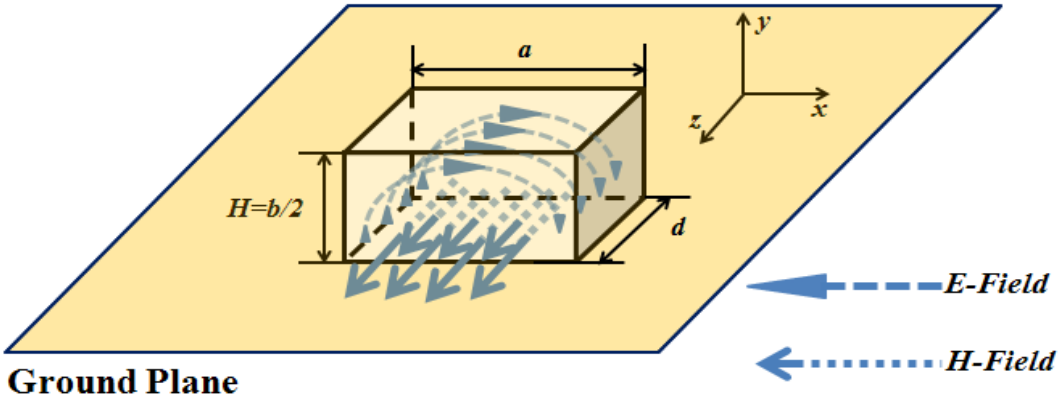

(a) 3D fields distribution

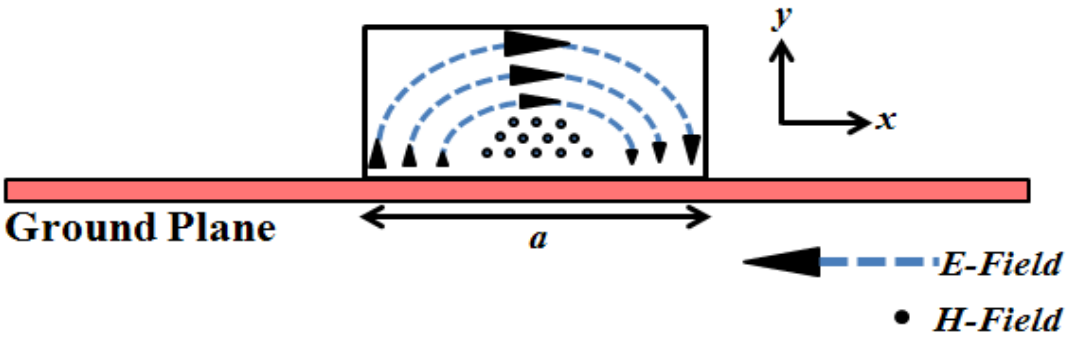

(b) Fields distribution in x-y plane

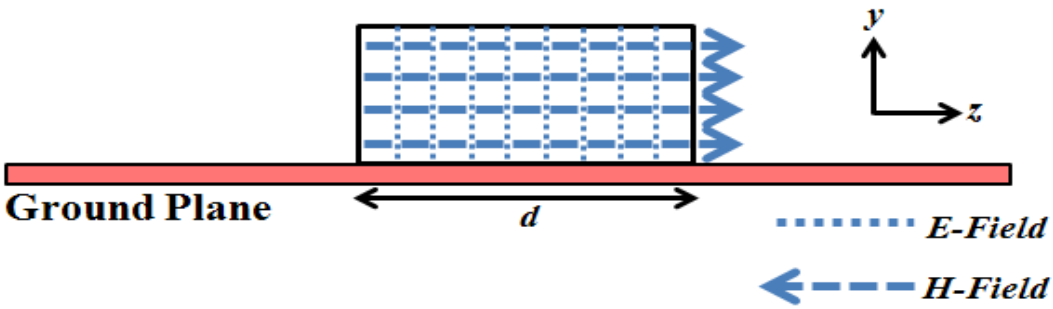

(c) Fields distribution in y-z *plane*

Fig. 2.4 Fields distribution of the dominant mode $TE^{z}_{11\delta}$

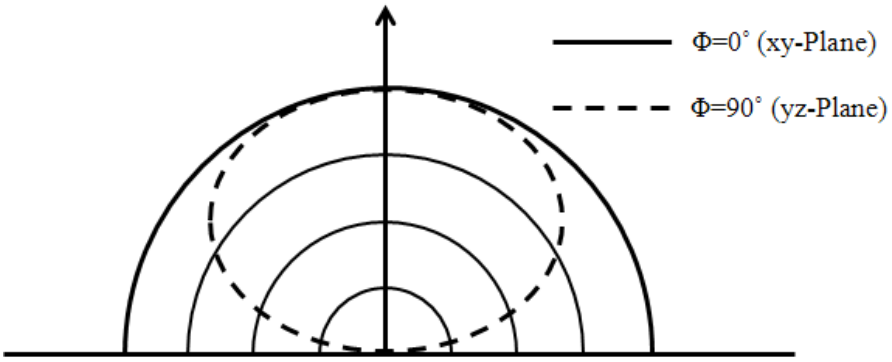

Fig. 2.5 Dipole like radiation pattern for RDRA on the infinite ground plane

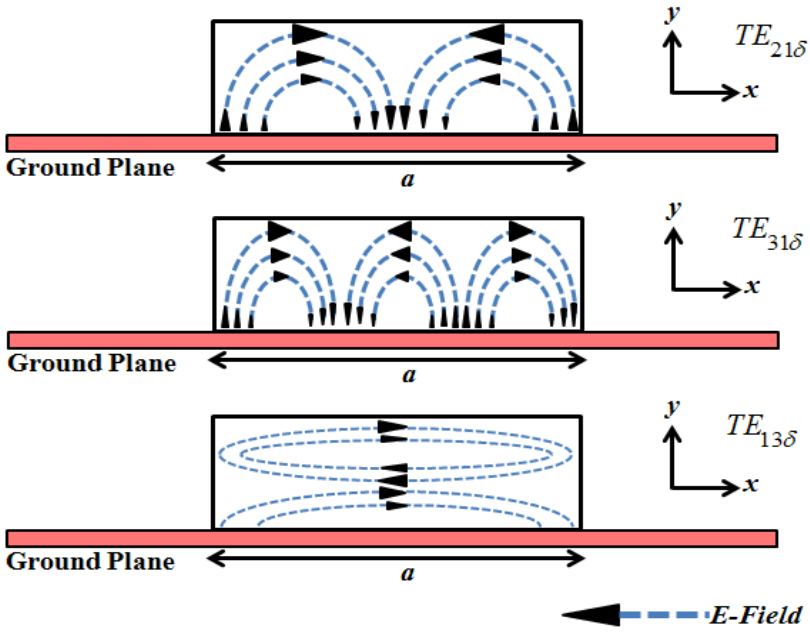

Fig. 2.6 E-fields distribution for different higher-order modes inside the RDRA

2.3.3 Simulation and Verification

a. Introduction of the Simulation Tools

In this section, commercial finite element method (FEM) based Ansoft High Frequency Structure Simulator (Ansoft HFSS) 3D electromagnetic simulation software is applied to design and analyze the properties of RDRA.

The simulator of the HFSS which is used to calculate the full 3D electromagnetic field inside the

object is based on the FEM. Theoretically, the FEM method divides the object into thousands of smaller regions represented using a local function in each sub-region. During the process of calculation, the model will be separated into a large number of tetrahedrons which are four-sided pyramids. These small tetrahedral units form finite element meshes. HFSS represents the field quantities and analyzes it in three areas. Inside of the mesh element, the values of vector field quantity, such as the E-fields or H-fields are interpolated from the vertices of the tetrahedron. At each vertex point, the field components are tangential to the three edges of the tetrahedron. Further, the components of field vectors at the middle point of the each edge are tangential to the face and normal to each edge [60]. Fig. 2.7 presents these three areas. More reference on applications to electromagnetic problems for FEM can be found in [40], [41].

By representing field quantities in these three areas, HFSS can transform Maxwell's equations into matrix equations and solve them by using traditional numerical methods. In order to get the accurate results, large numbers of small mesh elements must be used in the calculation; however, the amounts of available computer resources limit this requirement. Hence, a trade-off between the object size and the mesh complexity is necessary. Additionally, in order to get the more precise field quantity results, HFSS uses an iterative process in which the mesh is automatically refined in critical regions, making sure each element is small enough for the field to be adequately interpolated from the nodal values.

b. Simulation by Ansoft HFSS and Verification

In this section, the Eigenmodes solver in Ansoft HFSS is applied to analyze the resonant

frequency by fixing the RDRA dimension. Ansoft HFSS eigenmode solver can obtain the different resonant frequencies as well as the corresponding field distribution under the different modes.

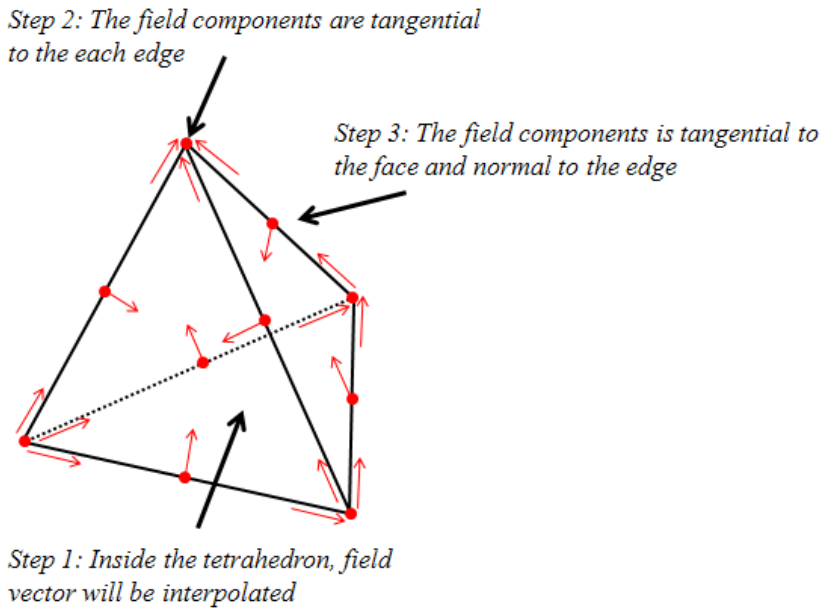

Fig. 2.7 Graphic of the calculation processes in HFSS

In this case, an RDRA with the dimension L=5mm, H=2mm, W=3mm and permittivity of 10 is investigated as an example. Since the coordinate axis in the HFSS simulation is different from the previous definitions in theory, the propagation direction of the magnetic field changes to Y axis, so the dominant mode should be $TE^{y}_{1\delta l}$ as shown in Fig. 2.8 and calculation of the resonance frequency for the dominant mode is predicted to be 18.033GHz based on the DWM model using equations (2.8), (2.9), (2.10). Then the HFSS Eigenmode solver is employed in the verification work as described in the following steps.

- *Step 1. Building the model and setup the simulation*. Fig. 2.8 is the RDRA model with permittivity of 10 in HFSS. The RDRA is placed inside the ideal perfect conducting cavity

(not shown in Fig. 2.8), which can be set by selecting a prefect E boundary on each surface of the cavity. The *Maximum Delta Frequency Per Pass* which is the percentage difference between calculated eigenmode frequencies from one adaptive pass to the next is set to 0.01. This value can control the mesh elements adaptively to increase the accuracy until the maximum number of the passes is completed [60].

- *Step 2. Results and Analysis.* During the simulation, there are approximate 10300 tetrahedral elements created which are applied to analyze the RDRA structure in HFSS. Fig. 2.9(a) shows the mesh distribution over the RDRA surface. The results are shown in Fig. 2.9(b). From the modes table, it can be seen that mode 1, 2 and mode 5, 6 are degenerate modes resulting by the conducting cavity boundary, which means they have the same resonance frequency but different modes; additionally, mode 7, 8 and 10 are also introduced by the conducting cavity boundary. Since the DRA changes the environment inside of the cavity, the resonance frequency and the field distribution of the conducting cavity box under the different modes are close to the characteristics of the standard empty conducting cavity, but not fulfill the characteristics strictly especially when the DRA operates at its own mode.

  The resonant frequency of dominant mode $TE^{y}_{1\delta l}$ is 18.1055GHz which is mode 3 as shown in Fig. 2.9(b) comparing to the 18.033GHz in theory, offsetting about 0.38%. The second order mode for RDRA is $TE^{x}_{\delta 11}$ whose resonant frequency is 18.8885GHz (the propagation direction of the magnetic field changes to X axis direction) which is mode 4 in Fig. 2.9(b). Since the resonator edge changes from *a* to *d* which is smaller than before, the resonant frequency for $TE^{x}_{\delta 11}$ is higher than $TE^{y}_{1\delta l}$. Mode 9 is $TE^{y}_{2\delta l}$ and the resonant frequency is

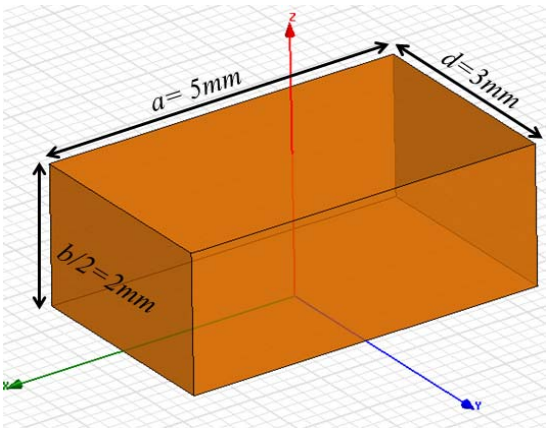

Fig. 2.8 Geometry of the RDRA analyzed in HFSS

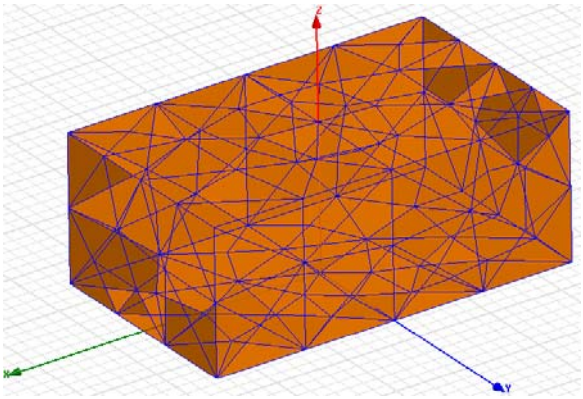

(a) Meshing on the surface of the RDRA

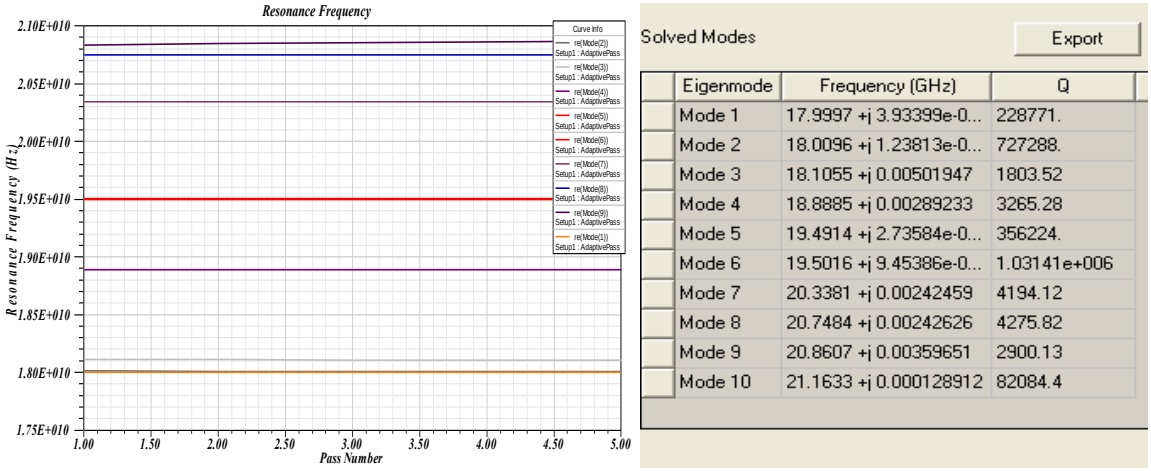

(b) Resonance Frequencies under the Different Modes

Fig. 2.9 Simulation results in HFSS

about 20.8607GHz. Mode $TE^{y}_{1\delta 2}$ does not exist since the tangential components of the

E-field at z=0 is zero. Fig. 2.10 illustrates the simulated field distribution of RDRA for different modes.

2.4 Excitation Techniques of the RDRA

In practical applications, signal power must be coupled in or out of the DRA through suitable methods, which are so-called excitation techniques. It is one of the critical parts in DRA design work. For different types of feeding schemes, such as the location of the port with respect to the DRA, the types of port and its dimension will decide how much power can be coupled to DRA and which modes can be excited. In addition, these feeding schemes have considerable impacts on the resonant frequency and Q-factor. Hence, it is necessary to analyze the characteristics of the different feeding mechanisms prior to coming up with the novel feeding scheme using the tall transmission line.

According to the Lorentz Reciprocity Theorem and the foundation of coupling theory for the resonator circuit in [42], the coupling factor k between the source and the field inside DRA can be described as an electric source and a magnetic source respectively as below:

$$K_E \propto \int (\vec{E}_{DRA} \cdot \vec{J}_S) dV \tag{2.12}$$

$$K_M \propto \int (\vec{H}_{DRA} \cdot \vec{M}_s) dV \tag{2.13}$$

where V is the whole volume of the DRA, vector $\vec{E}_{DRA}$ and $\vec{H}_{DRA}$ are the electric and magnetic field intensity respectively inside the DRA, while the vector $\vec{J}_s$ and $\vec{M}_s$ are the electric and magnetic sources respectively. Equation (2.12) represents the electrical current source is located at the maximum electric field within the DRA in order to achieve strong coupling. While

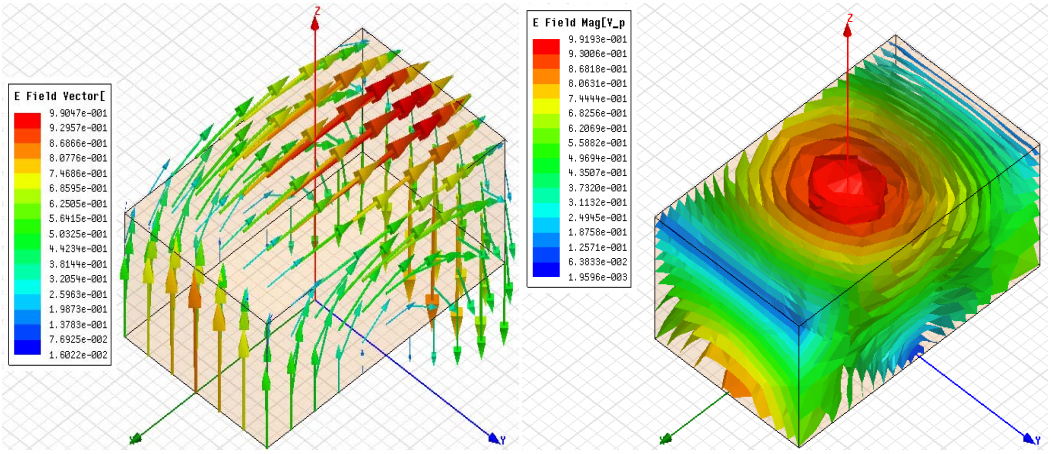

(a) E field vector for TE^{y}_{111} (b) E field magnitude for TE^{y}_{111}

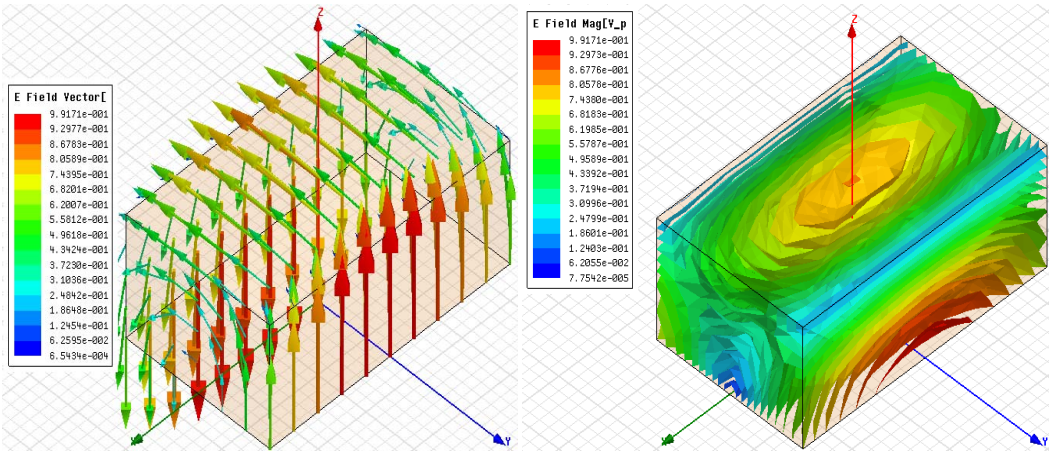

(c) E field vector for TE^{x}_{111} (d) E field magnitude for TE^{x}_{111}

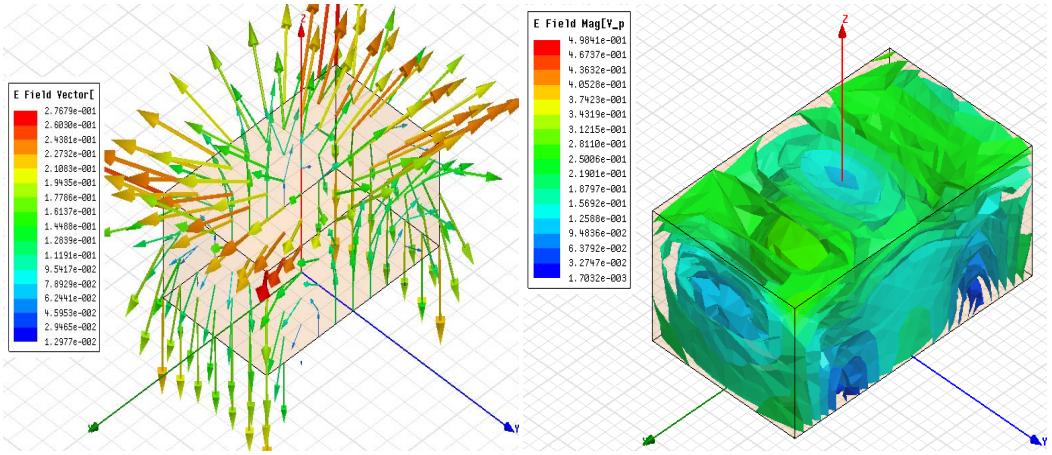

(e) E field vector for TE^{y}_{211} (f) E field magnitude for TE^{y}_{211}

Fig. 2.10 Simulated field distribution of different modes in HFSS; assuming δ=1, field intensity(V/m) represented by color bars

equation (2.13) illustrates the magnetic current source is placed at the maximum magnetic field within the DRA to obtain strong coupling. The following sections will illustrate the various feeding mechanisms.

2.4.1 The Coaxial Probe Feed

Coaxial probe feed is a very common method to excite the DRA and is widely used in practical applications. The probe consists of the transmission line (coaxial cable) with a short length of exposed inner pin. This pin can be seen as an open circuit vertical electrical source extending above the ground [27]. In order to achieve the desired coupling to excite the DRA, the probe can be considered as the vertical electrical current and is placed in the region where the DRA has high electric field as described in equation (2.12) and the dominant mode $TE^{z}_{11\delta}$ will be excited [33]. Fig. 2.11 shows this feeding structure and Fig. 2.12 presents the fields distribution of the dominant mode.

The advantage of this structure is the ease to match to 50Ω system. Since the transmission line can connect with the 50Ω system directly, the matching network becomes simple. In addition, the location of the probe can be placed adjacent to the DRA to control the amount of coupling, optimizing the matching condition. In order to obtain the good radiation pattern, the height of

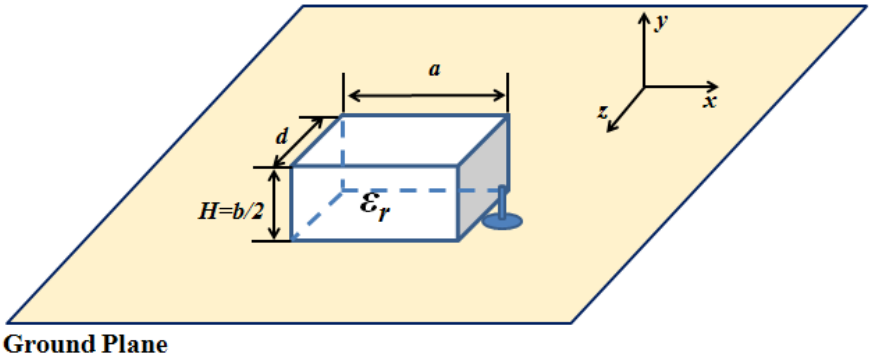

Fig. 2.11 Coaxial probe feeding structure

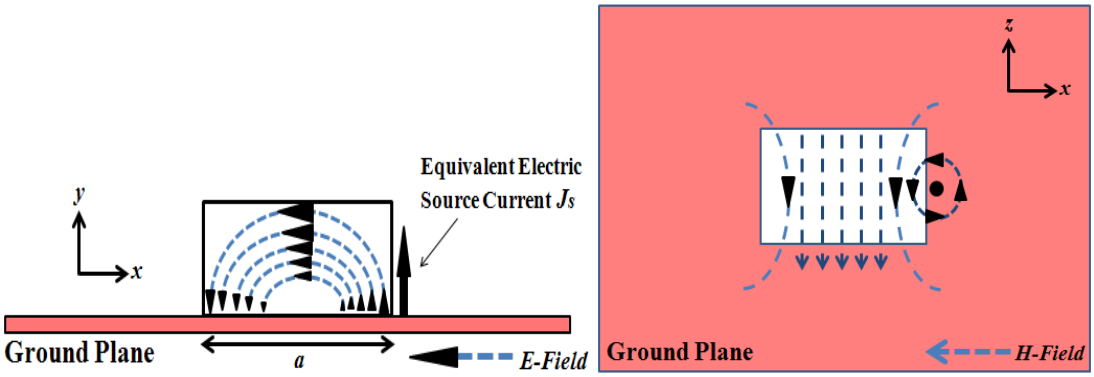

(a) E field distribution (b) H field distribution

Fig. 2.12 Field distribution of the coaxial probe feeding structure

the probe is usually lower than the height of the DRA to avoid probe radiation. However, some investigation focus on the effects of the feeding probe length, when its height is around a quarter guided wavelength, this probe can be seen as both the feeding source and the monopole radiator, which is a so-called hybrid mode DRA [43]. [33] claims that there are not suitable equations to design the required probe height for a given set of DRA dimensions and permittivity. In practice, the probe height can be obtained by using the experimental way to try the probes with different height until the desired match is achieved. Moreover, since the probe can be seen as the vertical electrical source, especially when it is substituted by a flat metal strip attached to the DRA, strong coupling can be obtained by placing the strip at the region where the DRA has high

electric field [44]. When the DRA operates at millimeter-wave, both of the resonant frequencies of DRA and the probe (or the strip) can be combined together to increase the bandwidth, creating the wide band antenna [45].

2.4.2 The Co-planar Slot Loop Feeding

Compared to the probe feeding structure, planar feeding does not need the obtrusive structure, easing the fabrication. By moving the co-planar loop from the edge to the center of the DRA or by changing shape of the loop, the amount of the coupling can be varied; furthermore, this feeding scheme can provide addition control for impedance matching by adding stubs or loops at the end of the line [46]. Fig. 2.13 gives the structure of this feeding mechanism and the field distribution. In this case, in order to obtain the desired coupling, the slot loop can be moved from the edge of the DRA to the center and the dominant mode TE^{z}_{111} can be excited [75].

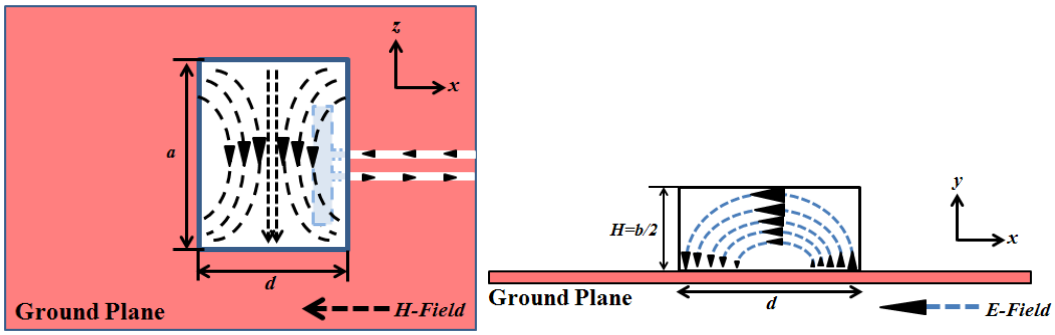

(a) E field distribution (b) H field distribution

Fig. 2.13 Geometry of the co-planar feeding scheme and $TE^{z}_{11\delta}$ fields distribution

In the case of the slot loop structure, there are many different shapes of co-planar structures possible as shown in Fig. 2.14, such as open-circuit co-planar waveguide [47], stub-loaded waveguide-fed [48], and co-planar rectangular loops feed [46].

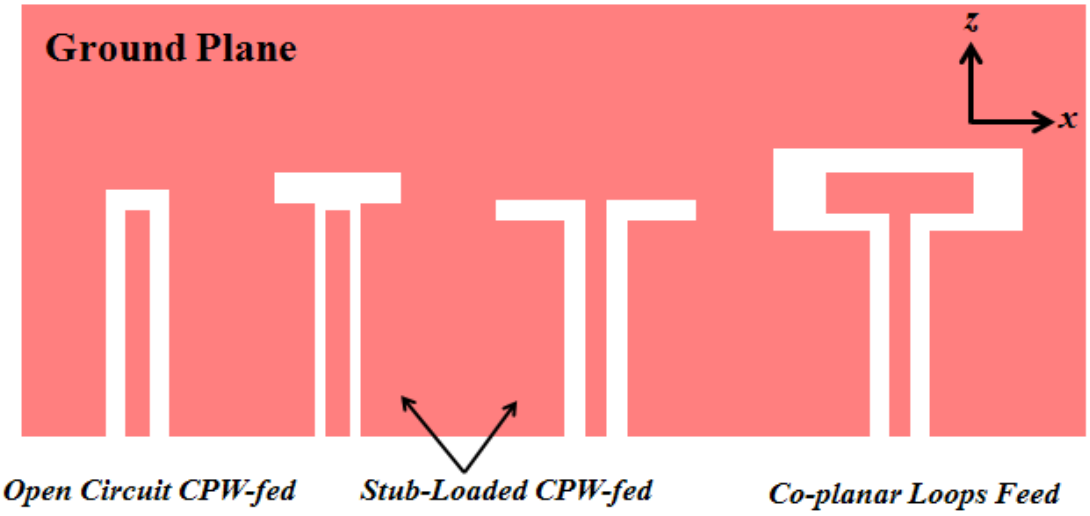

Fig. 2.14 Various co-planar feeding mechanisms

2.4.3 The Slot-Aperture Feeding

The slot-aperture feeding structure is similar to the co-planar feeding. The energy is coupled from the microstrip line to the DRA through fields in the slot aperture. The slot aperture is etched on the ground plane and coupled to either the open-end microstrip line or coaxial cable, or even a waveguide which can be used as one part of the feeding mechanism [49],[50]. When the energy is coupled to the DRA, the slot can be considered like an equivalent magnetic current and its direction is parallel to the slot length (See Fig. 2.15).

In order to achieve maximum coupling, the aperture slot should be placed in the region of maximum magnetic fields. Since the feeding line is underneath the ground plane which is isolated from the DRA, the spurious radiation therefore can be avoided [27]. Fig. 2.16 gives the structure and field distribution of this feeding scheme.

In this case, $TE^{z}_{11\delta}$ as the dominant mode will be excited. Furthermore, by adjusting the position

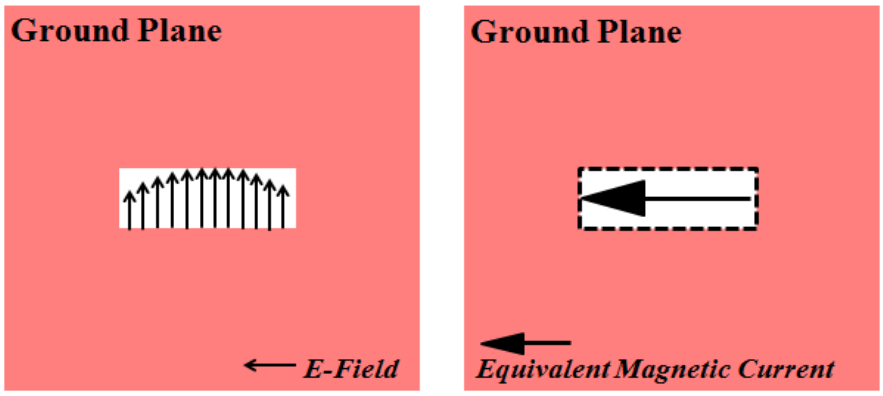

(a) Electric field of the slot aperture (b) Equivalent magnetic source

Fig. 2.15 Slot-aperture coupling illustration

of the DRA with respect to the slot aperture or verifying the dimension of the slot aperture, the coupling amounts can be changed as well as improving the impedance matching condition (the dimension of the microstrip line can be modified to cancel out the reactive components which are brought by the slot aperture) [27]. Furthermore, this feeding structure can be applied to wide band antenna design since the resonant frequency of the slot aperture can be combined with the resonant frequency of the DRA to enlarge the bandwidth [30]. In practical application, the slot size is usually electrically smaller than DRA; this property makes this feeding scheme possible at high frequency (above the L-Bands) [32].

2.4.4 The Microstrip Line Feeding

One of the simplest feeding structures is microstrip line feeding. By using proximity coupling to the DRA from the microstrip line, the magnetic field inside the DRA can be excited, producing

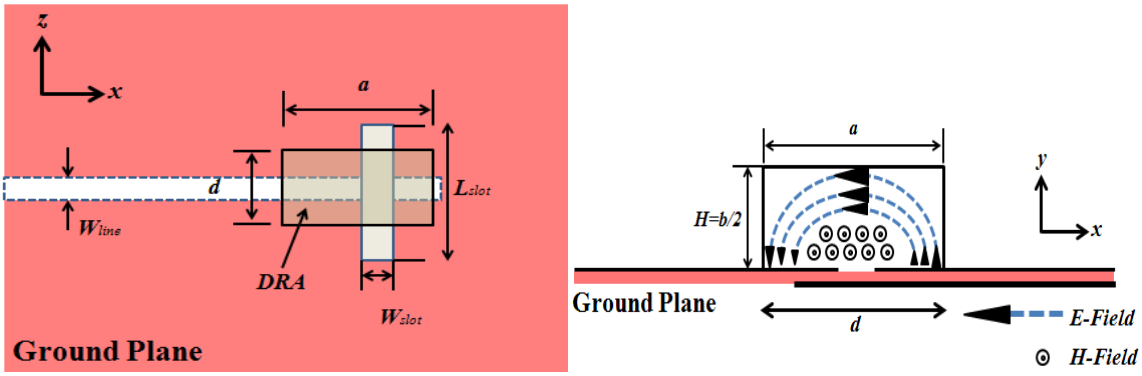

(a) Slot-aperture feeding structure (b) Field distribution of the DRA

Fig. 2.16 Geometry of the slot-aperture feeding scheme and its field distribution

the short horizontal magnetic dipole like $TE^{z}_{11\delta}$ mode as shown in Fig. 2.17. By tuning either the distance between the DRA and microstrip line or the position of the DRA with respect to the lateral microstrip line until obtaining the desired matching condition, the critical coupling between the feeding line and DRA can be achieved. The direction of the magnetic field inside of the DRA is parallel to the microstrip line as shown in Fig. 2.18(a) and the DRA behaves like a short magnetic dipole as shown in Fig. 2.18(b). Additionally, this structure also applies for the other shapes of DRA such as direct feeding on the cylindrical DRA [51].

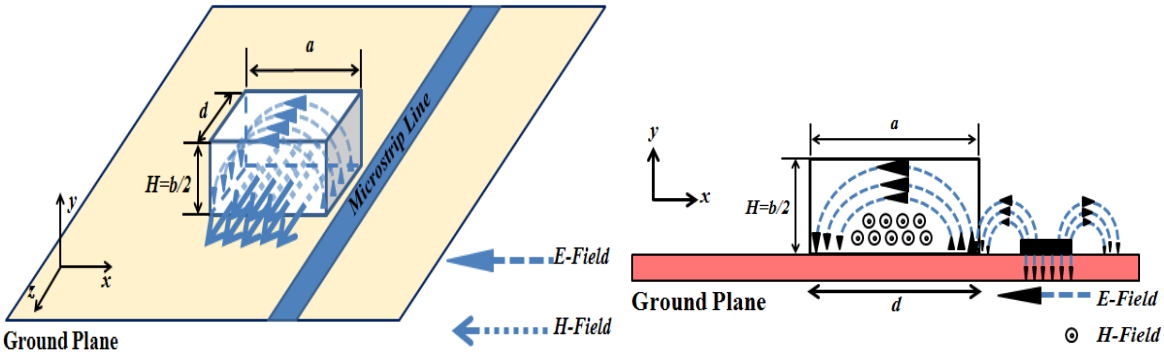

(a) Side coupling feeding structure (b) Fields distribution

Fig. 2.17 Microstrip line feeding structure and the field distribution

The amount of coupling is affected by the permittivity of DRA. When the permittivity value is high (ε_r >20), strong coupling can be obtained, however, the coupling level is significantly

decreased if the DRA has a lower permittivity value (ε_r <10) [27]. In this situation, series feeding for the linear DRA array can be applied to improve the radiation efficiency. The disadvantage of this feeding scheme is the surface wave can be excited at the higher frequency, affecting the radiation pattern and the DRA efficiency [52]; moreover, the matching work becomes problematic especially when the permittivity value of the DRA is very low [36].

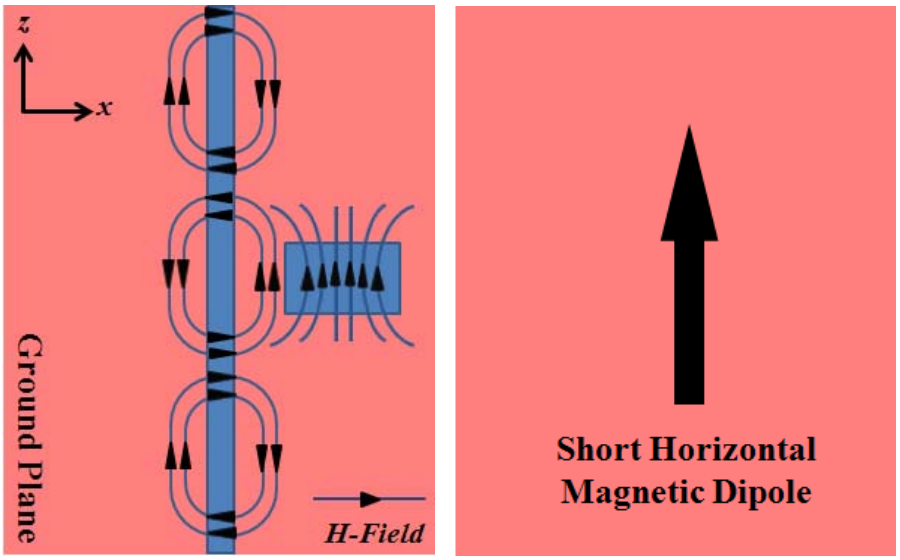

(a) Magnetic field distribution (b) Short magnetic dipole

Fig. 2.18 Magnetic fields distribution of the microstrip line and DRA

Chapter 3
Tall Micromachined Transmission Line

3.1 Introduction of Planar Transmission Line

Microstrip line is a type of planar transmission line which is widely used in practical circuit applications. Since it can be easily fabricated by printed circuit board technology or photolithography methods, its characteristics can be well controlled by modifying the dimension or the material to obtain the desired characteristics. In addition, it can also easily be integrated with circuit elements, so it is one of the most popular types of transmission line applied to microwave circuit design. Fig.3.1 (a)~(d) give different types of planar transmission lines.

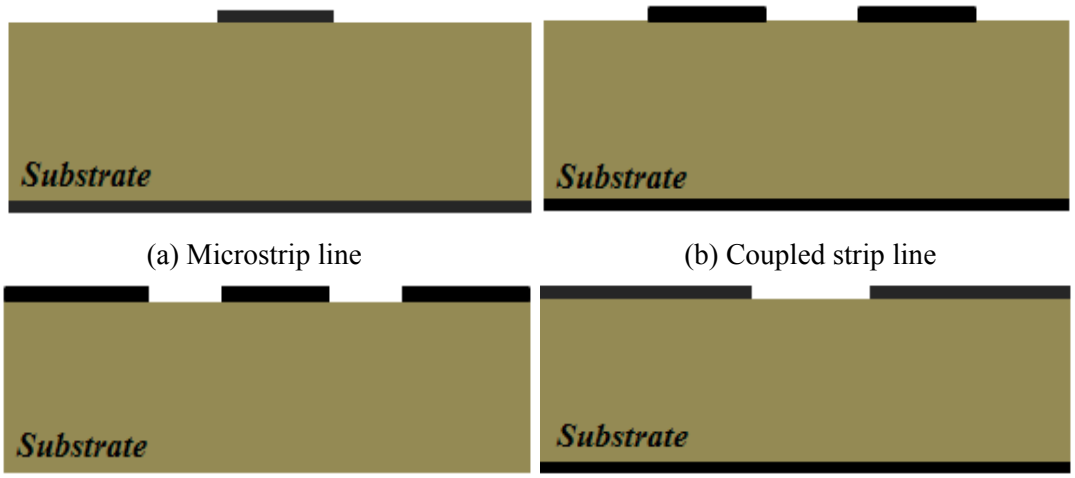

(a) Microstrip line (b) Coupled strip line

(c) Coplanar waveguide (d) Slot line

Fig. 3.1 Planar transmission line.

The microstrip line structure is composed of three parts: metal conductor trace, substrate and metal ground plane. Fig.3.2 (a)~(b) give its configuration.

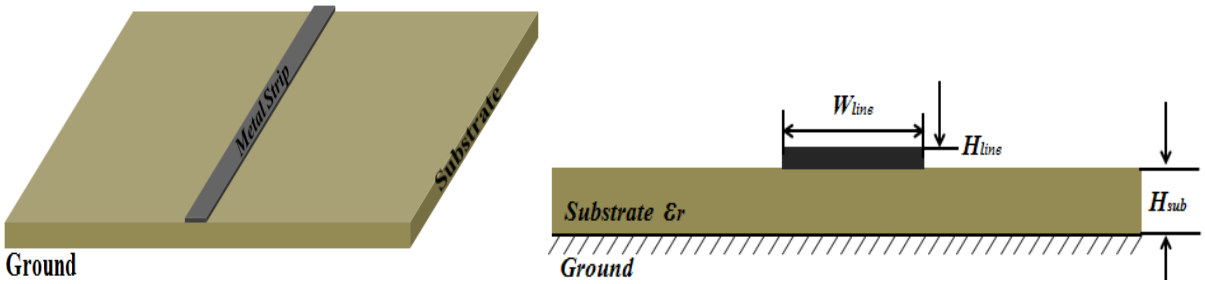

(a) Top view (b) Side view

Fig. 3.2 Geometry of the microstrip line

The metal strip with the proper width and thickness, which can be made by various materials such as copper or gold, is printed on the dielectric substrate with the metal grounded on the other side. The substrate can be of different materials, with relative permittivity values typically in the range of 2 to 20.

Since the conductor strip is placed at the air-substrate interface having different dielectric constants, when the waves propagate through the microstrip line, most of the fields will be confined between the conductor strip and the ground plane inside the substrate area; while a few of fields are present in the air region above the substrate [39]. If the longitudinal components of the E-field or H-Field under the dominant mode of a microstrip line are much smaller than the transverse components, the quasi-TEM approximation can be applied. Fig. 3.3 illustrates the static quasi-TEM field pattern of microstrip line. For this reason, the effective dielectric constant ε_{eff} is introduced and since the inhomogeneous environment is around the metal conductor, the effective dielectric constant is higher than the air permittivity (ε_r=1) but less than the substrate relative dielectric constant as below:

$$1 < \varepsilon_e < \varepsilon_r \tag{3.1}$$

Furthermore, the phase velocity in the dielectric region is $\frac{c}{\sqrt{\varepsilon_r}}$ which is much different than the phase velocity c in the air, so true TEM waves cannot be supported at the dielectric–air interface due to the unmatched phase velocity. The equation for effective phase velocity V_p of the microstrip line can be obtained using the effective dielectric constant as in (3.2)[39].

$$V_p = \frac{c}{\sqrt{\varepsilon_e}} \tag{3.2}$$

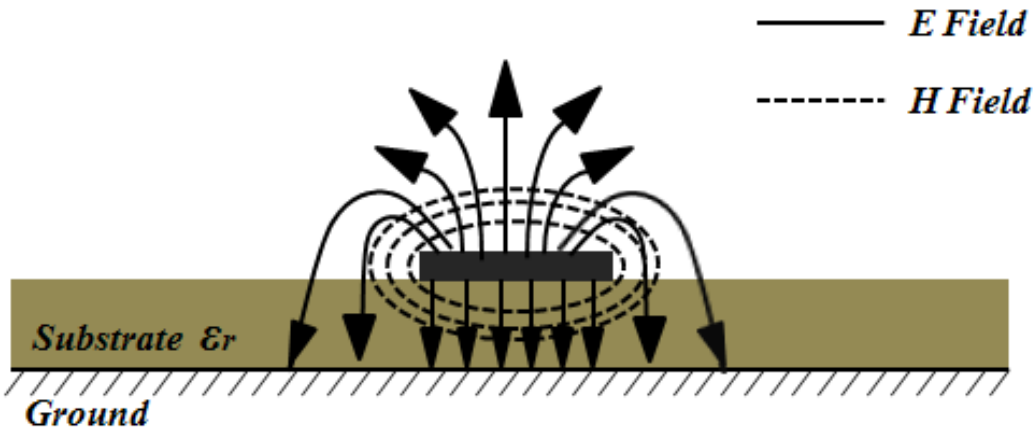

Fig. 3.3 Field distribution for the microstrip line

Presently, there are many papers and commercial tools can provide various approximated models or equations to get the accurate results for parameters such as dimensions, impedance, effective dielectric constant, phase velocity, attenuations and so forth [53]~[57] and these equations are applied to practical design works very well. The details of the theory on planar transmission line as well as the various equations on how to calculate the parameters as discussed will not be included in this thesis. The point will focus on the properties of the tall transmission line and its performance and characteristics are analyzed by using the commercial 3D finite element software Ansoft HFSS in the following sections.

3.2 Deep XRL Fabricated Tall Microstrip Lines

3.2.1 Introduction

Since the deep XRL fabricated tall microstrip line has thicker conductor trace than the conventional microstrip line, it offers many advantages. For conventional microstrip line, its characteristics can be obtained as in [53] using the quasi-static method basing on quasi-TEM model. Good agreement between the experiments and the theory have been shown [55] when the thickness of the conductor with respect to the substrate thickness is smaller than 0.005, while the dielectric constant is in the range of 2 to 10 and the ratio of the strip width to the substrate thickness is in the range of 0.1 to 5.

In addition, these formulae for the characteristic impedance and effective dielectric constant are valid in the case of quasi-TEM model at low frequency [53]. However, as the frequency goes higher and the metal conductor thickness with respect to the substrate thickness increases, the static assumption is not valid or even a poor approximation to describe the properties of this new model. Since the characteristic impedance and the effective dielectric constant change dramatically when the operated frequency is high, the hybrid mode can be excited rather than the quasi-TEM mode, making the transmission line dispersive. So it is necessary to apply the full wave numerical methods to analyze the performance of tall microstrip line.

3.2.2 Analysis and Simulation

The normal microstrip line and deep XRL fabricated tall microstrip line are investigated by using

the 3D finite element software Ansoft HFSS in this section. Fig. 3.4 (a)~(b) give both geometries of conventional microstrip line and deep XRL fabricated tall microstrip line models in Ansoft HFSS software.

The nickel conductor (conductivity=1.47×10^7Siemens/m) is assumed to be plated on a 1mm thick quartz glass substrate (relative permittivity ε_r=3.78 at 10GHz). The different height of the metal conductor h is under the investigation.

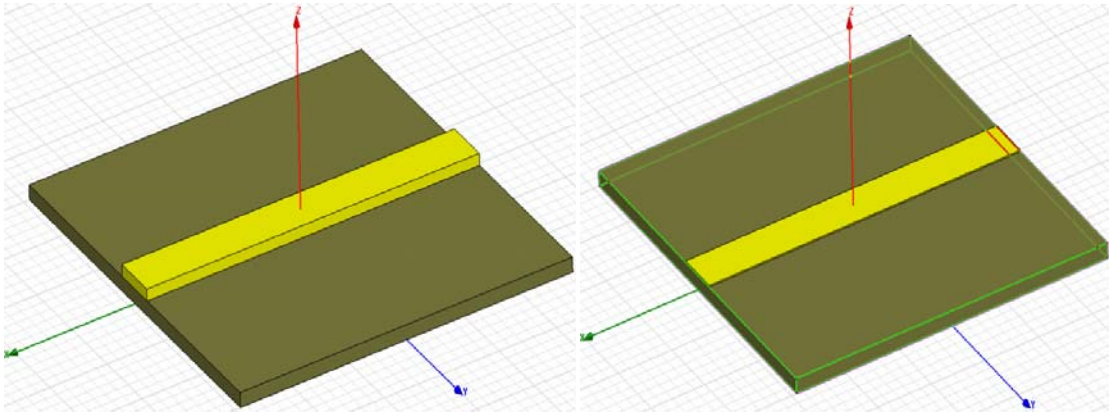

(a) XRL fabricated taller microstrip line (b) Conventional microstrip line

Fig. 3.4 Geometry of the microstrip line.

Both of these structures are simulated under the Driven Modal in Ansoft HFSS. They are covered by the air box with default surface as the prefect electrical boundary confining all the energy inside the box. Two wave ports are defined by attaching both end surfaces of the metal conductor and substrate making sure the energy can pass through from one port to the other. The size of the wave port should be controlled. A large port could excite the waveguide mode since the air box can be assumed as the rectangular waveguide due to the electrical boundary condition outside. If the size is too small, the fields will couple from the conductor trace to the edge of the port walls resulting in inaccurate solutions.

One rule of the thumb for a microstrip line model is that the port width is 10 times wider than the width of conductor trace in case the width of conductor trace is bigger than the substrate thickness; while when the width of conductor trace is smaller than the substrate thickness, the port width should be set as 5 times wider than the width of the conductor trace [58]. The port height should be set about 6~10 times higher than the substrate thickness. Fig. 3.5 demonstrates the correct size of the wave port.

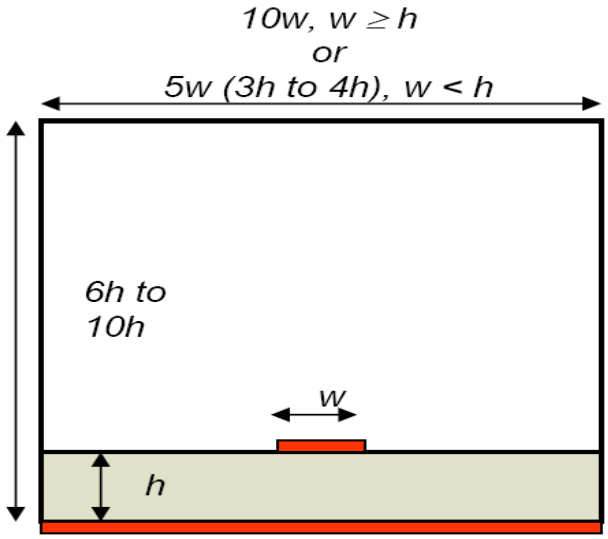

Fig. 3.5 The size of the wave port in the HFSS

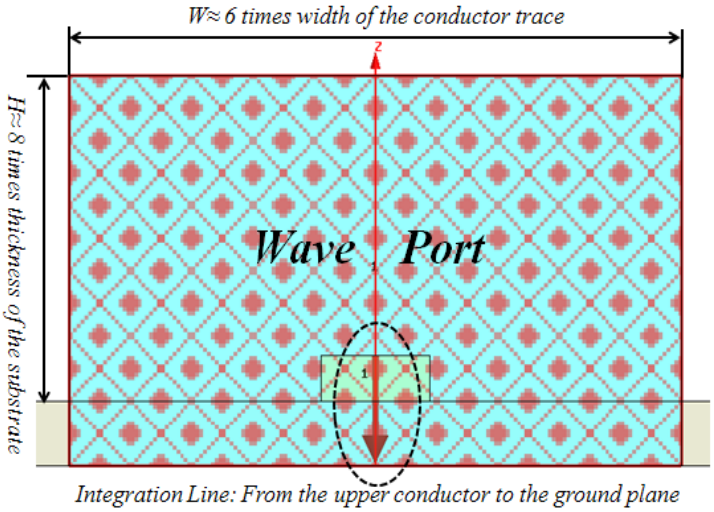

Fig. 3.6 Geometry of the wave port in HFSS

The integration line is to set for calculation purpose. Fig. 3.6 shows the port setting of the tall fabricated microstrip transmission line in HFSS. Fig. 3.7 shows one example of the tetrahedral elements when the height of the metal conductor is 0.7mm. There are 10255 tetrahedrons distributed on the surface of the whole structure. During the simulation, the height and the width of the metal conductor are varied to obtain the different characteristic impedances. Meanwhile, the parameters such as field distribution and effective dielectric constant are under investigation.

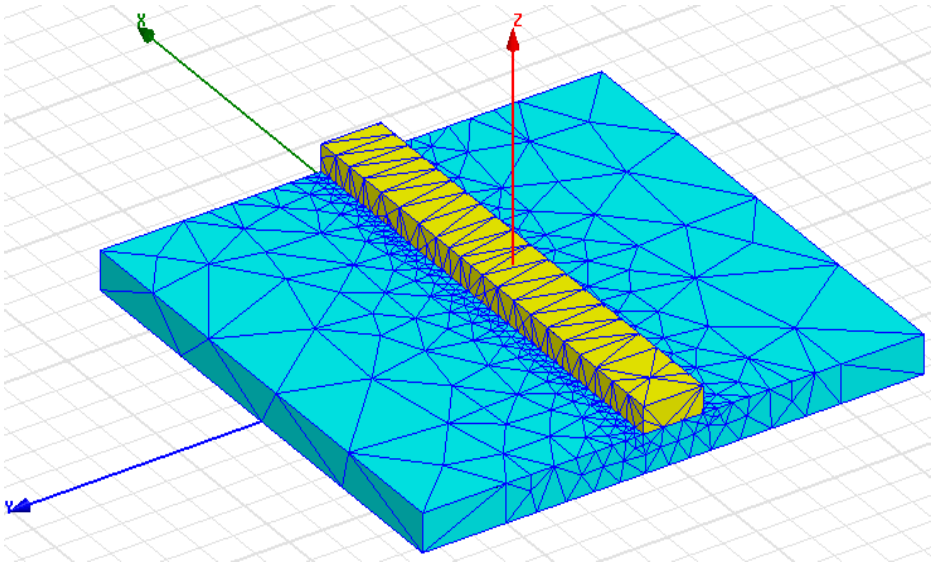

Fig. 3.7 Tetrahedral mesh distribution in HFSS calculation

The field distribution for tall transmission line with conductor thickness of 0.7mm and the conventional microstrip line with conductor thickness of 0.02mm will be compared firstly. Both of these models have the same conductor width which is 1.78mm. The simulated magnitude and vectors of the electric field at 10 GHz for both conventional microstrip line and tall microstrip line are presented in Fig. 3.8 and Fig. 3.9 respectively. Since the tall transmission line has more metal conductor exposed in the air, the magnitude of electrical fields along the tall metal conductor trace above the substrate is concentrated; however, the magnitude of electric field

concentration around the bottom of metal conductor is lower than the thin conductor. This feature results in the higher conductor loss associated with the traditional microstrip line; additionally, simulated vectors of electric field above the substrate for the tall microstrip line are more intensive than the conventional microstrip line indicating the tall microstrip line has higher coupling energy due to the thicker conductor trace. Hence the tall microstrip line can be applied to the structure which requires the lower loss but the higher coupling energy, such as coupler or filter [5]~ [7].

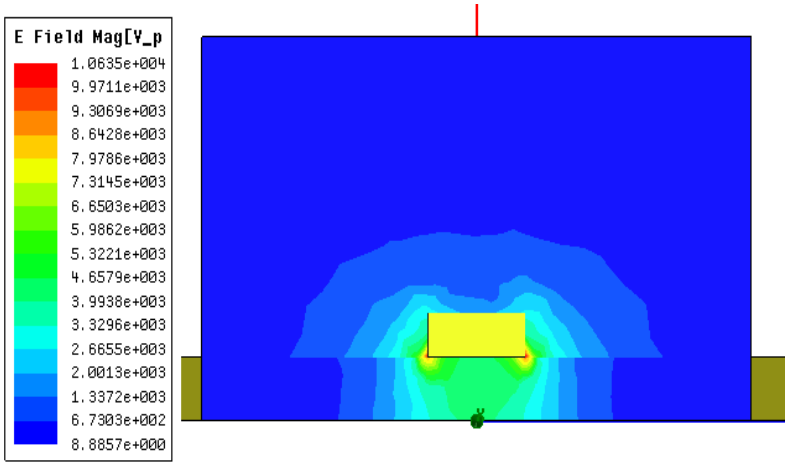

(a) Tall microstrip line

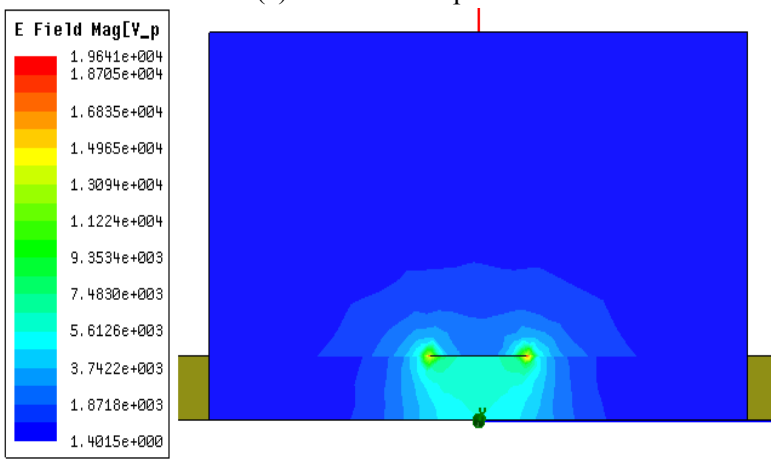

(b) Conventional microstrip line

Fig. 3.8 Magnitude of E-field distribution

Fig. 3.10 illustrates the characteristic impedance of the microstrip line with varying the

conductor width from 0.25mm to 2mm under the different conductor heights of 0.02mm, 0.1mm, 0.2mm, 0.4mm, 0.7mm. The characteristic impedance decreases with increasing the metal conductor width; while for the same metal width, the characteristic impedance decreases with increasing the metal conductor height.

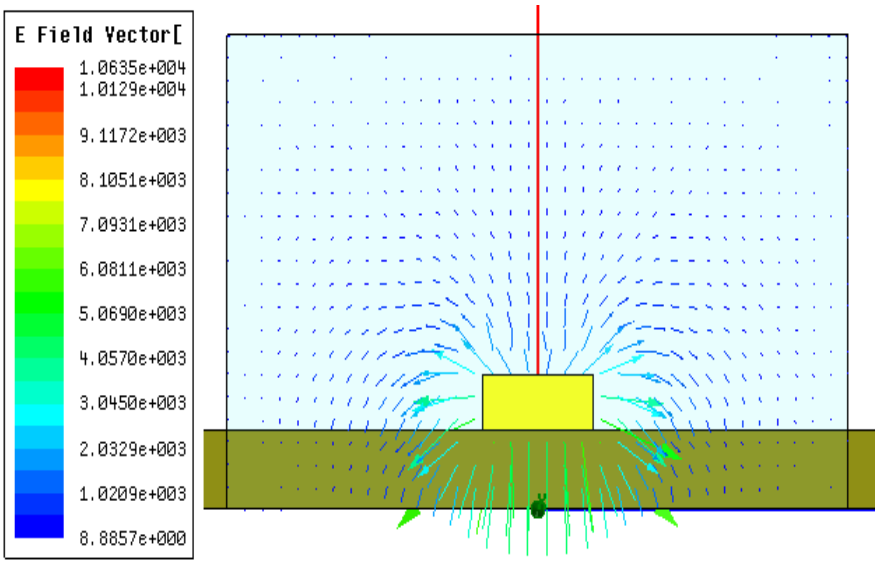

(a) Tall microstrip line

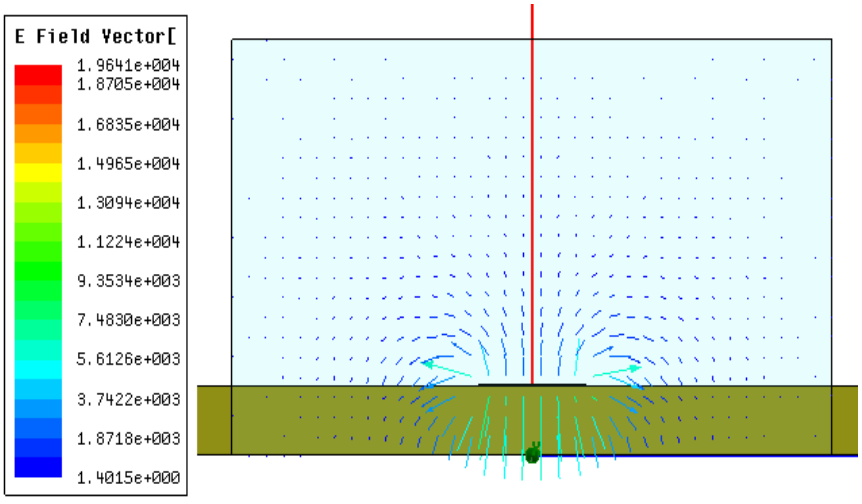

(b) Conventional microstrip line

Fig. 3.9 Electric field vector distribution

The low characteristic impedance can be obtained either by increasing the width of the conductor

trace or by increasing the height of the conductor trace. Since more fields distribute above the substrate when the height of conductor trace is increased, the tall microstrip line with the lower impedance potentially produces high coupling energy, making the objects more laterally compactable.

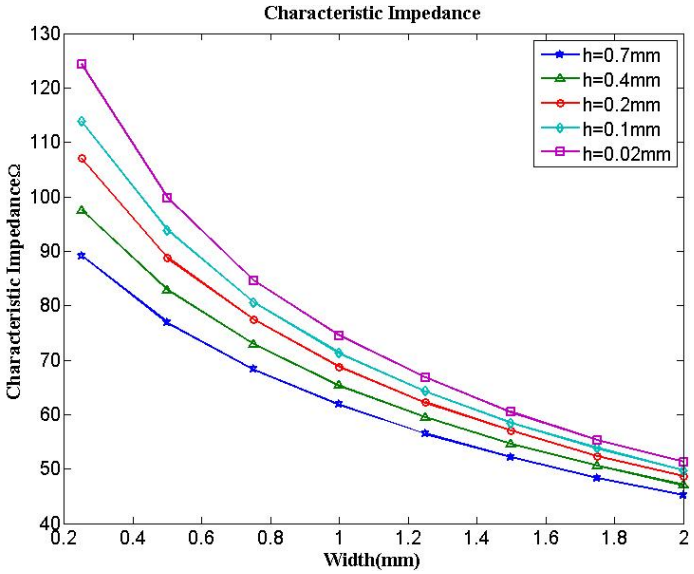

Fig. 3.10 The characteristic impedance of the microstrip line operating at 10 GHz as a function of strip width, *w*, for different height, *h*.

Fig. 3.11 presents the effective dielectric constant under the different heights of the microstrip line. Since more fields distribute above the substrate with increasing the conductor trace, the effective dielectric constant decreases. This fact results in the lower phase constant in Fig. 3.12 when the conductor height is increased.

The attenuation constant can be obtained from the complex propagation constant γ available directly in the HFSS solution [59]. The propagation constant is given by equation (3.3).

$$\gamma = \alpha + j\beta \tag{3.3}$$

where the real part α is the attenuation constant of the signal propagating through the

transmission line. The imaginary part β is the propagation phase constant. Fig. 3.13 presents the results of the attenuation constant variations when the height of the microstrip line is increasing. For the fixed conductor width, when the conductor height increases, the attenuation constant decreases. This is mainly because the higher current density distributes at the bottom of the thinner conductor trace compared to the taller case. The lower attenuation constant values are associated with the lower losses for the tall microstrip line model.

Additionally, the propagation phase constant β can be obtained directly in HFSS by calculating the imaginary part of propagation constant as shown in Fig. 3.12.

Fig. 3.14(a) is the top view of a microstrip line fabricated using deep XRL with electroplating. The metal conductor is nickel and the substrate is quartz glass. The measured average height of the metal conductor is 287μm and the substrate thickness is 500μm. In this research, the height of the conductor trace can be measured by taking the average of three independent measurements on the same conductor trace at the middle and the two end points. Fig. 3.14(b) shows the details of the corner of the microstrip line, measured under the microscope Zeiss Axiotron 1 (see the Fig. 3.15).

From the discussion above, XRL fabricated tall microstrip line is a good candidate which can be applied to microwave and millimeter wave circuit design due to its unique characteristics such as the higher coupling energy and lower loss. In addition, circuits such as filters and couplers which are fabricated by XRL can achieve excellent performance and offer precise dimension and compact lateral structure due to the higher coupling energy [5],[6],[9].

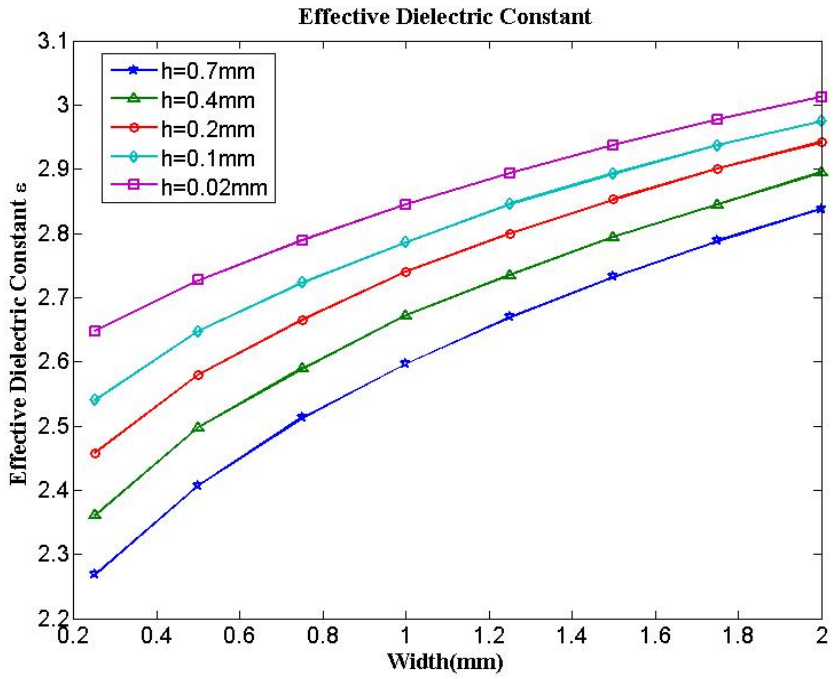

Fig. 3.11 Effective dielectric constant at 10 GHz of the different height microstrip line as a function of strip width, *w*, for different height, *h*.

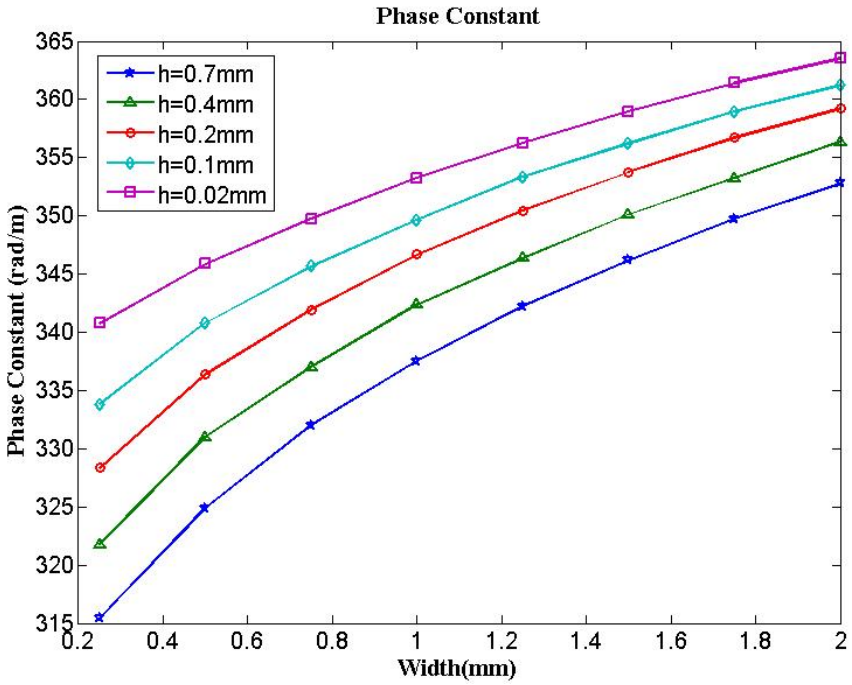

Fig. 3.12 Phase constant at 10 GHz of different height of the microstrip line as a function of strip width, *w*, for different height, *h*.

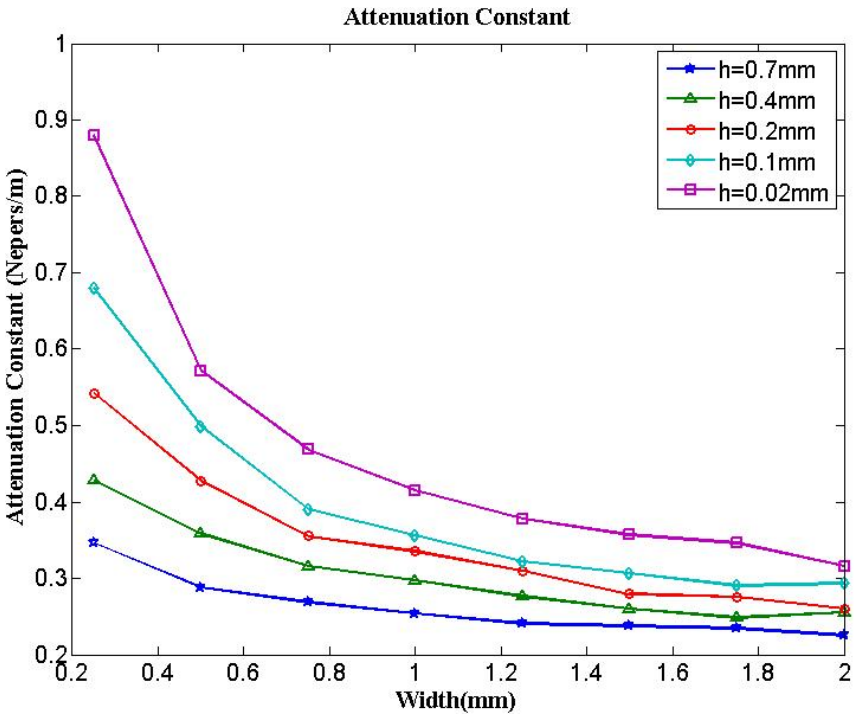

Fig. 3.13 Attenuation constant at 10 GHz of different height of the microstrip line as a function of strip width, *w*, for different height, *h*.

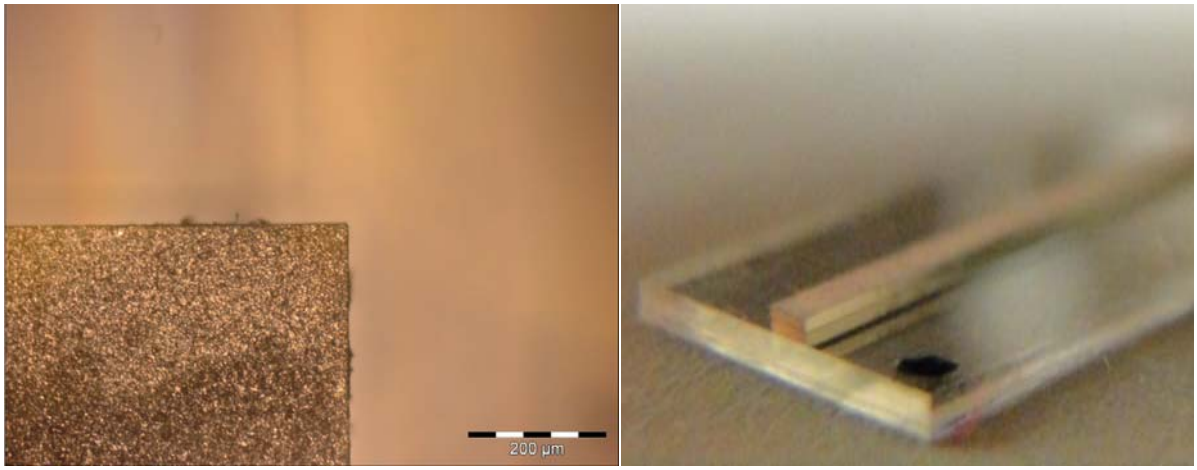

(a) Top view (b) Side view

Fig. 3.14 XRL fabricated tall microstrip line

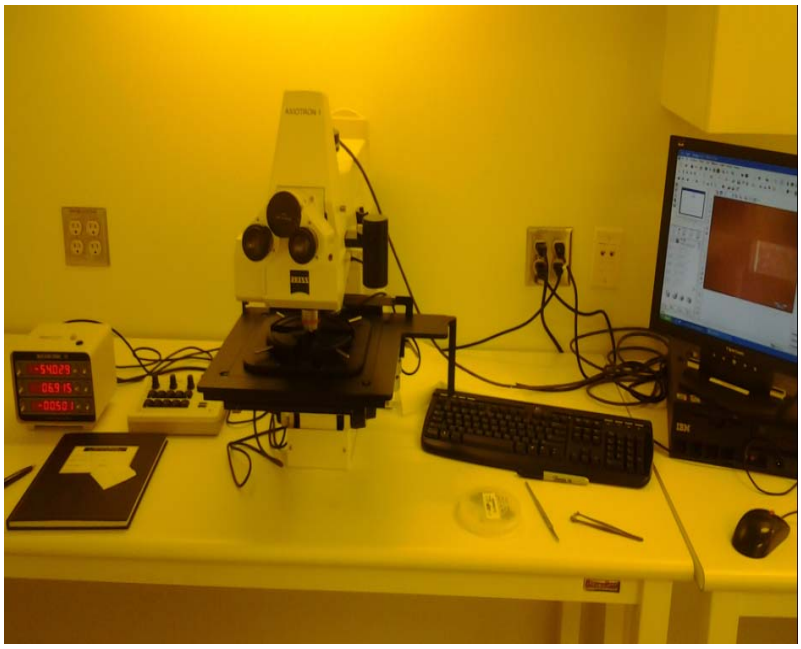

Fig. 3.15 Measurement platform: Zeiss Axiotron 1 Microscope

Chapter 4
New Feeding Scheme for Low Permittivity Rectangular DRA

4.1 Motivation and Introduction

In the last two chapters, the properties and characteristics of the DRA as well as the deep XRL fabricated tall microstrip line have been investigated. In this chapter, how to utilize the advantages of the tall microstrip line to excite the DRA with low permittivity ($\varepsilon_r \leq 10$) and compose the novel feeding structure is under investigation.

For the novel feeding scheme, it not only inherits advantages of the tall microstrip line such as lower loss but also can more easily excite the DRA as well as integrate with other tall microstrip circuits. In this chapter, there are two new feeding structures presented and one evolving structure will be proposed and investigated by using the FEM based Ansoft HFSS software.

4.2 Analysis of New Feeding Structure

4.2.1 Introduction

In chapter 2, four popular common feeding schemes have been illustrated and analyzed. Among these traditional feeding structures, the simplest one is the microstrip line feeding structure. Theoretically, the coupling intensity by using the microstrip feeding is decided by two factors, one is the distance to the microstrip line and another one is the dielectric constant of the DRA

element. However, since more fields distribute above the substrate if the feeding line becomes thicker, more coupling energy can be created.

Furthermore, coupling intensity is also decided by the dielectric constant of the DRA; the stronger coupling energy can be achieved when the DRA with high permittivity (ε_r>20) is applied. However, If the dielectric constant is low (ε_r≤10), the coupling intensity is too low to excite the DRA, making this simplest feeding scheme difficult to apply practically. R.K. Mongia in [36] illustrates that it is not possible to obtain critical coupling by using the planar microstrip line feeding if the RDRA has a permittivity value lower than 20. However, XRL fabricated tall microstrip line can remedy these drawbacks due to its special advantages. The vertical and thick metal conductor trace can produce more fields bringing more coupling energy which can compensate for the lower permittivity value of the DRA.

4.2.2 Side Coupling Feeding Scheme

The first feeding method is side-coupling. Its configuration is similar to the conventional microstrip line feeding structure. The RDRA is placed at the region of the maximum electric field or magnetic field adjacent to the transmission line to achieve the maximum coupling energy and excite the dominant mode. The DRA with permittivity of 20 and 10 are analyzed; during the simulation, the microstrip feeding line with different aspect ratios is under investigation to verify the performance of the proposed feeding structure. Fig. 4.1 shows the geometry of this feeding model in Ansoft HFSS.

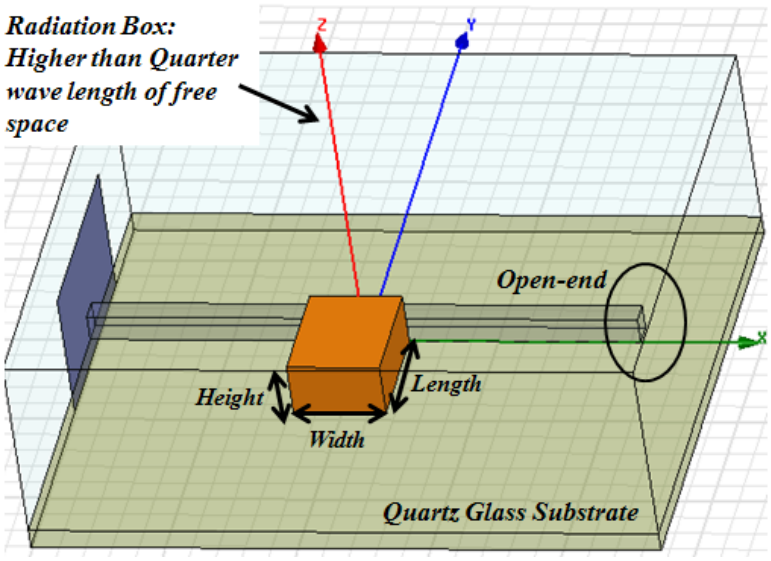

Fig. 4.1 Geometry of the side-coupling feeding scheme on RDRA

The open end tall microstrip line is placed on a 1.5 mm thick quartz glass substrate. The RDRA with dimensions 7 mm*9 mm*4 mm (W*L*H) is placed aside of the microstrip line.

For the first case, the RDRA with permittivity of 20 is analyzed. In order to achieve the maximum coupling energy, the RDRA is assumed to contact the metal conductor trace, and is moved from the open end point along the transmission line until obtaining the critical coupling which achieves the best return loss. Since high coupling intensity can be anticipated due to the high dielectric constant, this RDRA element could be excited using the traditional planar microstrip line. Theoretical computation shows the resonant frequency of the dominant mode for the single RDRA with the dimension of 7 mm*9 mm*4 mm (W*L*H) is 6.45GHz compared with the simulated resonant frequency 6.93GHz in HFSS. Since this RDRA is loaded by the planar microstrip line in HFSS, the resonant frequency under the dominant mode presents a difference of 7.44%. Fig. 4.2 presents the simulated H-field vector distribution for both the feeding line and RDRA. It can be seen that the magnetic field inside the RDRA coincides with

that of the microstrip line to achieve a strong coupling.

The reflection coefficient is lower than -20dB as shown in Fig. 4.3. The 10dB fractional bandwidth can be defined as the bandwidth at the return loss of -10dB divided by its central frequency. The simulation results show the 10dB bandwidth is about 6.13%, relatively narrow due to the DRA with high dielectric constant.

TE^{x}_{111} as the dominant mode in this case is excited making the field distribution like the short horizontal magnetic dipole. Fig. 4.4 (a) and (b) present the dominant mode field distribution of the RDRA for both the E-field and H-field. Fig. 4.5 (a) and (b) give the radiation pattern for E-plane and H-plane respectively. It can be seen that the gain value is about 6.8dB and the cross-polarization is about 36.53dB below the co-polarization.

In HFSS, there are two gains: gain and realized gain. Both of them have their individual meanings. The first parameter of gain is 4π times the ratio of the radiation intensity, U, for an antenna in a given direction to the total power accepted, P_{accept} , by the antenna and is presented in equation (4.1).

$$Gain = \frac{4 \times \pi \times U}{P_{accept}} \tag{4.1}$$

The realized gain is presented in equation (4.2) as below:

$$Gain_{realized} = \frac{4 \times \pi \times U}{P_{incident}} \tag{4.2}$$

The difference between these two parameters is the power. The accepted power in equation (4.1) does not consider the reflected power from the antenna; while the incident power, P_{incident} , in realized gain is the total power which is received by antenna. Since the realized gain includes the

reflected power at the end of antenna, it is closer to the measured gain in the chamber as the practice; while the gain value meets the gain definition in [64]. However, once the return loss at the input port of antenna is lower than -10dB delivering more than 90% energy to the antenna, the difference between these two gain parameters can be ignored. In this case the gain value is about 6.7982dB comparing with 6.699dB of the realized gain, which is smaller than 0.1dB difference. So in the following simulation, the gain value will be presented to describe the radiation quality of the DRA.

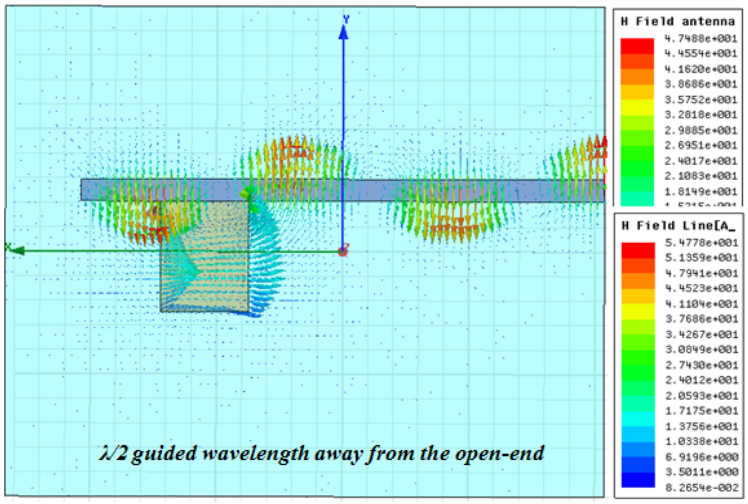

Fig. 4.2 Simulated H-field vector distribution for both of the microstrip line and RDRA

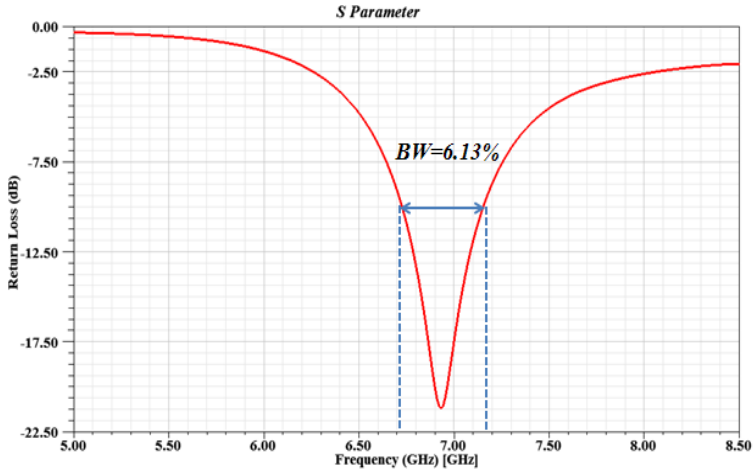

Fig. 4.3 Return loss in dB of the side coupling feeding structure of RDRA with permittivity of 20.

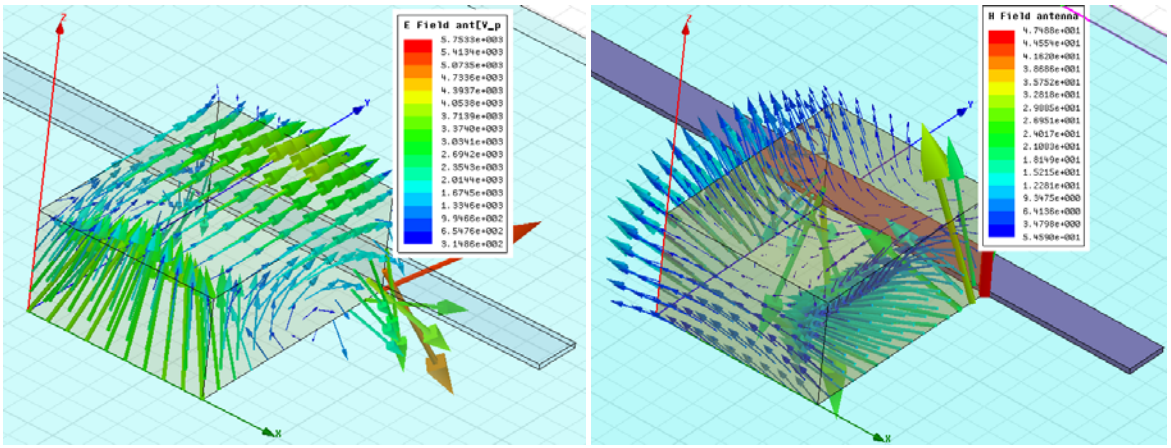

(a) E-field distribution (b) H-field distribution

Fig. 4.4 RDRA field distribution of the dominant mode

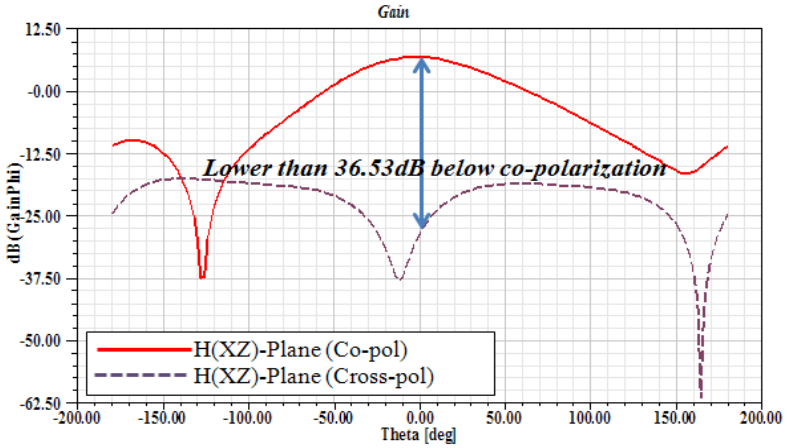

(a) H(XZ)-Plane

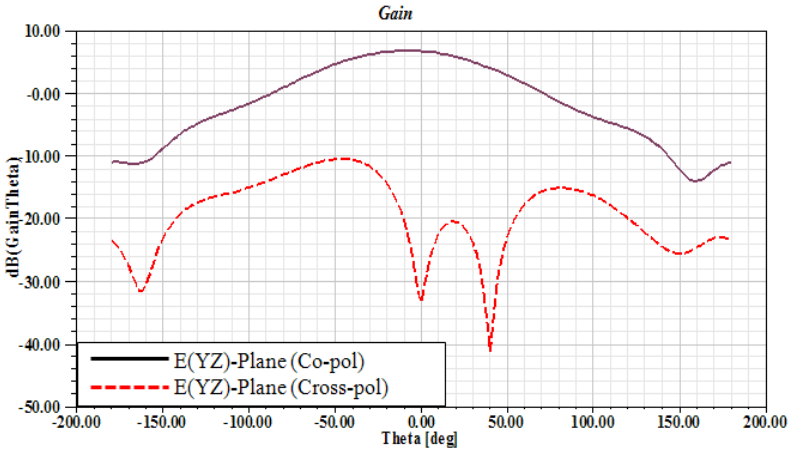

(b) E(YZ)-Plane

Fig. 4.5 The radiation pattern of the side-coupling scheme of RDRA with permittivity of 20

In the second case, the dielectric constant is decreased from 20 to 10, but the RDRA has the same

dimensions. The coupling level becomes weaker due to the lower dielectric constant value. In order to excite the RDRA effectively, the thickness of the feeding line is increased; besides, the position along the tall microstrip line will be varied to obtain the critical coupling.

The computation of the resonant frequency using equations (2.8), (2.9), (2.10) in Chapter 2 is 9.02GHz; however, the simulated resonant frequency in HFSS is about 7.77GHz, which is 13.8% lower than the theoretical result. The reason is because of the tall feeding line. In this case, in order to achieve more coupling from feeding line, the height of the conductor trace increases to 1.5mm which is close to the half of the RDRA height. Since the contact area between the RDRA and the tall feed line is much larger, the conductor trace is not only loading the RDRA but also appearing as prefect-E wall. Based on the image theory, the effective dimension of the RDRA under simulation case appears larger than in the theoretical computation. This unique characteristic can make the size of the RDRA more compact with using tall microstrip line feeding. On the other hand, the critical coupling is not generally obtainable for DRAs with low permittivity value ($\varepsilon<10$) if the simple planar microstrip line is applied, making the traditional feeding scheme less effective in practice for excitation [38]. However, results for the return loss presented in Fig. 4.6 show good matching using the tall microstrip line feeding scheme, even for the low permittivity DRA. As shown, since the DRA permittivity changes dramatically from 20 to 10, it is clear that the resonance frequency and the bandwidth increase as the permittivity of DRA decreases [32], however, the resonance frequency does not increase dramatically as expected, due to the miniaturization effects of the tall feeding line. The return loss in dB is lower than -14dB and the 10dB bandwidth is 10.54% which is wider than in the first case.

The radiation patters for both the E-plane and H-plane are presented in Fig. 4.7(a)&(b). The gain is about 6.1dB and the cross-polarization is 17dB lower than the co-polarization. The radiation pattern shows good symmetry due to the symmetrical feeding structure in which the RDRA is placed near the center part of the tall microstrip line. Under this feeding scheme, the dominant mode TE^{x}_{111} can be excited and shown in Fig. 4.8(a),(b),(c). The field distribution is similar to the RDRA dominant mode descriptions in Chapter 2.

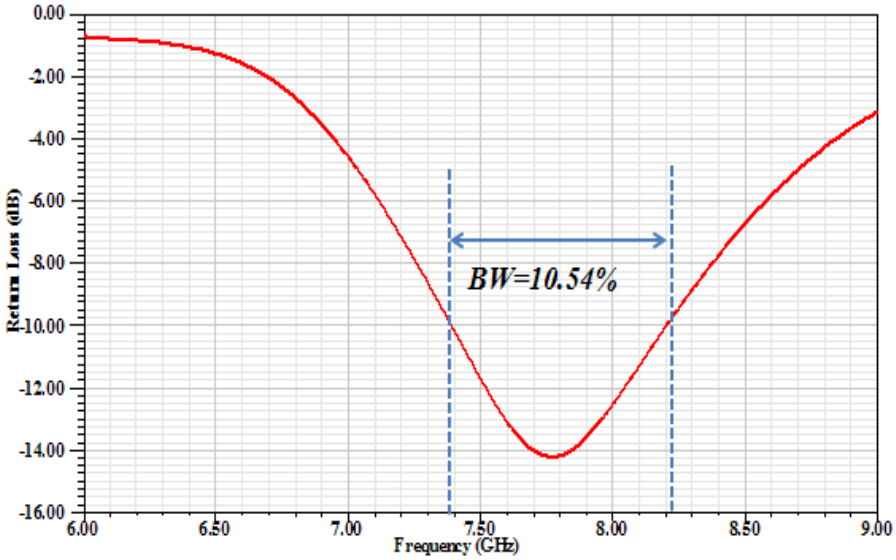

Fig. 4.6 Return loss of the side coupling feeding structure of RDRA with permittivity of 10.

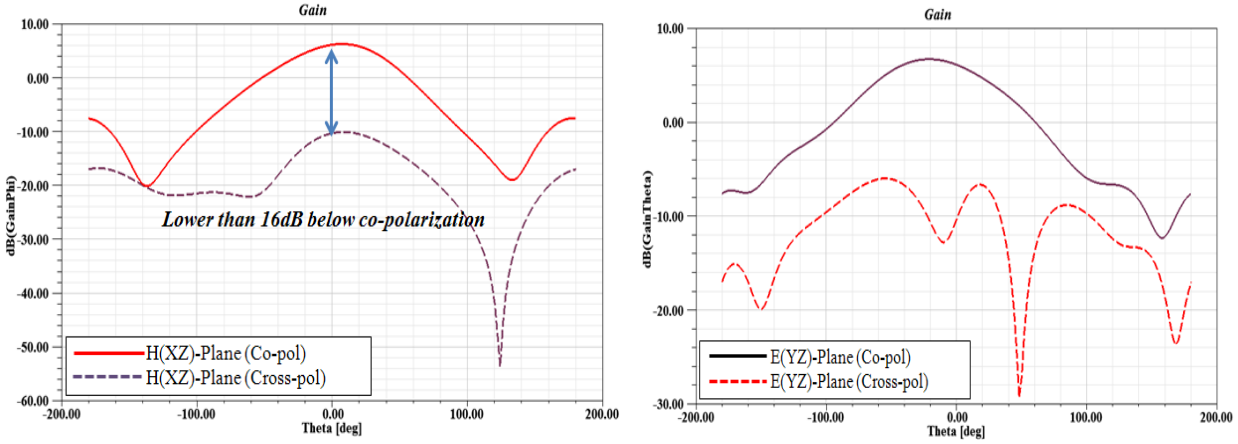

(a) H(XZ)-Plane (b) E(YZ)-Plane

Fig. 4.7 The radiation pattern of the side-coupling scheme of RDRA which permittivity is 10

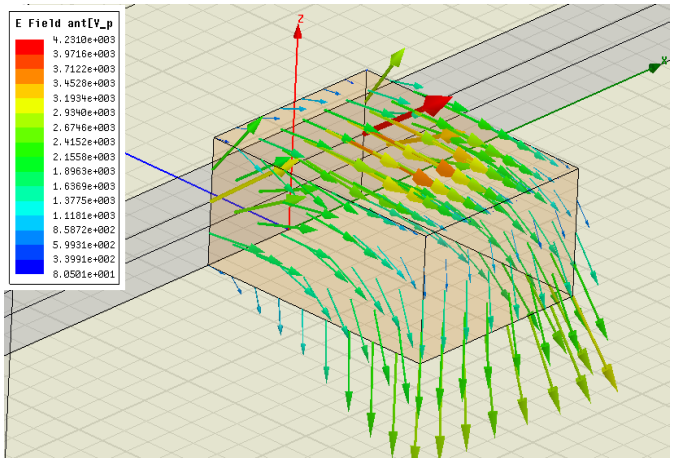

(a) E-field distribution of the RDRA

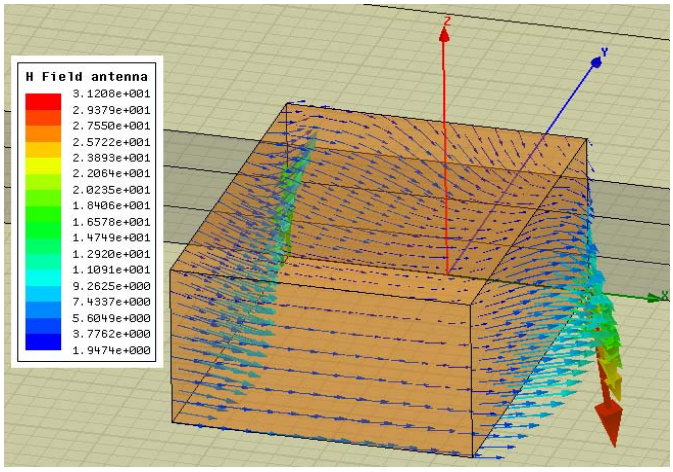

(b) H-field distribution of the RDRA

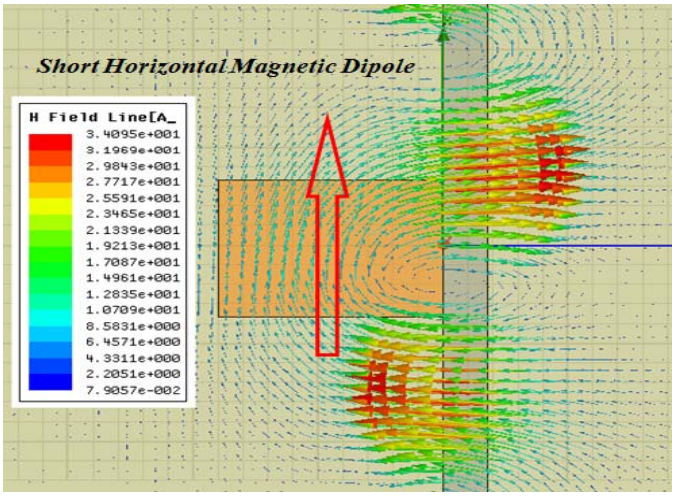

(c) H-field distribution of the tall microstrip line

Fig. 4.8 Field distribution of the dominant mode TE^{x}_{111} of RDRA with permittivity of 10

4.2.3 Direct Coupling Feeding Scheme

For microstrip line feeding, an alternative approach is to place the RDRA at the end of the open end point of the microstrip line where the maximum electric field occurs. This is called direct feeding scheme [51]. This feeding structure is normally applied to excite the HE_{111} mode of the cylindrical DRA. It is also possible to excite the RDRA, since the thin metal conductor trace, but only for high permittivity values (ε_r>>10) as described in [36] if restricted to simple planar metal feeding lines.

Many researchers attempt to improve the performance of the direct feeding structure for low permittivity DRA; however, these techniques sometimes make the structures complicated, for example, by combining the high permittivity material with the low permittivity material together to produce hybrid DRA in [61] or by modifying the feeding line into the step formation and combining a patch antenna on the top surface of the RDRA in [62].

In the last chapter, the properties of the XRL fabricated tall microstrip line were analyzed. Since more fields distribute above the substrate, good performance could be obtained when applied to side-coupling feeding structure. However, high field intensity can also be anticipated at the end of the open end point due to the thicker conductor trace. So an alternative structure is to place the RDRA at the end of the open end position. By utilizing the fields distributing around the open circuit end, the RDRA with lower permittivity value can be excited effectively; furthermore, by optimizing the dimension of the feeding line, good matching conditions can be achieved.

Fig. 4.9 shows this feeding structure in HFSS software. An example RDRA with permittivity of 5

is placed at the end of the open-end tall microstrip line. The dimensions of the RDRA are 3.1mm*3.3mm*1.7mm (L*W*H). The metal trace is placed on a quartz glass substrate with thickness of 1mm. The dimensions of the metal conductor trace, such as width, length and thickness are modified until the desired RF performance as well as the excellent radiation performance can be achieved.

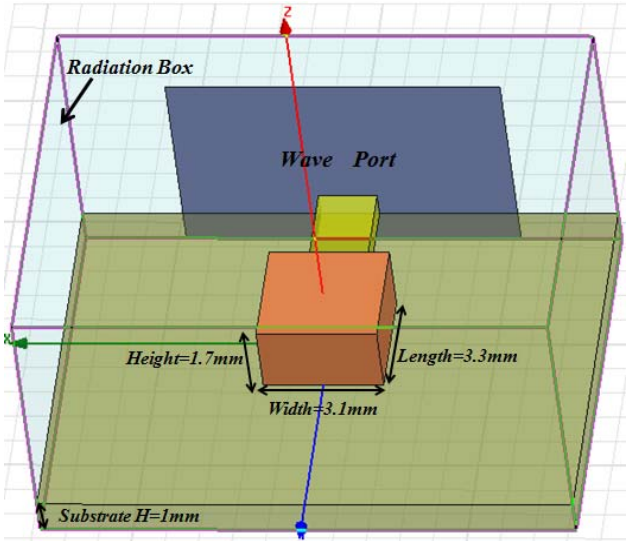

Fig. 4.9 Geometry of the direct feeding structure of RDRA with permittivity of 5

The resonant frequency which is obtained through calculation using equations (2.8), (2.9), (2.10) in chapter 2 is about 27.41GHz compared to 23.84GHz in HFSS simulation results. The reasons of the frequency deviation are similar to those descriptions in section 4.2.2. Since coupling capacity is not only decided by the length of the feeding line, but also can be tuned through adjusting its aspect ratio, this feeding structure can be more effective than the side coupling feeding scheme. Additionally, by optimizing the dimensions of the feeding line, the matching condition can be optimized through cancelling out the reactive components at the feeding point impedance.

As shown in Fig. 4.10(a) and (b), the input impedance at the resonant frequency equals to

50-*j*3.35Ω, a real part of 50Ω and an imaginary part close to zero, resulting in an excellent matching condition. The return loss is lower than -25dB at the center frequency and the 10dB bandwidth is about 25.59% which is greatly enhanced due to the low permittivity.

Fig. 4.11(a)&(b) gives the radiation pattern. The gain is 4.9dB and the cross-polarization is -40dB lower than the co-polarization. It is worth to note that the radiation pattern in the theta direction is symmetrical due to the symmetry with respect to the feeding point. Fig. 4.12 (a)&(b)

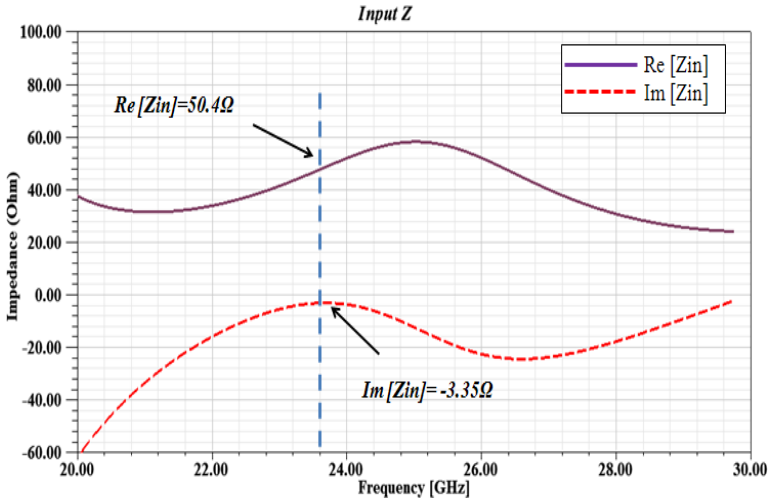

(a) Input impedance

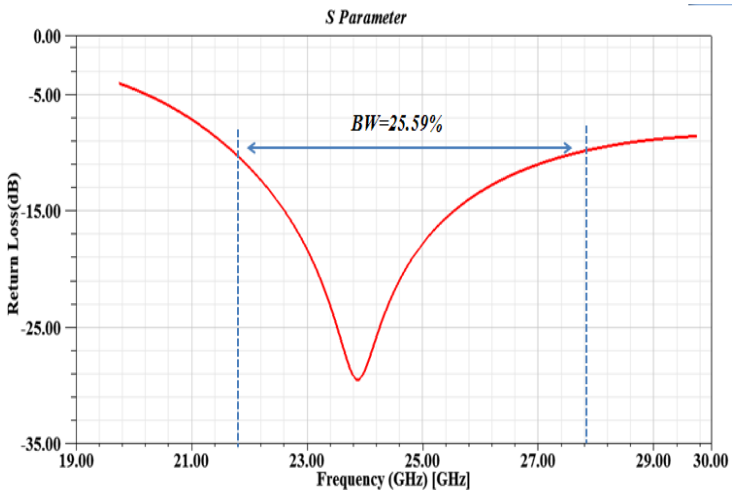

(b) Return loss in dB

Fig. 4.10 Analysis of the direct feeding structure of RDRA with permittivity of 5.

give the simulated field distribution. It can be seen that strong capacitive coupling can be created at the end of the open-end tall microstrip line and the lowest mode TE^{x}_{111} mode can be excited making it radiate similar to a short magnetic dipole.

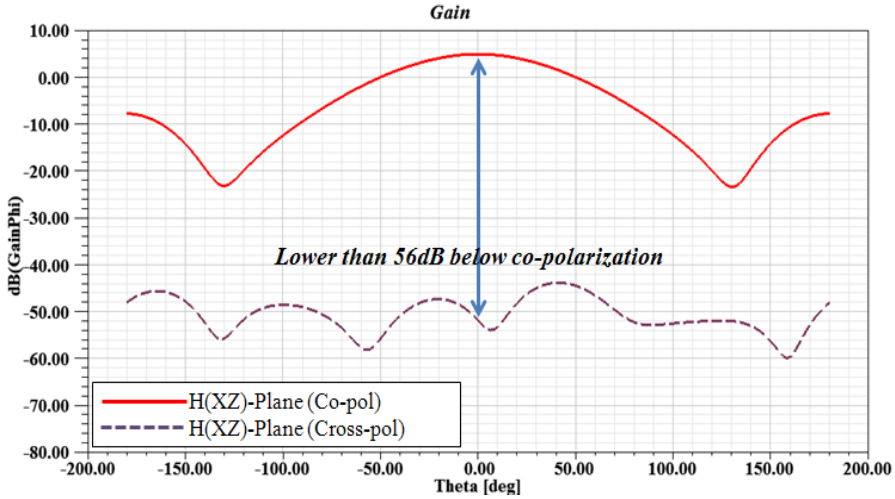

(a) H(XZ)-Plane

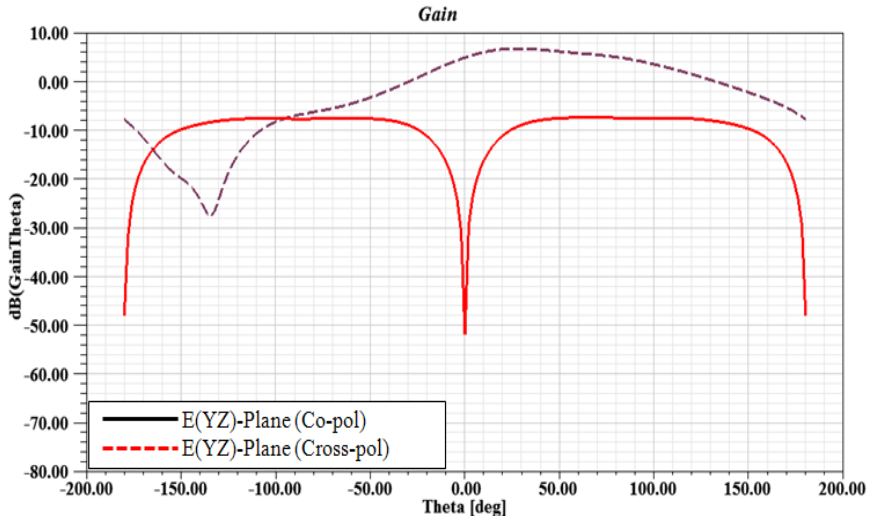

(b) E(YZ)-Plane

Fig. 4.11 The radiation pattern of direct scheme of RDRA with permittivity of 5

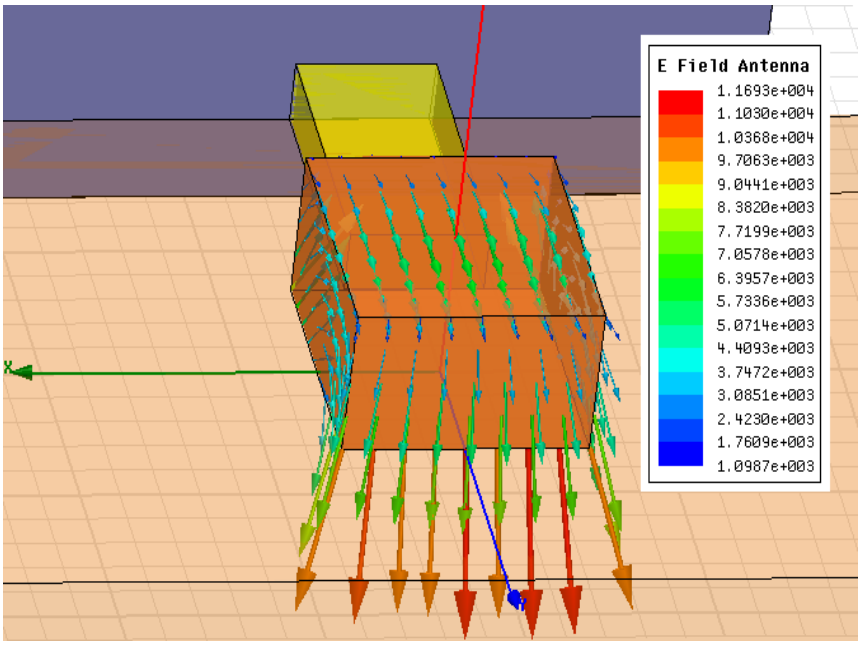

(a) Simulated E-field vectors distribution of the RDRA

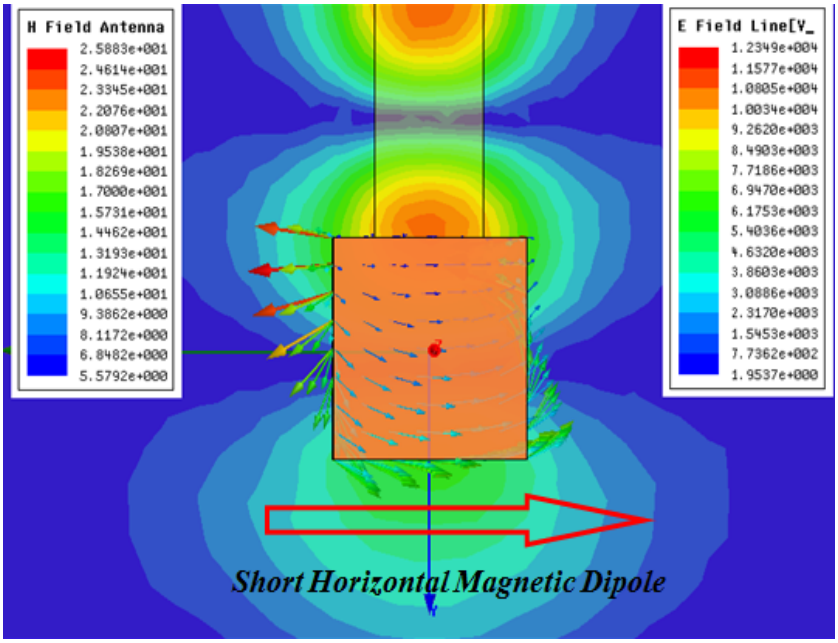

(b) Simulated H-field vector distribution of the RDRA and the magnitude of E-field distribution of the feeding line

Fig. 4.12 Fields distribution of direct feeding scheme of RDRA with permittivity of 5

4.2.4 The T-Shape Feeding Scheme

For the T shape feeding structure, not only can it excite the DRA with the low permittivity as in the previous feeding schemes, but can also be effective and simpler to apply to practical applications, for instance the linear series-fed array design.

Fig. 4.13 illustrates the geometry of this feeding scheme. For analysis, the DRA is located at the end of the open-stub line. Since the tall transmission line is applied to excite the low permittivity DRA element, this T shape open stub line is terminated by a tall short circuit transmission line placed on 1mm thick quartz glass substrate to avoid the end radiation. The T shape open stub line is located roughly at the 3/4 guided wavelength position away from the short end, making this appear as an open circuit to the T stub, resulting in minimal loading.

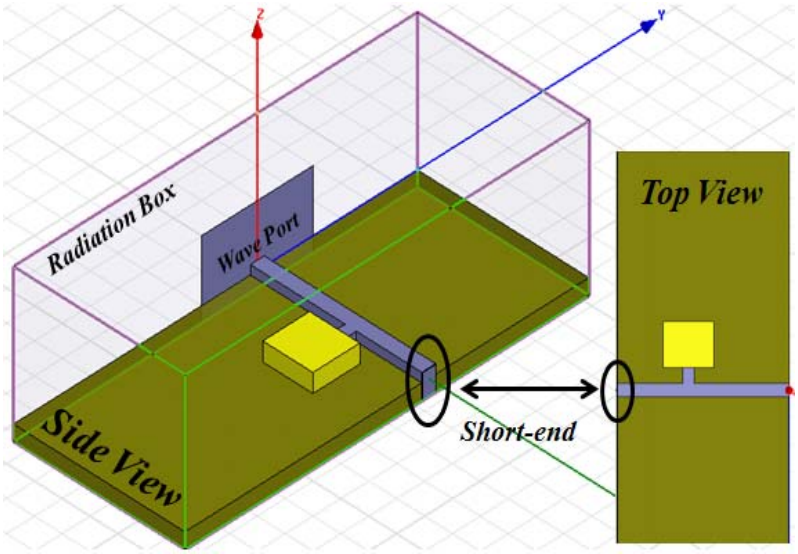

Fig. 4.13 Geometry of the T shaped novel feeding scheme

In addition, the parasitic capacitor between the open stub feeding line and the RDRA due to the high E field intensity at the open end point will shift the resonant frequency. Ideally, once the

DRA operates at the resonant frequency, through optimizing the dimensions of the T shape open stub line, the reactances of the T shape open stub line and the short end 3/4 guided wavelength transmission line can be cancelled out leaving only a real impedance at the feed point. This process can be achieved through simulation or experimental measurements, by observing the best response in S_{11}. In this research, since the dimensions of the DRA are fixed in HFSS, some critical parameters such as the dimensions of the open stub line (width, length and thickness) are tuned in HFSS until good matching condition as well as radiation performance, is obtained.

Fig. 4.14 (a)&(b) give the results for both simulated return loss and the input impedance. The S_{11} is lower than -37dB operating at the 23.46GHz and the 10dB bandwidth is wider than 35% covering from 20GHz to 27.58GHz. The bandwidth is greatly enhanced due to the lower permittivity value of the DRA. The input impedance is 64-*j*1.86Ω with imaginary part close to zero at the resonant frequency.

Furthermore, through tuning the dimensions of the open stub line, not only can the imaginary parts be cancelled out, but also the critical coupling can be obtained. The gain value of this T shape feeding structure showing in Fig. 4.15 is about 4dB and the cross-polarization is 20dB lower than the co-polarization.

Fig. 4.16(a),(b)&(c) present the field distribution. Fig. 4.16(a) and (b) show both simulated vectors distribution of the E-field and the H-field of the RDRA respectively. The TE_{111}^{x} mode as the dominant mode which satisfies the description of RDRA dominant mode distribution in chapter 2 can be excited at the end of the open stub line. Fig. 4.16(c) gives the simulated magnitude of the E-field of the feeding line. It can be seen that the open stub line is located at the

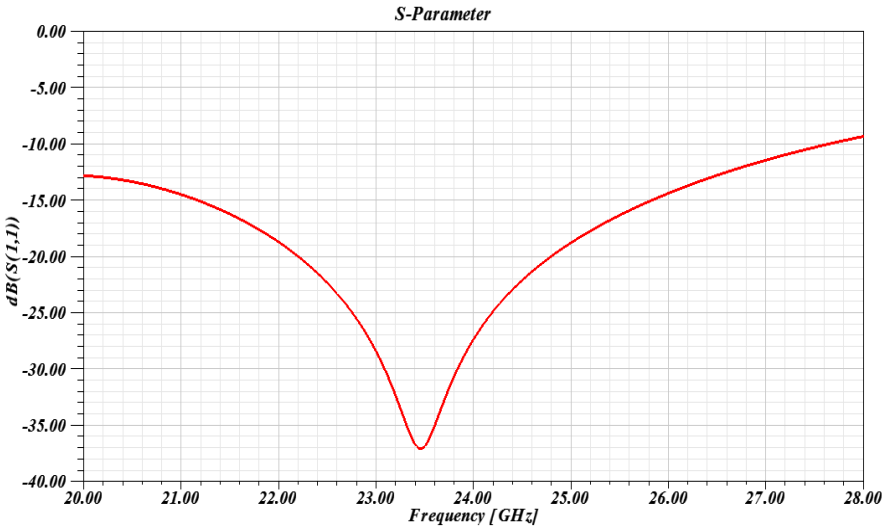

(a) Return loss in dB

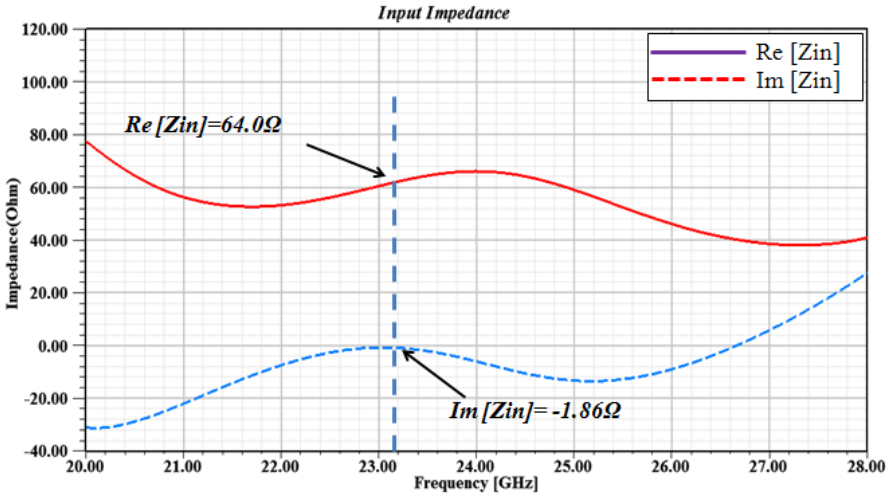

(b) Input impedance

Fig. 4.14 Analysis of the T shape feeding structure of RDRA with permittivity of 5.

maximum E-field position which is 3/4 guided wavelength away from the short end point. Meanwhile, the dimensions of the open stub line (width, length and thickness) can be adjusted to control the currents distribution to obtain the different coupling level. This advantage can make this novel feeding structure a good feeding mechanism applied to linear DRA array design. Through controlling the current distribution of the linear array, the side-lobes can be well adjusted to obtain the desired radiation patterns.

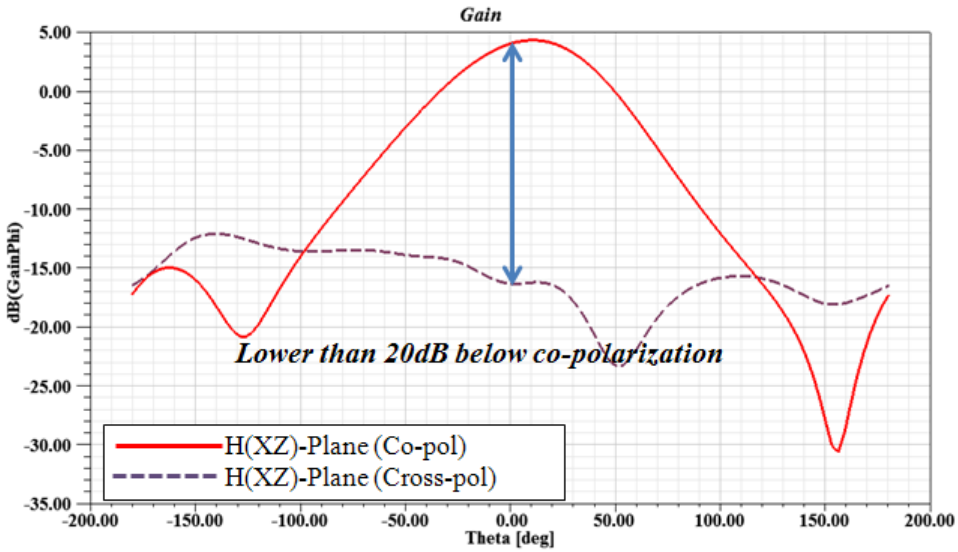

(a) H(XZ)-Plane

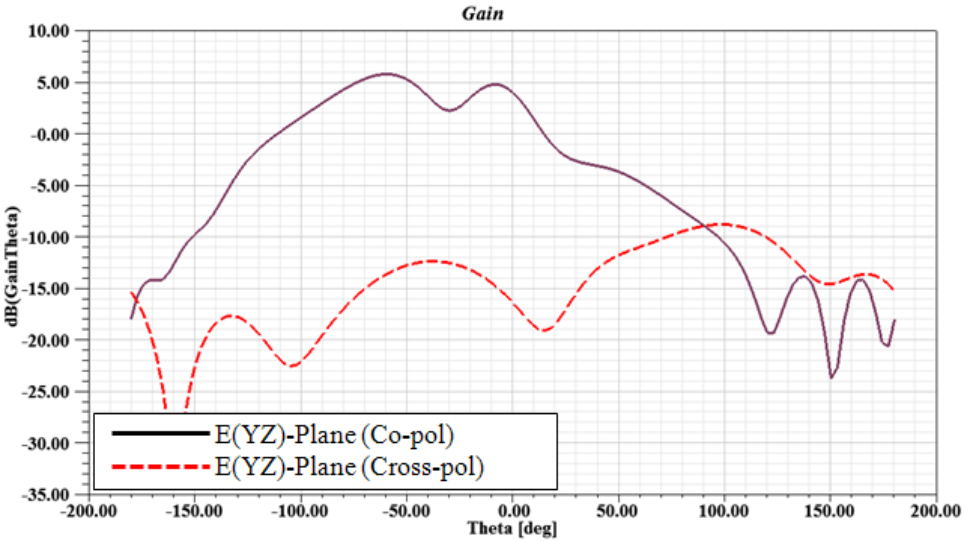

(b) E(YZ)-Plane

Fig. 4.15 Radiation pattern of the T shaped feeding structure of DRA with permittivity is 5

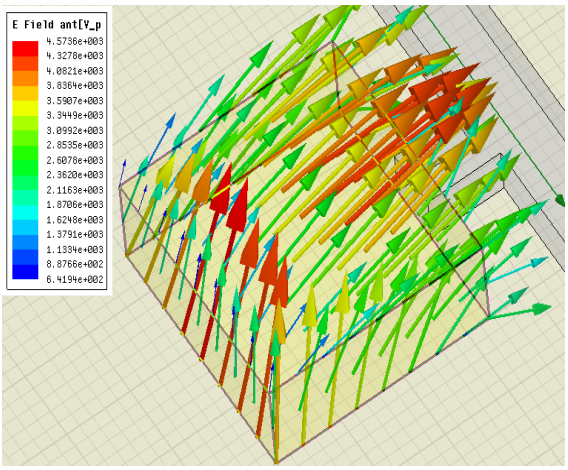

(a) Vector of the E-field distribution of the DRA

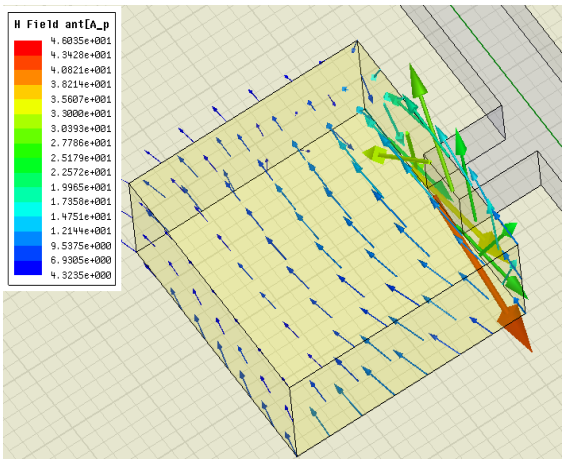

(b) Vector of the H-field distribution of DRA

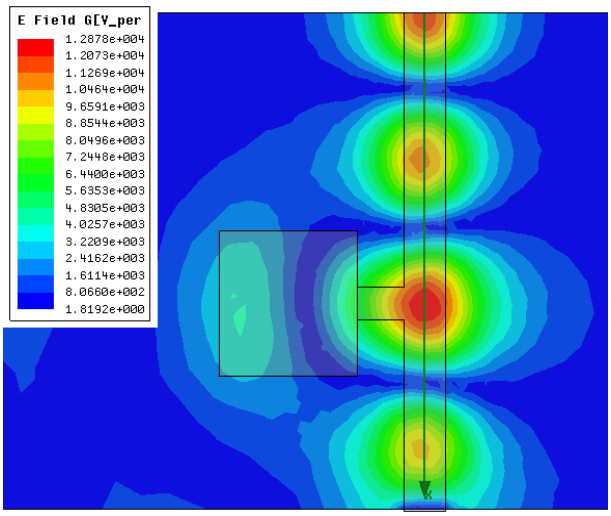

(c) Magnitude of the E-field distribution of the tall microstrip line

Fig. 4.16 Field distribution of the T shaped feeding scheme of DRA with permittivity is 5

4.3 Measurements and Analysis

In this research due to cost and time constraints, dedicated fabrications for both tall transmission lines and also the DRA samples were not feasible. However, representative tall metal transmission lines and polymer-ceramic composite DRA devices of similar dimensions and fabricated using deep XRL were available in the research group from other PhD students (Himal Jayatilaka, Mohammadreza Tayfeh Aligodarz). Though not optimal for this research, these devices could still be used experimentally to demonstrate the feasibility of the tall feeding structure proposed. Two different DRA samples are excited to demonstrate the feasibility of the tall feeding scheme by experimentation. Although the dimensions for both tall transmission line and DRA samples are different than the simulation models in HFSS presented in previous section in this chapter, these new models are re-simulated in HFSS here, and both simulation and experimental results confirm the effectiveness of the deep XRL made tall transmission line on exciting the low permittivity DRA sample. Since the side-coupling feeding scheme is the simplest structure, the experiments and verification works focus on this feeding scheme.

The side coupling feeding structure is composed of the tall transmission line using available tall microstrip lines fabricated using deep XRL. The conductor trace and the substrate are of nickel and quartz glass respectively. The average height of the conductor trace is about 0.29 mm which is measured by using Zeiss Axiotron 1 Microscope and the substrate thickness is 0.5 mm. The bottom of the substrate is grounded by silver glue pasted on an aluminum block and the tall microstrip line connected with a 3.5mm SMA connector. Fig. 4.17 gives this feeding structure.

Two low permittivity DRA samples are under investigation. The first one used for comparison is cut from Rogers 3010 substrate with permittivity of 10.2. The dimension is 5mm*5mm*1.27mm (W*L*H); the second one is fabricated by deep XRL technology using a polymer ceramic composite material with permittivity of approximately 8 and the dimension of 4.55mm*4.60mm*1.29mm (W*L*H). Fig. 4.18 presents the pictures deep XRL DRA samples.

The feeding structure was connected to the Agilent 8722ES network analyzer using a HP 2.4mm-3.5mm flexible test port cable to measure the input reflection coefficient. During the measurement, the DRA sample was placed aside the feeding line, in contact with it and moved from the end of open circuit until the desired reflection coefficient is obtained. Fig. 4.19 shows the test platform and its configuration.

In the first case, the DRA was placed around half guided wavelength away from the open-end circuit near the expected maximum electric field. Fig. 4.20 gives the comparison between the simulated and measured reflection coefficients. The simulation results show the DRA resonates at 23.53GHz compared with 23.5GHz obtained through practical measurement and the reflection

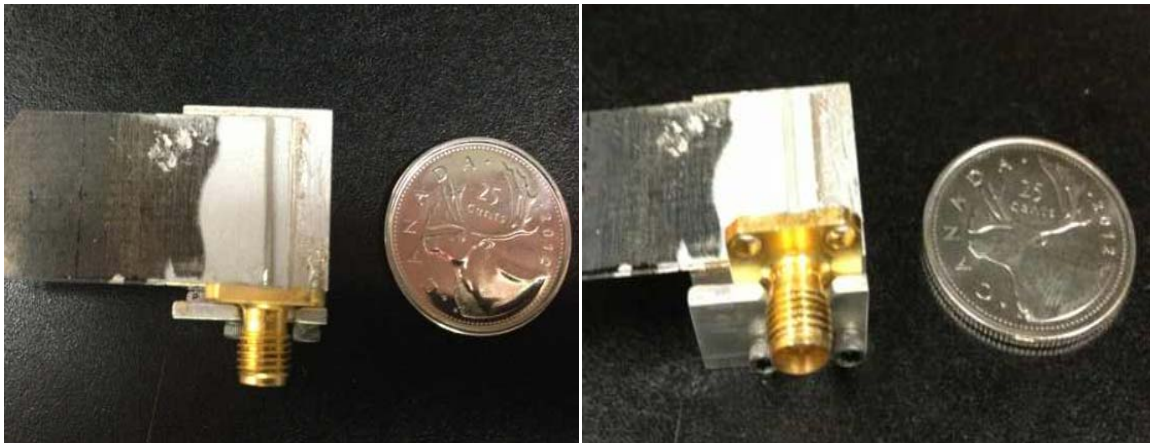

Fig. 4.17 Geometry of side-coupling feeding scheme made by tall microstrip line (Microstrip line courtest of H. Jayatilaka)

Fig. 4.18 1.29mm thick polymer ceramic DRA samples (DRA samples courtesy of M. Tayfeh)

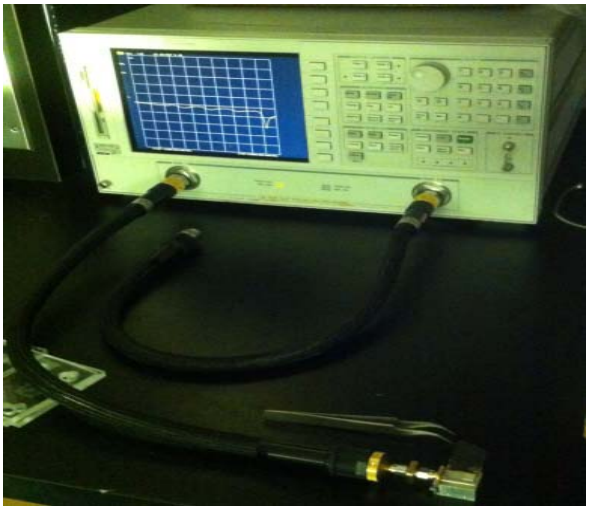

(a) Measurement platform

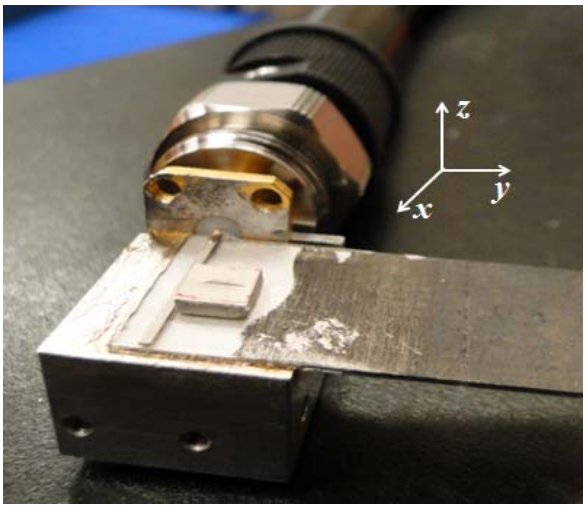

(b) Side coupling feeding structure connecting with the network analyzer

Fig. 4.19 Measurement platform

coefficients for both results are around -40dB. These results show the good agreement between them. The resonance frequencies of the simulated, measured results are 23.53GHz and 23.5GHz respectively. However, field distribution in HFSS simulation show the DRA does not resonate at the dominant mode TE^{x}_{111} as predicted, but the TE^{z}_{111} mode. This is mainly due to the lower thickness of the available feeding line.

Theoretically, TE^{x}_{111} as the dominant mode of rectangular DRA can be excited in this case with using the side coupling feeding scheme; additionally, half-cycle field variation of the electrical field will happen in the *z*-direction, which means the lateral length of the DRA is about half guided wavelength. However, simulation results show the dominant mode cannot be excited due to the thinner feeding conductor trace (in this case 0.29mm thickness is thinner than the side coupling case in the section 4.2.2 in which the thickness of the feeding line is 1.5mm.) producing the inefficient coupling level in this case. As shown in Fig. 4.21 (a)&(b), the vertical magnetic

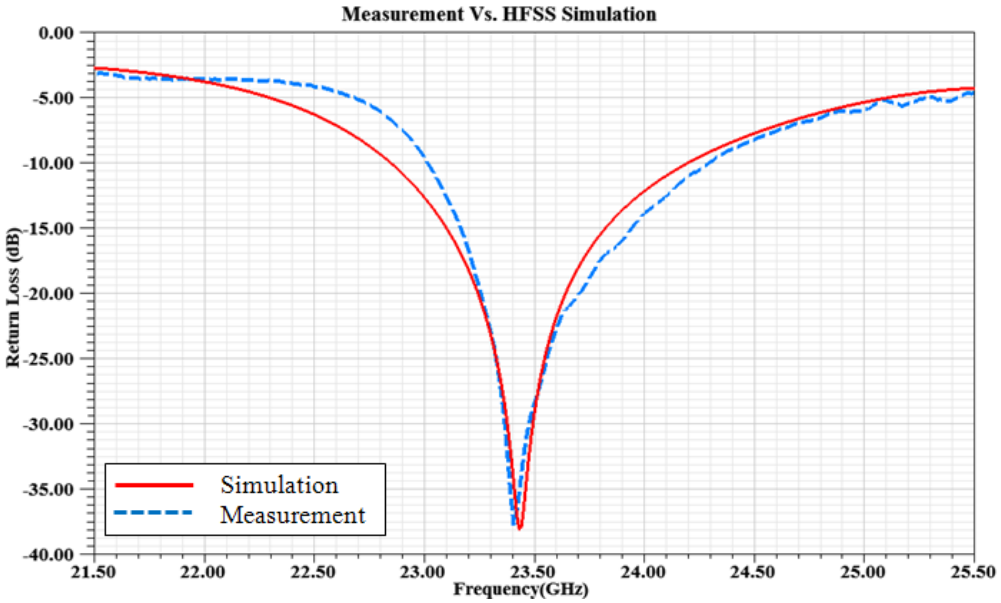

Fig. 4.20 Comparison between simulation and measurement for the DRA with permittivity 10.2

source is excited and passing through from the bottom of DRA to the top surface in the center.

Half-cycle field variations happen in the *x*-direction rather than the *z*-direction. However, since the magnetic field is perpendicular to the ground, passing through from the bottom of DRA to the top surface, the image component of magnetic current on the oppsite side will offset the magnetic source resulting the inefficient radiation mode as shown in Fig. 4.22.

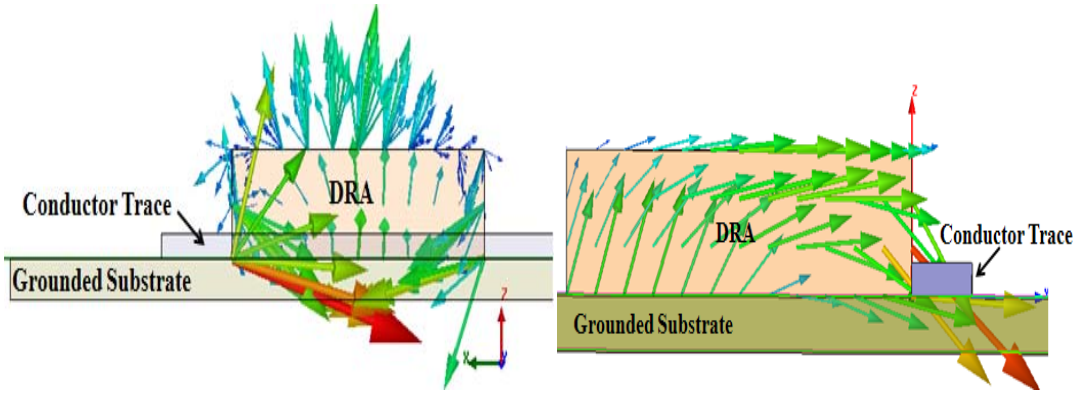

(a) H- fields distribution (b) E-fields distribution

Fig. 4.21 Fields distribution of the DRA which is excited by tall microstrip line

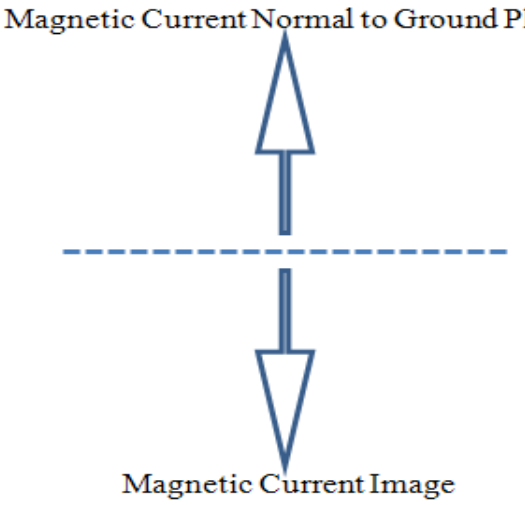

Fig. 4.22 Magnetic source equivalent

In the second case, Fig. 4.23 illustrates the comparison of simulated and measured reflection coefficients for the DRA sample with the permittivity of 8 which is fabricated by XRL technology.

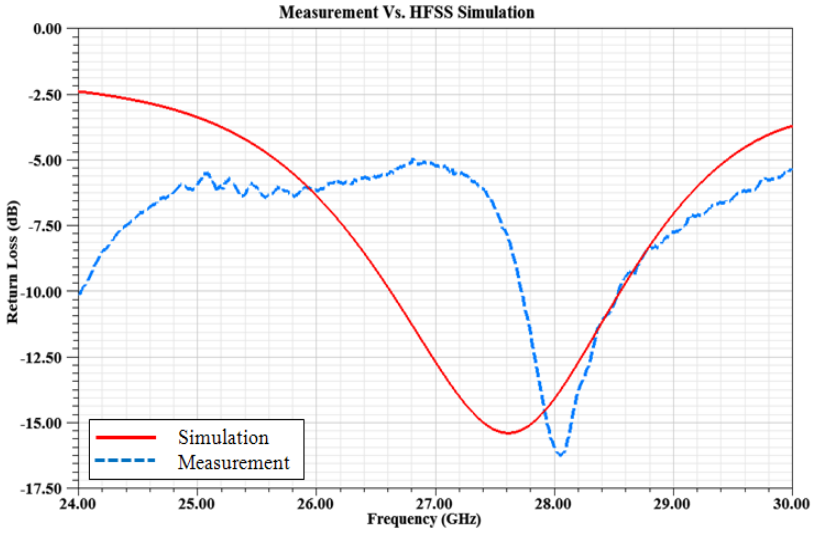

Fig. 4.23 Comparison between the simulated and measurement results for the DRA with permittivity 8

The measured results illustrate that the DRA resonates at 28.2GHz compared to simulated results of 27.58GHz and both of these results have the similar reflection coefficients of -16dB. The difference is likely due to the silicon RTV adhesive which is used to attach the DRA on the substrate to avoid the affect of air gap between the resonator and ground plane. This tiny adhesive layer changes the single DRA into multi-segment DRA model [27] and varies the resonance frequency; furthermore, since the feeding line is not high enough, the low permittivity DRA causes the low coupling resulting in the higher reflection coefficient value.

In order to obtain the high coupling energy and validate the effectiveness of the deep XRL tall transmission line, simulation verification is applied. In this case, the height of feeding line will be increased; meanwhile, the width of feeding line varies to match the E-field distribution inside the resonator to improve the matching condition. For keeping consistency with the test cases, the dimensions and the permittivity of DRA are the same as DRA with permittivity of 10.2 in the test case. Fig. 4.24 presents the configuration of this improved feeding structure in HFSS.

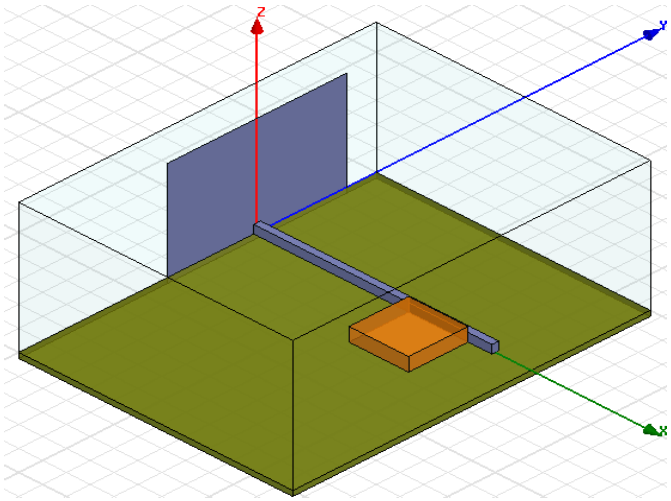

Fig. 4.24 Configuration of the improved side-coupling feeding structure

Reference [36] suggests that it is difficult to achieve the desired reflection coefficient on exciting the DRA with low permittivity value. However, as the thickness of the feeding line is increasing, more coupling energy can be obtained; furthermore, since the dimension of the feeding line is such that the width and the thickness can be varied to improve the matching condition, the simulated resonance frequency of 18GHz under the dominant mode TE^{x}_{111} can be observed. The simulated results show the reflection coefficient at the resonance frequency under the dominant mode is around -7dB, which can be improved easily by using the external matching network in the future work.

Fig. 4.25 shows the simulated E-field distribution of the dominant mode TE^{x}_{111} which circulate around the magnetic fields inside the DRA. Fig. 4.26 (a)&(b) give the excellent simulated radiation pattern under the dominant mode. The short magnetic dipole-like pattern appears in these plots and the gain is about 4dB. Both the reflection coefficient and the radiation pattern in this case can prove that the DRA with low permittivity value can be excited effectively as increasing the thickness of the feeding line, which present the ability and effectiveness of the

XRL fabricated tall transmission on the application of low permittivity DRA feeding schemes.

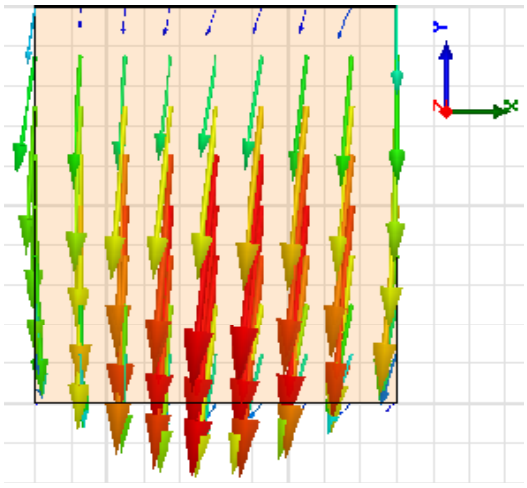

Fig. 4.25 E-field distribution inside of DRA element

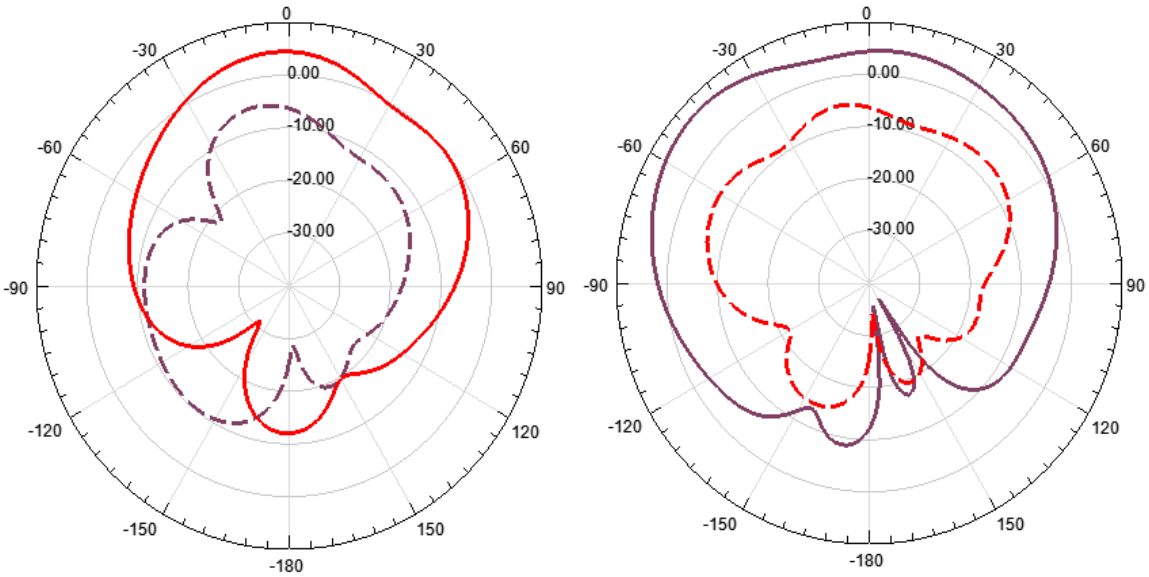

(a) H-plane(ZY) radiation pattern of TE^{x}_{111} mode. ——co-pol, - - -cross-pol.

(b) E-plane(XY) radiation pattern of TE^{x}_{111} mode. ——co-pol, - - -cross

Fig. 4.26 Simulated radiation pattern

4.4 Summary

Three feeding schemes with using deep XRL fabricated tall microstrip line demonstrated the

feasibility of exciting the DRA with low permittivity. Among the three feeding structures, the side coupling feeding is the simplest one. Since the thicker conductor trace can supply more coupling energy, by varying the dimensions of the feeding trace or the position with respect to the feeding line, the DRA with low permittivity can be excited. However, both the simulation and experiment results show this feeding structure is hard to excite the DRA with permittivity value which is lower than 10 due to the low coupling fields. However, the end coupling feeding structure can supply more coupling energy at the open-end tall feeding trace and the DRA even with lower permittivity value can be excited, additionally, since the coupling energy can be modified by varying the guided wavelength of the feeding line, the matching condition can be improved efficiently. The T shape feeding structure is the transformation of the end coupling feeding, since the coupling intensity and the matching condition can be easily changed by modifying the dimension of the open stub line as well as the position with respect to the main line. It is suitable to apply into linear array design. From these investigations above, it can be seen that effectiveness of the tall transmission line feeding structure on exciting the DRA with low permittivity. Since the current tall microstrip line samples are limited, the performance of the experimental structures is not optimal for the test cases due to the inappropriate thickness of the feeding line, especially for the side coupling feeding structure. Two DRA samples with permittivity of 10.2 and 8 respectively were excited and the performance validated by simulation. Since the thickness of the feeding line in both test cases is thinner than the ideal analysis cases before, some other modes rather than the dominant mode are excited out due to the inefficient coupling energy. However, the other approach in simulation shows that the dominant mode of the

low permittivity DRA (ε_r=10.2) can be excited with increasing the thickness of the feeding line; additionally both results of reflection coefficient and radiation performance show the feasibility of the tall feeding line. On the other hand, although it is difficult to achieve the desired performance when exciting the low permittivity DRA with using the side coupling feeding structure, the alternative approaches such as using the external matching network, modifying the DRA with different aspect ratio to match the E-field distribution inside of the resonator [15], [63] or by making the DRA be a multilayer model to increase the coupling energy [27] can be applied in the future work to improve the feeding performance.

However, these issues, such as insufficient coupling energy or less flexibility for design work can be accomplished by using either the direct coupling feeding structure or T shaped feeding structure. Since more field intensity can be anticipated at the open-end circuit, the direct feeding scheme can be applied to excite the DRA with lower permittivity value compared to the side-coupling feeding scheme. The simulation results have already shown their excellent performance in the last section and the permittivity of the DRA can be as low as 5.

Chapter 5
Novel Feeding Mechanism Application in Designing Linear DRA Array

5.1 Antenna Array Introduction

In the modern wireless communication, many applications require high gain or a directional radiation pattern, which cannot be achieved by a single antenna element. Two methods can solve these issues. The first one is to enlarge the dimension of the single antenna element to obtain better directive characteristics. Another way is to assemble a number of radiating elements in an electrical and geometrical configuration without increasing the dimension of the single antenna element. These multi-elements which can produce a directional radiation pattern are referred to as an array antenna. Recently antenna arrays are becoming increasingly important in wireless communications, not only by providing high gain, but also can achieve a steerable beam by using the simple antenna element. Furthermore, the radiation pattern can be changed by exciting the single antenna with different current magnitudes or current phases. This important characteristic can provide us a freedom to achieve the desired radiation pattern without changing the physical dimension. In practical applications, there are many different kinds of geometrical configurations, but the most popular and elementary type is linear array in which the antenna elements arrange along a straight line.

In this work, the novel feeding scheme will be applied to design a 6 element Dolph-Chebyshev

linear DRA array using a proposed new simulation approach. In this chapter, firstly some basic concepts of the linear array will be introduced and then the Dolph-Chebyshev array theory will be discussed. Finally, these concepts are applied to a new simulation approach to demonstrate design in the previous chapters of a 6-element Dolph-Chebyshev DRA array using the novel feeding scheme described.

5.2 Basic Concepts of the Linear Antenna Array

5.2.1 Uniform N Elements Linear Array

The single antenna element can exhibit a specific radiation pattern, however, when several of these radiating elements combine in an array, the overall radiation pattern is changed. This can be described by an array factor (AF). It can determine the whole radiation pattern of the array by combining the radiation pattern of the single antenna element. Furthermore, this factor is a function which only depends on the geometry of the array or the excitation such as the phase or the magnitude. The simplest array pattern: two elements array will be under the investigation. Fig. 5.1(a) shows the geometry of the array. Two infinitesimal dipoles are placed along the *z*-direction. Based on spatial pattern combining, the total E fields radiated by the single element are equal to the sum of the individual field components without considering the coupling between them and is given by [64]:

$$E_{total} = E_1 + E_2 = \hat{a} j\eta \frac{kI_0 l}{4\pi} \{ \frac{e^{-j[kr_1 - \left(\frac{\beta}{2}\right)]}}{r_1} \cos\theta_1 + \frac{e^{-j[kr_2 + \left(\frac{\beta}{2}\right)]}}{r_2} \cos\theta_2 \} \tag{5.1}$$

where the $\hat{a}$ is unit vector, η is intrinsic impedance of the medium, l is the length of the

infinitesimal dipole, k is the propagation constant, the current excitation I_0 is the same and β is the phase difference of the excitation for these two elements. However, if the observation point is far enough away as shown in Fig. 5.1(b) that the distance r_1 is nearly equal to r_2, then the angle θ_1, θ_2 and θ are nearly the same, then the phase differences can be assumed as: $d/2$–cosθ and $d/2$+cosθ, and the E field can be represented as [64]:

$$E_{total} = \hat{a}_\theta j\eta \frac{kI_0 le^{-jkr}}{4\pi r}\cos\theta\left\{2\cos[\frac{1}{2}(kd\cos\theta+\beta)]\right\} \tag{5.2}$$

where the $\hat{a}_\theta$ is the unit vector in θ field direction and the function: $2\cos[\frac{1}{2}(kd\cos\theta+\beta)]$ is known as the AF and the function $\hat{a}_\theta j\eta \frac{kI_0 le^{-jkr}}{4\pi r}\cos\theta$ is the field of the array element. It is apparent that the AF is the function of the relative excitation phase differences, magnitudes of the excitation and the geometry of the array arrangement. Furthermore, the AF can be simplified if the array element has identical amplitudes, phase differences and spacing. From equation (5.2), it is apparent that the total far field pattern of this two element array is equal to the AF multiplied by the field of the single array element. This relationship can be described as[64]:

$$\textit{Total Array Pattern= Array Element Pattern * Array Factor} \tag{5.3}$$

This is an important property of the array and also known as the principle of pattern multiplication [64]. This relationship can also be valid for the linear array with arbitrary number of identical elements. Now the array which consists of N identical antennas is discussed and the configuration is shown in Fig. 5.2. In this array, isotropic radiators are arranged with the same spacing along the z-direction and excited by the same amplitudes. Moreover, each succeeding element has a β progressive phase lead current excitation relative to the

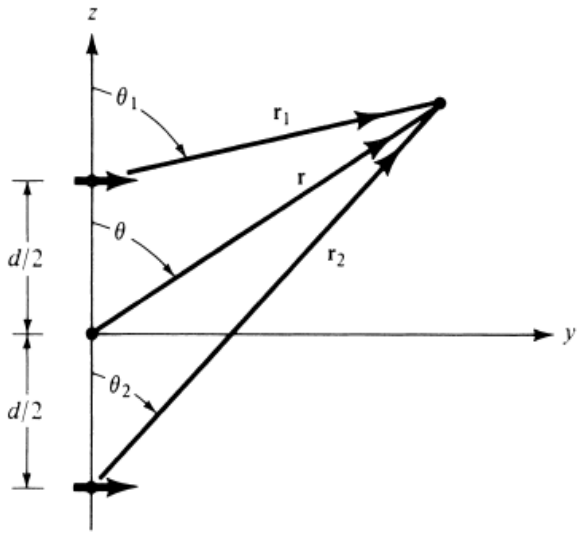

(a) Two infinitesimal dipoles

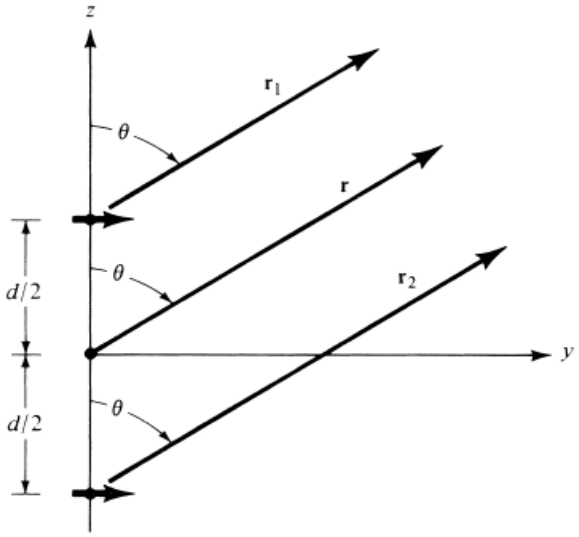

(b) Far field configuration

Fig. 5.1 Geometry of two element antenna array

preceding one [64]. This type of the array is called a uniform N elements linear array. Since the excitation currents to every element in the array have the same amplitude and with a constant

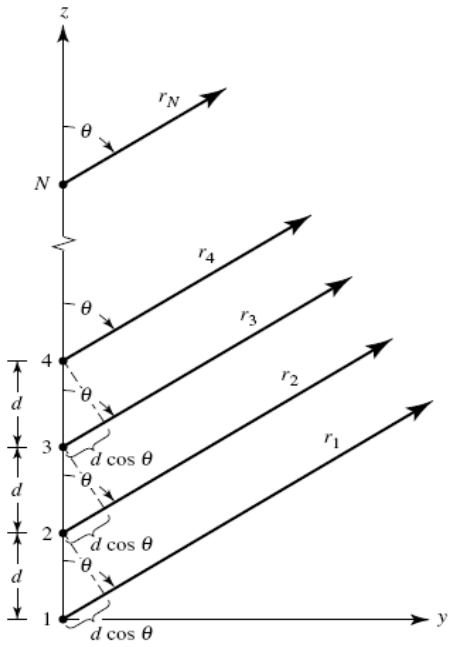

Fig. 5.2 Uniform N elements linear arrays configuration

phase difference β between adjacent elements, then the AF can be obtained as below [64]:

$$AF = 1 + e^{j(kd\cos\theta+\beta)} + e^{j2(kd\cos\theta+\beta)} + \ldots\ldots + e^{jN(kd\cos\theta+\beta)}$$

$$= \sum_{n=1}^{N} e^{j(n-1)\psi} = \frac{\sin(N\frac{\psi}{2})}{\sin(\frac{\psi}{2})} e^{j(N-1)\frac{\psi}{2}} \tag{5.4}$$

Where the $\psi = kd\cos\theta + \beta$ and $0 \le \theta, \beta \le 2\pi,$ N is the number of elements in the array.

If the reference point is located in the center of the array, then the AF in (5.4) can be reduced as [64]:

$$AF = \frac{\sin(N\frac{\psi}{2})}{\sin(\frac{\psi}{2})} \tag{5.5}$$

then the normalized AF to unity is[64]:

$$AF = \frac{1}{N}\left(\frac{\sin(N\frac{\psi}{2})}{\sin(\frac{\psi}{2})}\right) \tag{5.6}$$

Note that angle θ in space has the range from 0 to 2π, while ψ depends on the angle θ which has the wider range than 0 to 2π, leading to a problem of the AF achieving the maximum value more than once during the period.

When $\psi = kd\cos\theta + \beta = \pm 2m\pi$ $(m = 0,1,2,3.....)$, the AF has a maximum value which leads to equation (5.6) having the form: sin*(0)*/0. When ψ=0 the normalized AF in equation (5.6) has a maximum value which is known as the main lobe; however, the maximum values occur many times since the AF is the function of ψ, these different maximum values are called grating lobes [64]. The condition for grating lobes occurring is that the spacing of adjacent elements in the array is equal to or bigger than one wavelength at the operated frequency. Furthermore, a null can be formed when AF equals 0. Under this situation, the angle θ can be simplify in equation (5.7) by setting $\sin(N\psi/2) = 0$ [64].

$$\theta = \cos^{-1}[\frac{\lambda}{2\pi d}(-\beta \pm \frac{2n\pi}{N})] \tag{5.7}$$

where n=1,2,3….. which is the order of the null. n cannot be an integral multiple of N since a maximum will result in the grating lobe. Furthermore, the peak value of AF can be obtained by setting the $\sin(\psi/2) = 0$ as below [64]:

$$\theta = \cos^{-1}[\frac{\lambda}{2\pi d}(-\beta \pm 2m\pi)] \tag{5.8}$$

where m=0, 1, 2, 3…… When m equals 0, the θ function can be simplified as [64]:

$$\theta = \cos^{-1}(\frac{\lambda}{2\pi d}) \tag{5.9}$$

which makes ψ equal to 0 and represents the main lobe of the array. Fig. 5.3 shows an example of the main lobes and the grating lobes. In this plot, the main lobe which contains the direction of maximum radiation occurs in θ=0 direction, while the other maximum radiation which are same

as the main lobe in the different direction are referred to as grating lobes. Between the main lobe and the grating lobes is referred to as minor lobe, the one which is adjacent to the main lobe and the grating lobe is called side lobe which is normally the largest of the minor lobes [64].

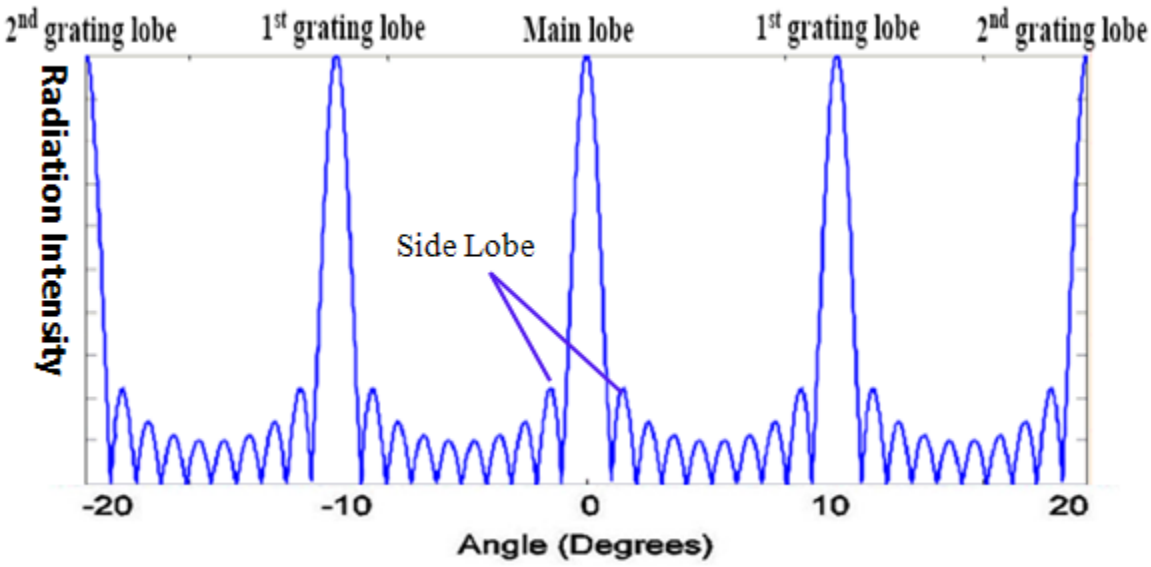

Fig. 5.3 Example of main lobe and grating lobe in the array pattern.

5.2.2 Broadside and End Fire Array

The direction of the radiated main lobe can be changed by changing the array orientation. If the radiated main lobe is perpendicular to the array orientation, it is referred to as the broadside array, while if the main lobe has the same direction as the array orientation, it is known as the end fire array.

For the broadside array, in order to achieve excellent performance, the array element and AF should fulfill the condition that both of them have the maximum radiation at θ=90^{o}. Fig. 5.4 presents this scenario. Furthermore, the maximum AF can be obtained when $\psi = kd\cos\theta + \beta = 0$. In order to satisfy the array phase function, the phase angle β should be

zero, which means every single antenna element in the array must be excited with the same phase and then the normalized AF is equal as below [64]:

$$AF = \frac{1}{N}\left(\frac{\sin(N\frac{kd}{2}\cos\theta)}{\sin(\frac{kd}{2}\cos\theta)}\right) \tag{5.10}$$

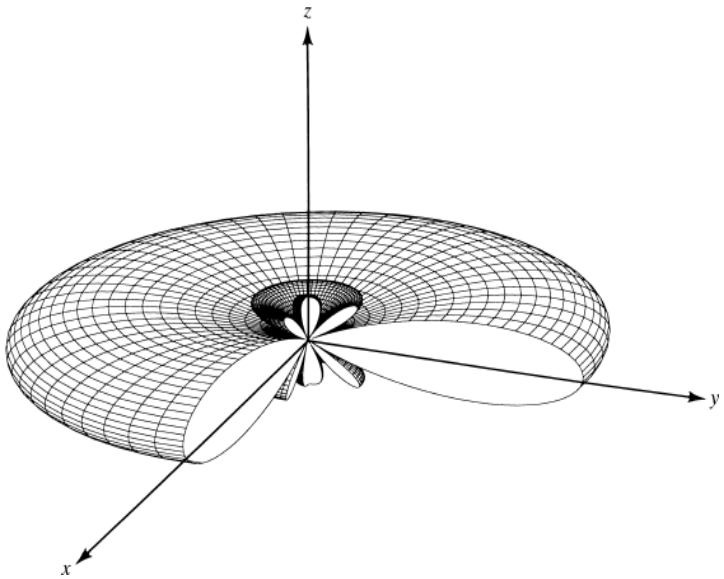

Fig. 5.4 3-D radiation pattern of the broadside array

The following pictures (Fig. 5.5(a)~(d)) show the changes of the AF for a 10 elements linear array under different element spacing: 1/4 guided wavelength λ_g, 1/2 guided wavelength λ_g, 1 guided wavelength λ_g, 1.5 guided wavelength λ_g.

From the simulation results, it can be seen that the width of the main lobe decreases with increasing the element spaces. The grating lobes are introduced when the element space is greater than or equal to 1 λ_g. To avoid the grating lobes, the largest space between the single elements is no more than 1 λ_g. Moreover, since the AF is the function of the number of elements, the main lobe can be sharpened by increasing the number of array elements without changing the

space between the elements. Fig. 5.6 shows the results of a broadside array with fixed element space ($0.5\lambda_g$) for element numbers of 2, 4, 6, and 10.

The second one is the end fire array whose the maximum radiation direction is the same as the array orientation either in 0^o or 180^o (see the Fig. 5.6).

As with the broadside array, the maximum AF occurs when the phase function $\psi = kd\cos\theta + \beta = 0$. When θ=0^o, the first maximum of the AF occurs and the phase angle β is equal to $+kd$, while the second maximum of the AF also occurs when θ=180^o and the phase angle β is $-kd$. The normalized AF of the end fire array is given as [64]:

$$AF = \frac{1}{N}\left(\frac{\sin[N\frac{kd}{2}(\cos\theta \mp 1)]}{\sin[\frac{kd}{2}(\cos\theta \mp 1)]}\right) \tag{5.11}$$

Fig. 5.7 (a)~(d) illustrates how the radiation pattern of the 10 element end fire array changes under the different element spaces: $1/4\lambda_g$, $1/2\lambda_g$, $3/4\lambda_g$, $1\lambda_g$. Unlike the broadside array, the maximum is direct at the θ=0^o when the element space is $1/4\lambda_g$ under the condition that the phase angle is $+kd$. While the maximum will direct at the θ=180^o when the phase angle is $-kd$. Moreover, the end fire array will radiate at both 0^o and 180^o when the element space is $1/2\lambda_g$. The grating lobes are introduced when the element spaces are greater or equal to $1/2\lambda_g$. If the element space is a multiple of the wavelength, such as $d=n\lambda_g$ (n=1, 2, 3….), the end fire array will have the maximum radiation not only at the end fire direction but also at the broadside direction [65].

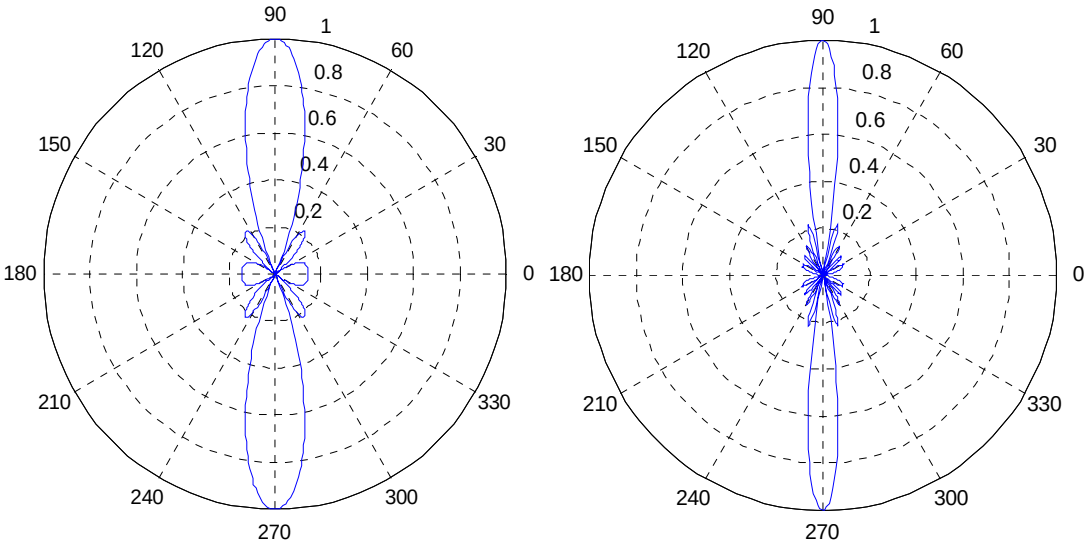

(a): d=1/4λ_g (b):d=1/2λ_g

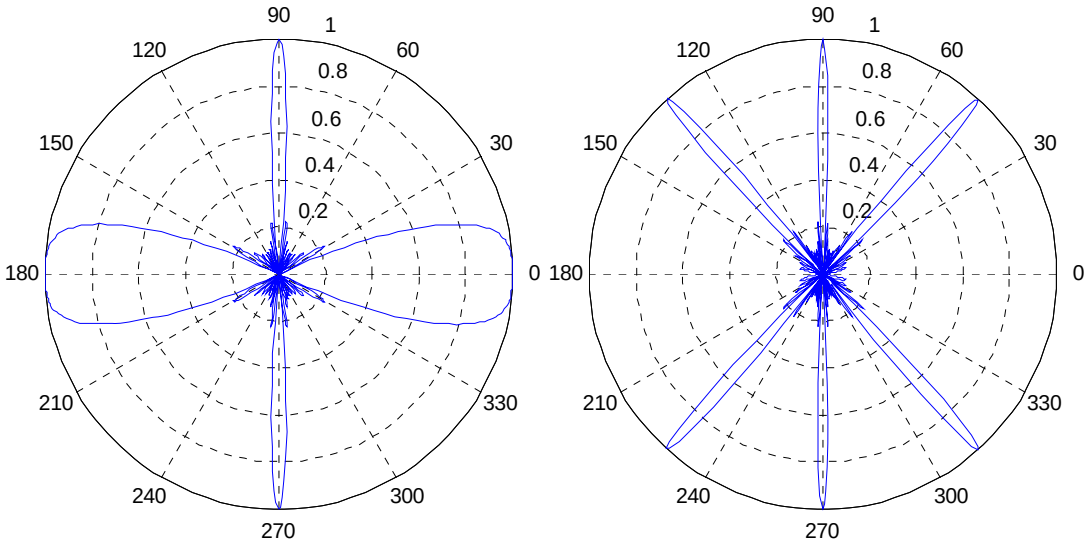

(c): d=1λ_g (d): d=1.5λ_g

Fig. 5.5 AF for broadside array with 10 elements under the different element spaces

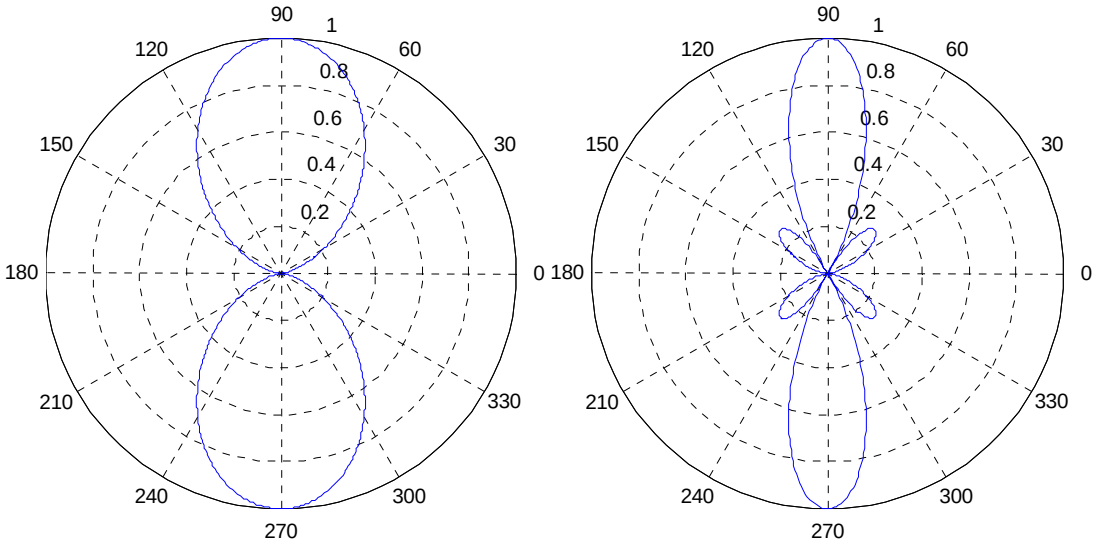

(a) Element number=2 (b) Element number=4

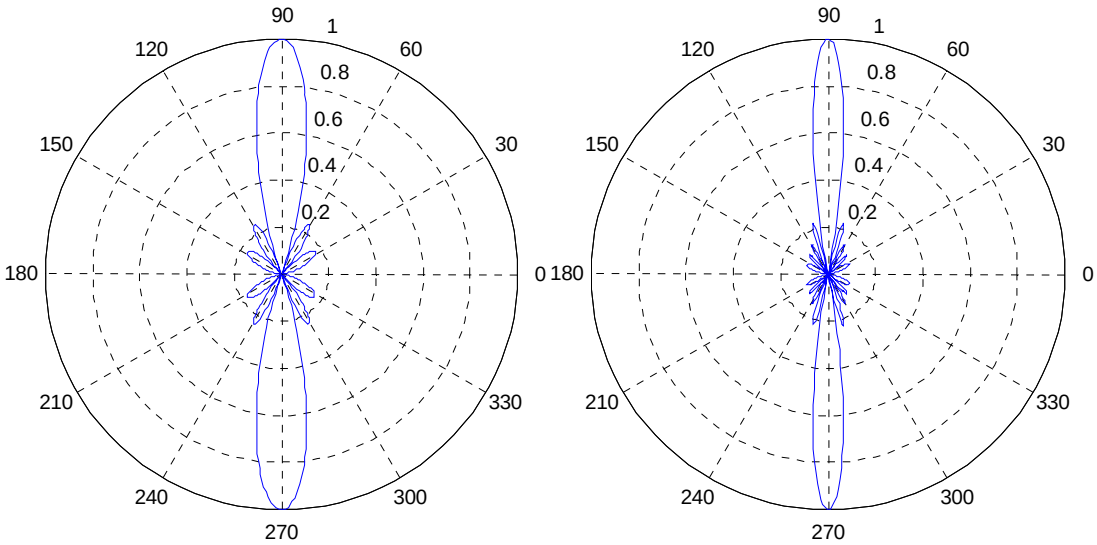

(b) Element number= 6 (d) Element number=10

Fig. 5.6 AF for broadside array with the fixed element space for the element number of 2, 4, 6, 10

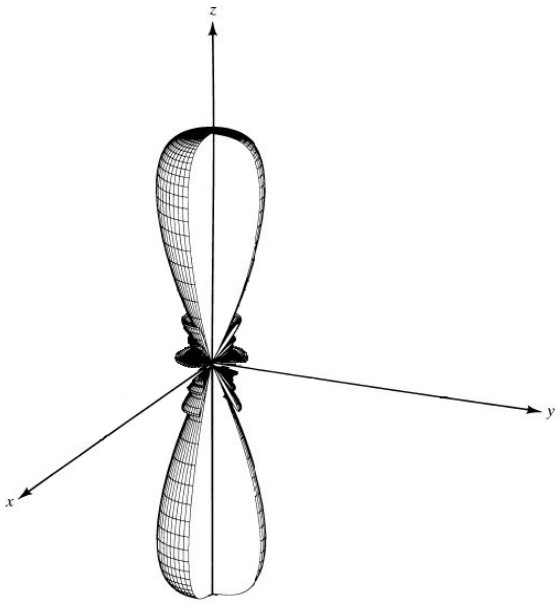

Fig. 5.6 3-D radiation pattern of the end fire array

5.3 Dolph-Chebyshev Array

In practical applications, most communication systems need special radiation characteristics. For example, most applications need the far field radiation pattern to have nulls in a certain direction; while other systems require the pattern to have a narrow beam and low side lobes. In order to satisfy system requirements, a new approach must use systematic combination methods to come up with the new geometry of the array or the special excitation distribution. It has been found that the side lobes can be reduced by using the special excitation distribution which is based on some approximate analytical model. Such a design method is known as synthesis [65]. There are several synthesis methods which are applied to different situations, producing the different radiation pattern, such as continuous sources, Fourier transform method, Woodward-Lawson method, Dolph-Chebyshev method, Taylor line source and so forth [64]. In this work, the

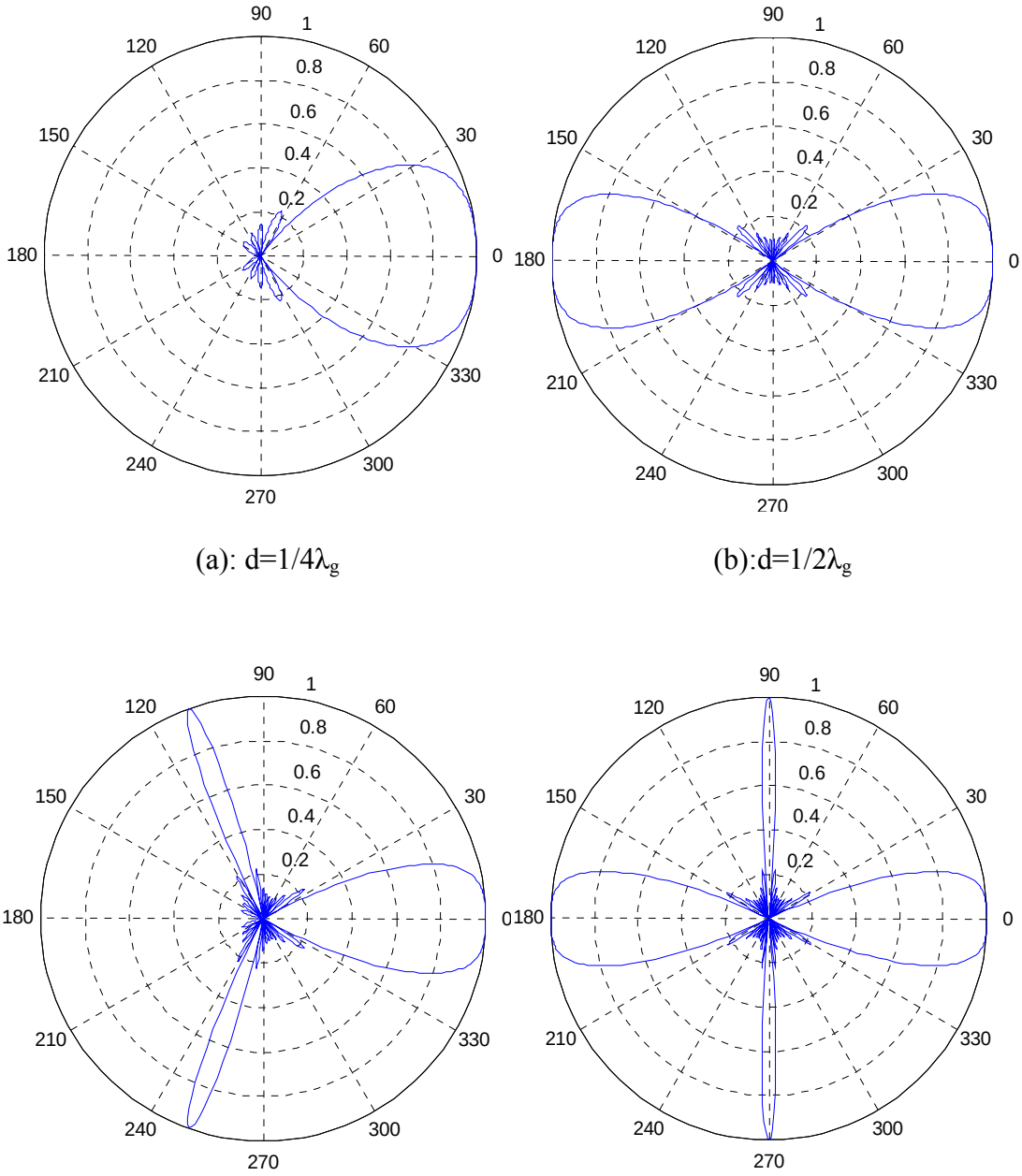

(a): d=1/4λ_g (b):d=1/2λ_g

(c): d=3/4λ_g (d): d=1λ_g

Fig. 5.7 AF for end fire array with 10 elements under the different element spaces

Dolph-Chebyshev method is studied and applied to design the linear DRA array.

Dolph-Chebyshev method was firstly introduced by C. L. Dolph in [66], and can produce the sharp main beam and low side lobes widely used in point-to-point communication and direction finding systems. The first step of this method will apply the Chebyshev polynomials representing

the radiation pattern approximately. The Chebyshev polynomials are defined as:

$$T_n(x) = \begin{cases} (-1)^n \cosh(n \cosh^{-1} |x|), & x < -1 \\ \cos(n \cos^{-1} x), & -1 < x < 1 \\ \cosh(n \cosh^{-1} x), & x > 1 \end{cases} \tag{5.12}$$

By letting $\delta = \cos^{-1} x$ and expanding the $\cos(m\delta)$ in powers of $\cos\delta$ [65], some lower order polynomials can be written as:

$$T_0(x) = 1$$

$$T_1(x) = x$$

$$T_2(x) = 2x^2 - 1$$

$$T_3(x) = 4x^3 - 3x$$

$$T_4(x) = 8x^4 - 8x^2 + 1 \tag{5.13}$$

The higher order polynomials can be obtained by using the recursive formula as below[65]:

$$T_{n+1}(x) = 2xT_n(x) - T_{n-1}(x) \tag{5.14}$$

From equation (5.12), some important properties of the Chebyshev polynomials can be found. The even orders of Chebyshev polynomials are even functions and the odd orders of Chebyshev polynomials are odd functions. The magnitude of polynomials fluctuates between -1 and 1 within the range of $-1 \leq x \leq 1$. Moreover, whatever the order of the polynomial is, $T_n(1)$ is always equal to 1 and all zeros of these polynomials lie within the range $-1 \leq x \leq 1$.

Fig. 5.8 plots the Chebyshev polynomials with n from 1 to 4. Through utilizing these properties of the Chebyshev polynomials, some special radiation pattern of the array, such as side lobes designed at some specific level, can be represented by connecting the Chebyshev polynomials and the array factor. The second step is analyzing the antenna pattern to match with the analytical

model, and making a new physical antenna model have the anticipated performance. An array of antennas along the *z*-direction and excited with the same current phase but different current amplitudes, but symmetric about the origin point, is referred to as a uniform spacing nonuniform amplitude linear array [65]. If the number of antenna elements is even, then the AF can be written as [66]:

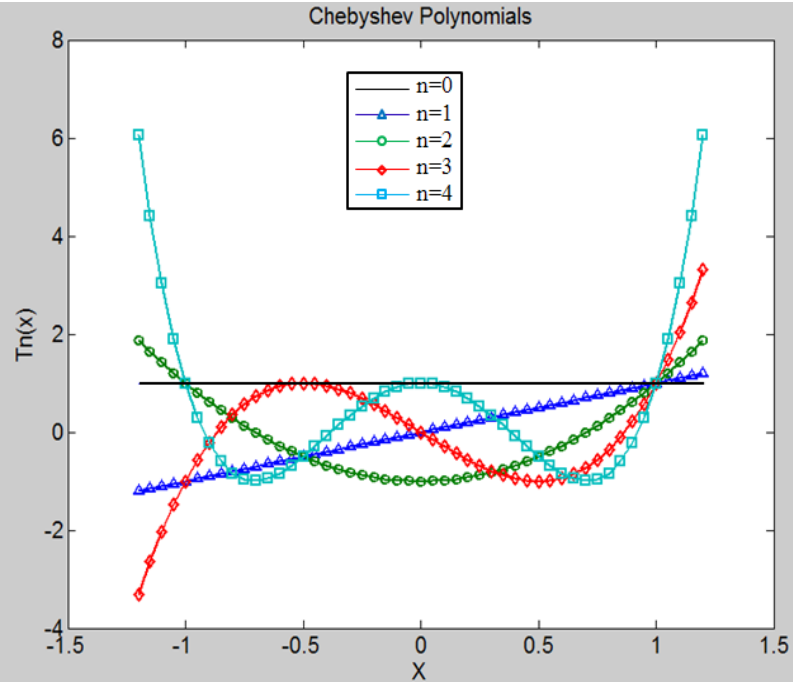

Fig. 5.8 Chebyshev polynomials $T_n(x)$ with n=0~4

$$(AF)_{even=2M} = \sum_{n=1}^{M} a_n \cos[\frac{(2n-1)}{2}\cos\theta] \tag{5.15}$$

If the number of the antenna elements is odd, AF can be written as [66]:

$$(AF)_{odd=2M+1} = \sum_{n=1}^{M+1} a_n \cos[(n-1)kd\cos\theta] \tag{5.16}$$

In both of the equations 5.15 and 5.16, each cosine term in the array factor can be expanded by

using the expansion in term of powers of cos*(u)*. Remember in these design procedures, the order *n* of the Chebyshev polynomial should be one less than the total number of elements in the array. The value of the side lobe peak to the value of the main beam peak in the pattern is known as the side lobe level (SLL). It can be presented as [65]:

$$SLL = 20\log\left|\frac{\text{value of the highest side lobe value}}{\text{value of the main beam}}\right| = -20\log R \tag{5.17}$$

where R is referred to as the ripple which is the ratio of the value of the highest side lobe value to the main beam value. In the design of Dolph-Chebyshev array, R can be driven from the Chebyshev polynomials and presented as [65]:

$$\begin{aligned} R &= T_{p-1}(x_0) = \cosh[(P-1)\cosh^{-1} x_0] \\ \text{where: } x_0 &= \cosh[\frac{\cosh^{-1} R}{P-1}] \end{aligned} \tag{5.18}$$

The final step is substituting $\cos(u) = x / x_0$ into the equations of AF (5.15) and (5.16), and normalizing the side lobes in AF to a peak of unity. The array coefficients can be obtained by equating the normalized AF to the Chebyshev polynomials $T_{n-1}(x)$, then the AF can be driven out. To summarize this design procedure, the first step is choosing the appropriate AF basing on the number of the array elements. Secondly, expanding the AF by replacing each cos*(mu)* term basing on the expansion of cos*(u)*. In addition, x_0 can be computed from the (5.18) by defining the required main lobe to the side lobe ratio *R*. Furthermore, the terms cos*(u)* in selected AF are substituted by x/x_0 . Finally, the coefficients of the AF can be obtained by comparing the transformation AF with the corresponding Chebyshev polynomials.

5.4 New feeding Scheme on Nonuniform Linear Dolph-Chebyshev DRA Array Design

5.4.1 The Analysis of Dolph-Chebyshev Array Design

The synthesis method of Dolph-Chebyshev array design can obtain a group of symmetrical current distributions. With these different current excitations, the side lobes of the linear array can be reduced considerably, while the main beam is enhanced. However, since only the coefficient values can be computed from the Dolph-Chebyshev method, it is necessary to transfer these coefficients into some common design parameters, such as impedances or reflect coefficients, to realize the practical design.

It is known that for a linear series feeding array, each antenna in the array can be seen as a resonator lying along a straight line with the same spacing. In chapter 2, a novel T shape DRA feeding scheme was introduced and now it will be applied to design the Dolph-Chebyshev array. Similar to the series feeding of the microstrip array, all antennas will be placed along the short or open end terminated feeding line, only leaving one input port to lead the signals flowing into every array element. Such an array configuration is known as a resonant array or travelling wave array [67]. The equivalent circuit of the resonant array is shown in Fig. 5.9. The conductance g_n (n=1,2…n) represents the radiating elements, spaced periodically along the feed line. Since the short or the open termination is quarter or a half guided-wavelength beyond the last element in the array, the termination always appears as an open circuit at the last element.

The analysis approach is similar to the slotted waveguide array in [68]. Since the current

amplitudes distribution can be computed from the Dolph-Chebyshev synthesis method, the values of the conductance g can be represented by the function of the desired amplitude distribution and are given as [69]:

$$g_i = \frac{A_i^2}{\sum_{i=1}^{N} A_i^2} \tag{5.19}$$

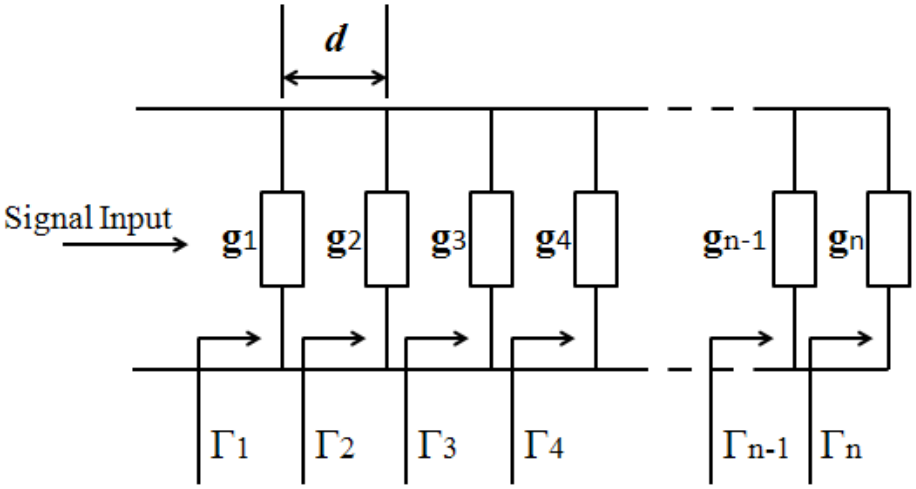

Fig. 5.9 Equivalent circuit of the linear resonant array

where A_i is the current amplitude coefficient for the ith array element whose value can be determined by using the Dolph-Chebyshev synthesis method. N is the total number of the element in the array. Since the space between each array element is either half or one guided wavelength, the cumulative reflection coefficient at every element can be obtained by[69]:

$$\Gamma_i = \frac{1 - \sum_{j=1}^{i} g_i}{1 + \sum_{j=1}^{i} g_i} \tag{5.20}$$

Through these two equations, the relationship between the current amplitude distribution of the

Dolph-Chebyshev array and the conductance distribution, reflection coefficient as well as S parameters can be built up. A 6 DRA elements linear Dolph-Chebyshev array is described as an example to acquire the corresponding current amplitude distribution, conductance distribution, reflection coefficient as well as the corresponding S-parameters.

Based on the design procedures in the last section, the specification of the target array is a 6 elements linear Dolph-Chebyshev array. The SLL in dB format is -20dB and the spacing between the array elements is one wavelength apart. The symmetrical array coefficients distribution which is normalized to the lowest side lobe coefficient can be obtained from the design procedures described in the last section and are shown in Table 5.1:

Table 5.1 20 dB 6 element Dolph-Chebyshev coefficient distribution

a_1	a_2	a_3	a_3	a_2	a_1
1	1.437	1.850	1.850	1.437	1

Then utilizing equations (5.19) and (5.20), the complete design table can be shown in Table 5.2. From this table, it can be seen that the sum of the symmetrical conductance distribution values is equal to 1, indicating the ideal input admittance. In addition, as the number of array elements increases, the reflection coefficient decreases toward the ideal value of 0 ($S_{11}\rightarrow -\infty$), indicating a good matching condition.

Table 5.2 Design chart for the 20 dB Dolph-Chebyshev linear array

DRA Element	a_i	g_i	Γ_i	S_{11} ***in dB***
1	1	0.077	0.857	-1.342
2	1.437	0.159	0.618	-4.183
3	1.850	0.264	0.333	-9.542
4	1.850	0.264	0.134	-17.462
5	1.437	0.159	0.040	-27.940
6	1	0.077	0.000	-∞

5.4.2 Advantages to Design Dolph Chebyshev Linear DRA Arrays by Using Tall Feed Structure

The design approach for the microstrip line series feeding DRA linear array is similar to the linear array of capacitive coupled microstrip patches in [67]. A. Petosa in [69] illustrates the traditional way to design the linear DRA array. In his paper, he sets the S_{11} parameter which can be obtained from the reflection coefficient as the design guide and achieves the target experimentally. First of all, the open-end unloaded microstrip line was connected to the network analyzer and the input coefficient measured; then one DRA element was placed aside the microstrip line at a time, through tuning the distance between the DRA and the line until obtaining the corresponding cumulative reflection coefficient. This procedure was repeated for several times until all the antenna elements were added along the microstrip line. However, if the number of the array element is huge, no matter using the experimental way or the simulation tools, this traditional way will become inefficient and time consuming, because the capacitive coupling which refers to the distance between the DRA and the microstrip line becomes very hard to control. However, since the coupling can be controlled by adjusting the dimensions of the

open stub line, the T shape novel feeding scheme can overcome these issues. Furthermore, the special configuration of T shape feeding scheme offers a novel simulation method to linear array design.

From the equation (5.20), since the impedance is the inverse of the conductance, the reflection coefficient can be represented by the impedance format. This new simulation approach transfers the conductance distribution into the impedance distribution and sets it as the design guide. Unlike the tradition way, this new method does not need to add the DRA element aside the microstrip line one by one until the acceptable performance can be achieved, because the coupling can be varied by adjusting the dimension of the open stub feeding line rather than tuning the spacing between the DRA and the feeding line one by one; additionally, the T shape feeding structure has more design degree (the width, length and height of open stub line) than the traditional side coupling feeding structure (only the spacing between the DRA and the feeding line), so it is more effective and efficiency. Since the real impedance can be achieved when the array elements resonate at the desired frequency, also the array elements are one wavelength apart and the impedance of every DRA element in the array can be obtained independently, there are only half of the impedances required due to the symmetrical distribution if the array number is even (if the array number is odd, the required impedance values are one more than the even number array). When the number of the array element is increasing, this method becomes more efficient, since only half of the array element is simulated. After obtaining the corresponding impedances, the single array element will be combined together by the designed guided wavelength apart and the desired performance can be easily achieved by few times simulation.

Comparing with the traditional design way, this new simulation method saves much resource and avoids the heavy work if the number of the array elements is huge, making it more effective and timesaving.

In the chapter 4, since we know the imaginary part of the input impedance will be cancelled out in the resonating condition, obtaining the real impedance, during the simulation it is easy to verify if the DRA element operates at the desired frequency through checking the input impedance in HFSS.

Firstly, the conductance distribution is transferred into a corresponding impedance distribution in Table 5.3 based on the conductance distribution for previous Dolph-Chebyshev array example. The equivalent circuit of this model is shown in Fig. 5.10.

Table 5.3 Impedance distribution of the 20 dB Dolph-Chebyshev array

R1	***R2***	***R3***	***R4***	***R5***	***R6***
648.5Ω	314Ω	189.5Ω	189.5Ω	314Ω	648.5Ω

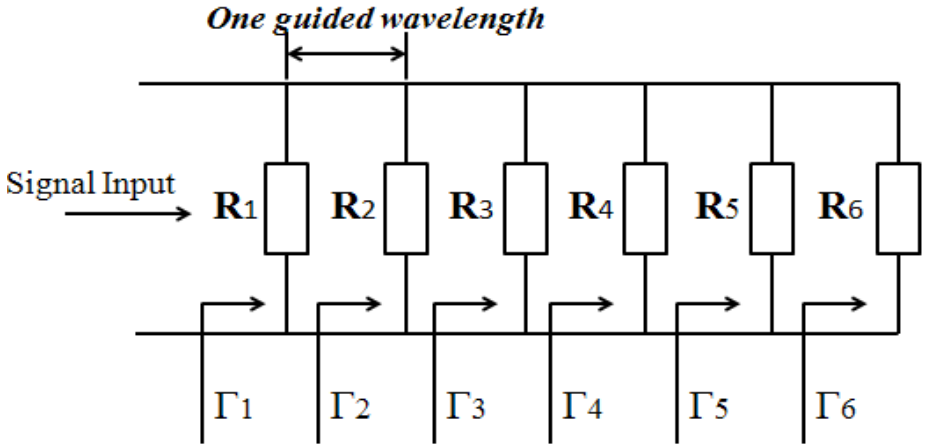

Fig. 5.10 The equivalent circuit of the new approach for Dolph-Chebyshev array design

Then the single DRA model which is excited by using the T shape novel feeding scheme in

HFSS software and its equivalent circuit are shown in Fig. 5.11 (a)&(b). The DRA is assumed to be a material with permittivity of 5 and the material of the tall feeding line is assumed to be nickel on the 1mm thickness quartz glass substrate. The DRA is placed one guided wavelength away from the open end point. Through adjusting the width of the open stub line, the corresponding impedance can be achieved.

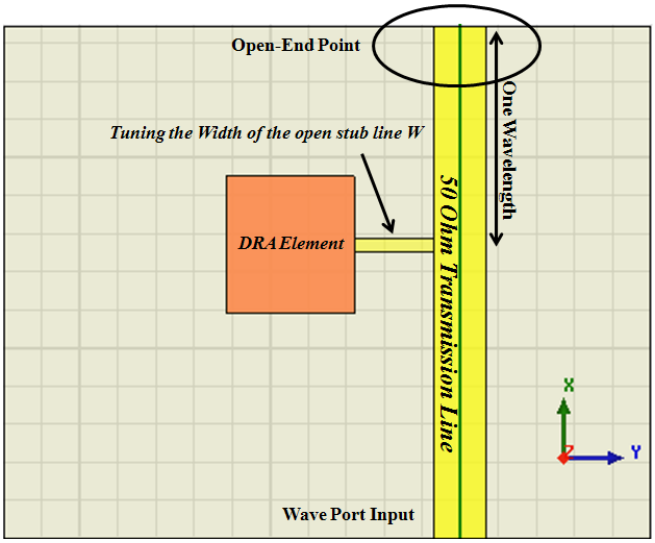

(a) The single element model of the array in HFSS

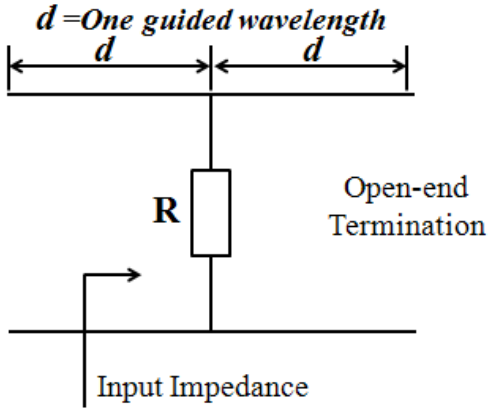

(b) The equivalent circuit

Fig. 5.11 Single feeding model and its equivalent circuit

During this process, in order to keep the uniform array structure, the height of the open stub line as well as the main microstrip line is fixed at 0.2mm. The array is operating at 24.75 GHz. Fig.

5.12 (a)~(f) give the simulation results of the impedance for the first three elements in the array. From these simulation results, it can be seen that the imaginary parts of these three DRA elements are nearly equal to 0, indicating that the DRA elements resonate at 24.75 GHz.

The comparisons for the simulation results and the ideal theory values of the impedance distribution are shown in Table 5.4. From the comparison, only R_1 has the big difference with the theory value. This is because of the inappropriate coupling at the open end. If the line is too thin, not only can it not excite the DRA but is also difficult to fabricate, so it is helped to maintain a reasonable range. Furthermore, there is a compromise between the R_1, R_2 and R_3 values. Since the different impedance values require different coupling levels, the dimensions of the open stub line, such as the width or the length, vary to achieve different impedance values. In addition to the width of the open stub line, its length is also a critical parameter which can affect the coupling.

From the impedance distribution in Table 5.3, it can be seen that this distribution is symmetrical; additionally, the first and the last elements in this table have the highest impedance value, while the elements in the center part such as R_3 and R_4 require the minimum impedance value. This tendency requires the dimensions of the open stub feeding line for each DRA element to be a tradeoff. In order to achieve the high impedance, the width should be as thin as enough and the distance between the main line and the DRA should be far enough, indicating that the coupling energy is very weak at the end of the open stub line. However, if the open stub line is too long, in order to keep the structure uniform with the rest of other DRA elements and obtain the appropriate coupling, it is hard to achieve appropriate impedance for the DRA with low

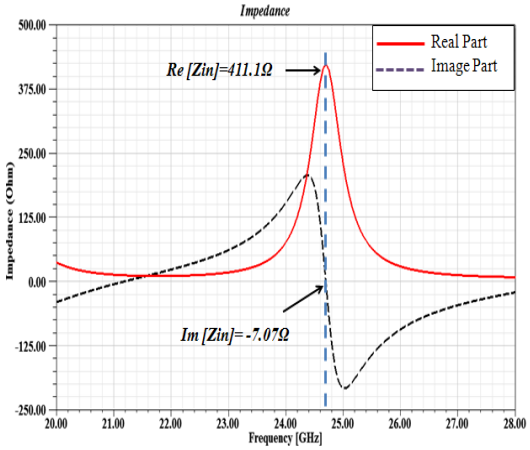
Impedance
Real Part
Image Part
Re [Zin]=411.1Ω
Im [Zin]= -7.07Ω
Impedance (Ohm)
Frequency [GHz]

(a)

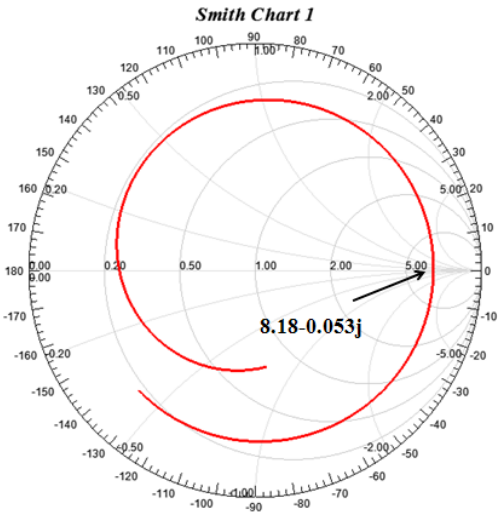
Smith Chart 1
8.18-0.053j

(b)

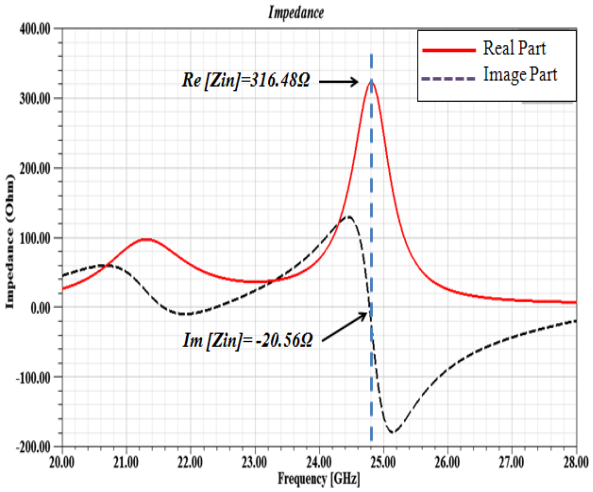
Impedance
Real Part
Image Part
Re [Zin]=316.48Ω
Im [Zin]= -20.56Ω
Impedance (Ohm)
Frequency [GHz]

(c)

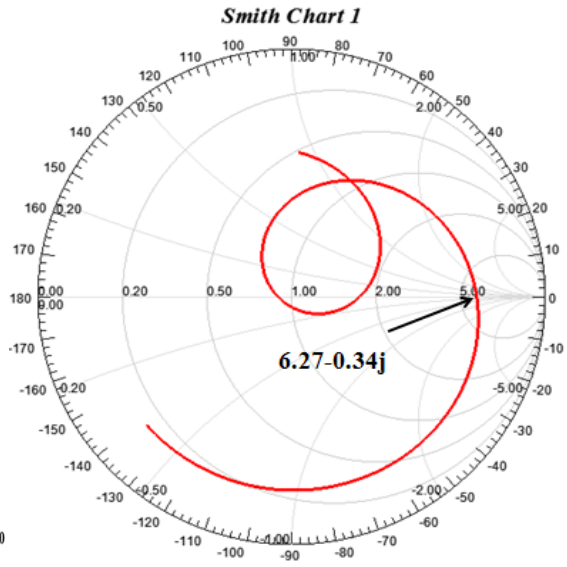
Smith Chart 1
6.27-0.34j

(d)

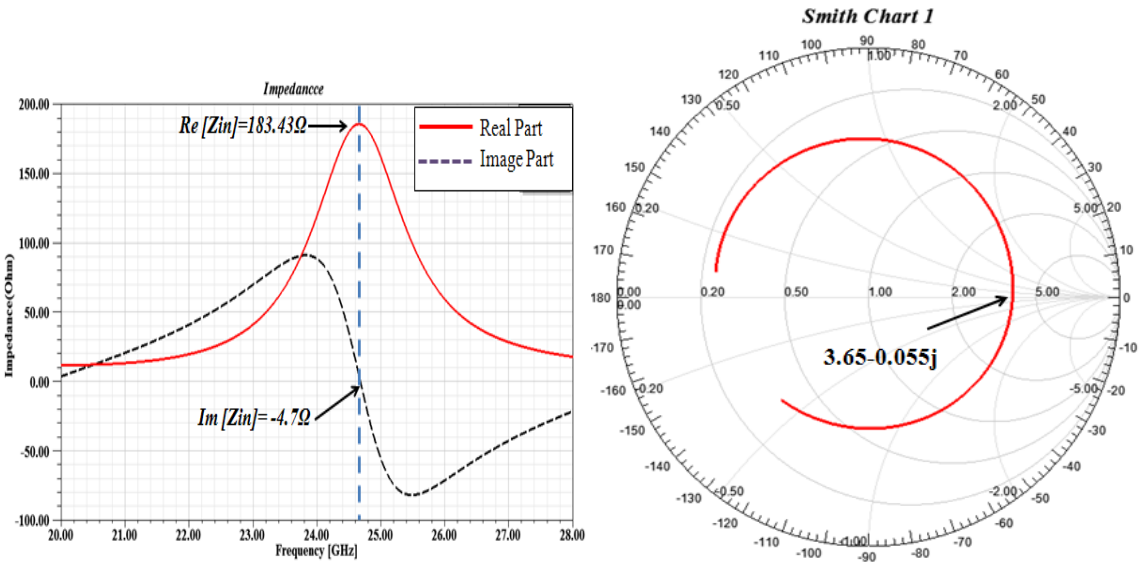

(e) (f)

Fig. 5.12 Simulation results of the single element in the array.

(a), (c), (e): Input impedance of the R_1, R_2, R_3 respectively.

(b), (d), (f): Smith Chart for normalized R_1, R_2, R_3 respectively.

Table 5.4 Comparison of simulation results with theoretical values

DRA Element	***Z*$_{in}$ (Theory)**	***Real Part of Z*$_{in}$ (HFSS)**	**Imaginary part *Z*$_{in}$(HFSS)**	**Phase(HFSS)**
R1	648.05Ω	411.1Ω	-7.07Ω	-2.19
R2	314Ω	316.48Ω	-20.56Ω	-1.52
R3	189.5Ω	183.43Ω	-4.7Ω	-2.35

impedance value. Because the open stub line cannot produce the high level coupling at the open end point due to the inappropriate electrical length. Because of this reason, considering decreasing the low side lobe level during this design work, the impedances of the second and third elements may be made suboptimal on the premise of increasing the impedance of the first element as high as possible.

After obtaining the corresponding impedance model in HFSS, the array can be built up. The next

work is fine tuning the distance of the each adjacent DRA until both good RF performance and radiation performance can be achieved.

In this case, more fields distribute outside the resonator due to the low permittivity of the DRA element. When connecting all the elements together, these fields result in higher mutual coupling; besides the linear array behaves like a leaky wave structure, especially when the number of the elements is increasing. So the total length of the array should be smaller than the computation in theory. Fig. 5.13 shows the geometry of the array in HFSS software after the fine tuning.

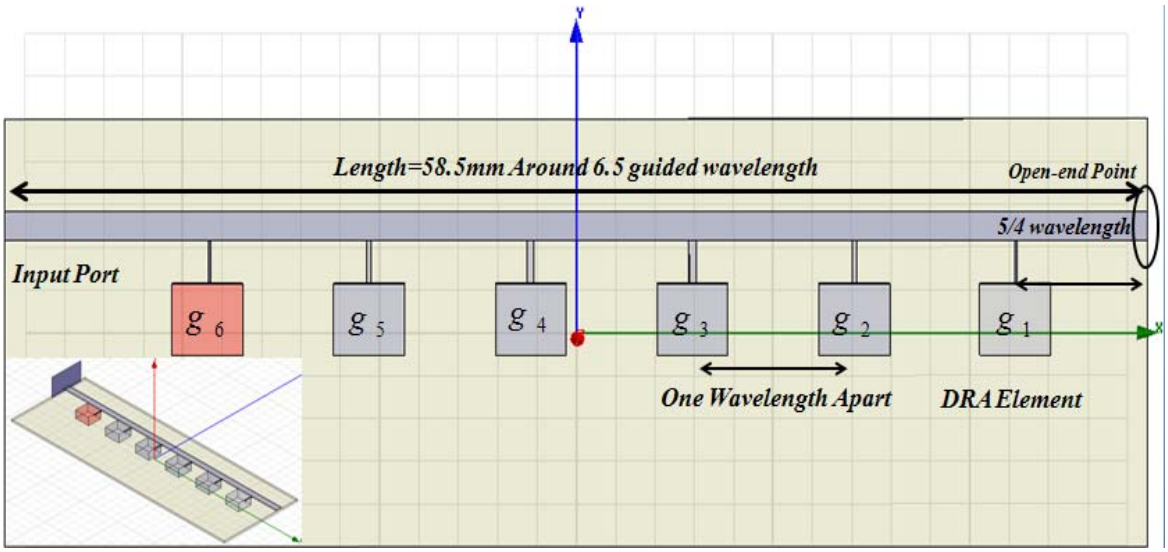

Fig. 5.13 Geometry of the Dolph-Chebyshev array.

In the configuration of the array, it can be seen that the dimensions of the open stub line distribute symmetrically. The widths of the open stub line for the middle two elements (element 3 and 4) are wider than the rest of the array elements due to the high impedance. This is because both of the center elements need more coupling, additionally the current amplitude of the Dolph-Chebyshev array is tapered more toward to the edges of the array, enhancing the main beam while decreasing the side lobes. Fig. 5.14 (a)~(c) gives the radiation performance as well

as the comparison with theoretical calculation. The simulated gain value of this array is around 9dB and the side lobe level is about 15dB which is 5dB higher than the design specification of 20dB. This is because of the inappropriate impedance distribution for the DRA elements R_2 and R_5 as well as the field distribution outside of the DRA element due to the low permittivity. The radiation pattern is approximately symmetrical while the main beam is tilted. This is because the current phases between the array elements are not perfectly uniform; besides, as the number of the elements is increasing, the impacts of the mutual couplings due to the low permittivity value of the DRA elements become more serious, resulting in erratic guided wavelength happening in the middle part of the main feeding microstrip line. Furthermore, since the phases between the array elements are not uniform, after connecting them together, the current amplitude can also be affected. This phenomenon can be observed in the simulated E-fields magnitudes distribution in Fig. 5.15. In this plot, it is can be observed that the non-uniform phase distribution affects the magnitude of the feeding line E-field from the third element and shifts the DRA elements away from the optimal position. These different field magnitudes influence the symmetry of the whole current amplitude distribution. The 3-D radiation pattern shown in Fig. 5.16 can show the radiation pattern which is impacted by the unsymmetrical current magnitude distribution.

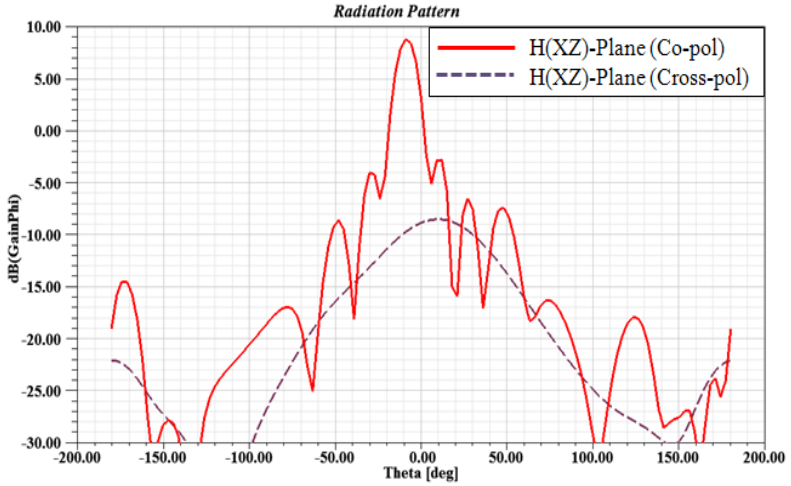

(a) Radiation pattern of the H-plane

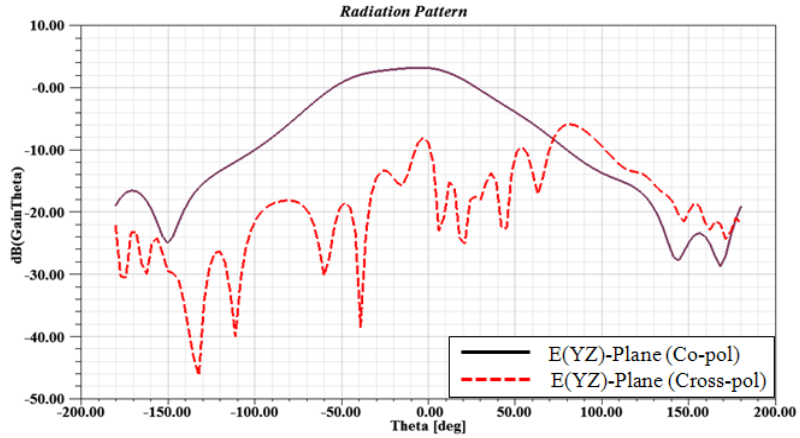

(b) Radiation pattern of the E-plane

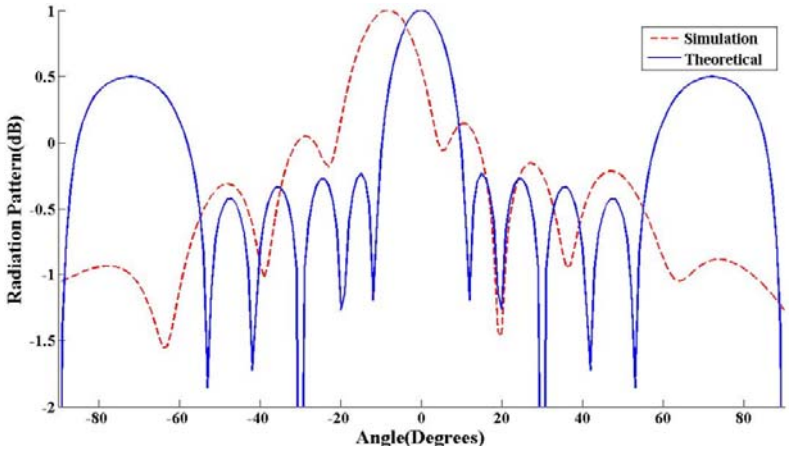

(c) Comparison of the normalized results between the simulation and the theoretical calculation

Fig. 5.14 Radiation pattern of the Dolph-Chebyshev array.

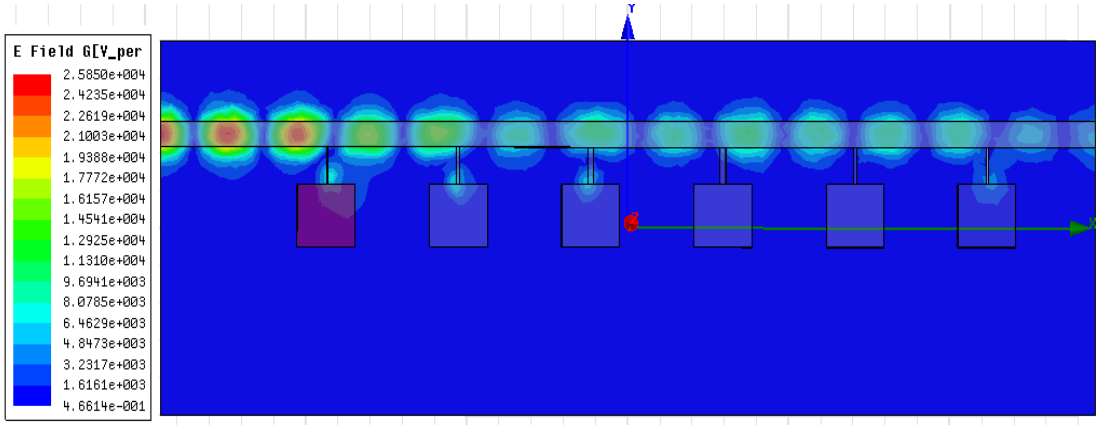

Fig. 5.15 E-field distribution of the feeding structure

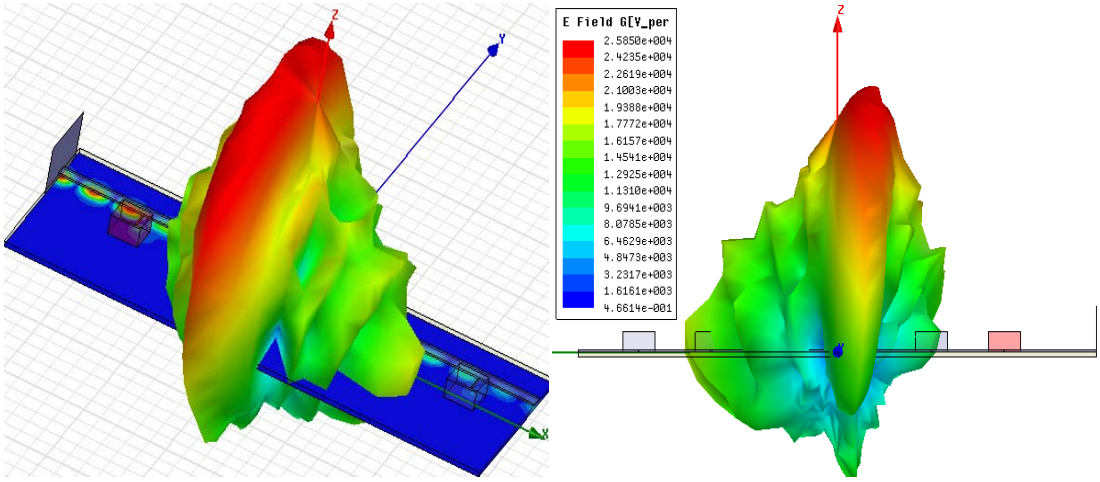

Fig. 5.16 3D radiation pattern of the Dolph-Chebyshev array

In addition, the theoretical radiation pattern in Fig. 5.14 (c) has two grating lobes; this is because the spacing between the array elements is one wavelength. For the broadside array, if the spacing between the array elements is higher or equal to the one wavelength, the grating lobes will be introduced. While for the simulation result, the grating lobes do not exist even if the array was designed under the one wavelength spacing. This is also because of the mutual coupling between the array elements which shortens the guided wavelength and disturbs the current phase and amplitude distribution.

Fig. 5.17 gives the return loss (S_{11} in dB) of the array. Since the lower permittivity DRAs are

applied into this design work, the 10dB bandwidth is about 13% which is much higher than the other linear DRA array works such as in [69]. The lowest point within the 10dB bandwidth is -15dB.

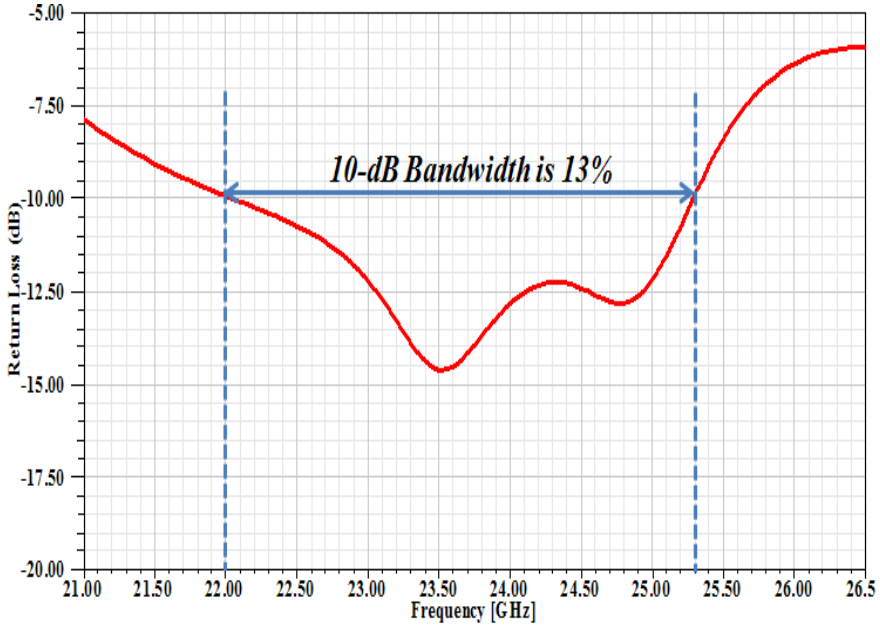

Fig. 5.17 Return loss of tall T shape Dolph-Chebyshev array

5.5 Conclusions

In this chapter, the novel T shape microstrip feeding structure was applied to the Dolph-Chebyshev array design work. This new feeding scheme has some special characteristics compared with the traditional microstrip feeding structure. For example, it can excite the DRA with the lower permittivity value effectively, and the coupling level can be adjusted by tuning the dimension of the open stub line. A new simulation approach sets the impedances distribution as the design guide, since the impedance for every array element can be obtained independently. Also, the impedance distribution is symmetrical, so only half of the impedance values for even

element number arrays are needed. Furthermore, the impedance can be easily achieved by optimizing the coupling through adjusting the dimensions of the open stub line. Compared with traditional approaches, this novel simulation method avoids the repetitive tuning work making the design work more efficient and timesaving.

In this design work, a 6 elements 20dB Dolph-Chebyshev linear array was designed by using this new simulation way. The results show a good radiation performance and it approximately fits with the theoretical result. Since the DRA has lower permittivity value, the 10dB bandwidth is about 13%, much wider than typical arrays which are built by high permittivity DRAs [69]. However, the low permittivity DRA results in high level mutual coupling since more of the fields distribute outside the DRA element. This results in higher SLL values and the radiation pattern is not perfectly symmetrical. This issue can possibly be solved by using the transposed configuration array in the future work.

Chapter 6
Summary and Conclusions

6.1 Summary and conclusions

The motivation of this research is to try to exploit the advantages of the deep XRL fabricated tall microstrip line and combine its special characteristics with the properties of the DRA to drive the development of novel feeding structures to excite low permittivity DRA elements and arrays effectively.

In the course of this thesis, firstly some previous research and the structure fabricated by deep XRL were reviewed.

The properties of the DRA were investigated following by firstly introducing fundamental features of the DRA and its advantages. Since this research work focused on the RDRA, first of all, the isolated DRA model which was driven from the truncated waveguide mode and analyzed by using the traditional electromagnetic analysis was introduced. The expressions of the fundamental mode were represented; besides, the numerical method on how to calculate resonance frequency under the different modes was illustrated. Secondly, different modes and their field distributions as well as the radiation pattern were presented. One example on how to compute the resonance frequency of the RDRA with permittivity of 10 was shown.

The next stage was to exploit the different feeding schemes of the RDRA. Four basic feeding structures: coaxial probe feeding, co-planar slot loop feeding, slot aperture feeding and

microstrip line feeding were analyzed. These analyses were the foundation to build up the connection between the fabricated tall microstrip line and the DRA element.

The deep XRL fabricated tall microstrip line was analyzed. This novel microstrip line was illustrated by comparing to the traditional microstrip line model. The parameters such as the characteristic impedance, propagation constant as well as the phase velocity were analyzed; in addition, the unique electromagnetic characteristic of the tall microstrip line was also illustrated. Through comparing with the conventional microstrip line, the advantages of the tall microstrip line were obvious and three novel feeding structures were proposed naturally by utilizing its special characteristics.

Since the tall microstrip line has the thicker conductor trace, a first feeding structure, side coupling feeding, utilizing the coupling energy from the outer edge of the conductor line to excite the DRA was proposed. A second feeding structure utilizing the fields which are produced at the end of the open tall microstrip line to excite the DRA directly was proposed. The third novel feeding structure which is composed by the T shape open stub line was proposed based on the direct feeding structure. This new feeding scheme not only can excite the DRA effectively with permittivity value as low as 5 but also can change the coupling energy by adjusting the dimension of the open stub line easily, making this feeding scheme apply to design the DRA array easily due to its unique configuration. Since the coupling level is higher than the conventional conductor traces due to the thick feeding structure, all these three feeding structures can be used for exciting the DRA with the low permittivity effectively.

Two experiments for side coupling feeding scheme on exciting low permittivity DRAs (ε_r=10

and ε_r=8) with using tall transmission line were undertaken. Additionally, since the dimensions of the test models were different than the proposed models in the previous simulation, both test models were re-simulated and compared with measurement data. One of the examples uses the DRA with permittivity of 8, which can be fabricated directly by deep XRL process. The simulation and the measurement results show good agreement and further simulation validates the feasibility and effectiveness of the tall transmission line feeding structure proposed.

The last chapter illustrated the theory of the antenna array firstly and introduced a design procedure for a new type of Dolph-Chebyshev array. The 6 elements Dolph-Chebyshev DRA array with 20dB SLL value operating at 24.75GHz was designed by using the T shape novel feeding scheme. Because of the distinguishing features of this tall T shape feeding structure, a new simulation approach was proposed. Comparing with the traditional design method, this new approach related the desired current distribution to an impedance distribution, which could be more directly obtained independently easily by adjusting the dimensions of the open stub line for each array element, enhancing the design efficiency greatly. The example simulation achieves the expected results. The radiation pattern is comparable to the theoretical computation, demonstrating the feasibility of realizing low permittivity DRA arrays with bandwidth much wider than traditional high permittivity DRA arrays.

In conclusion, from analysis and experiments of the novel feeding structures, the advantages and effectiveness of the tall microstrip line which is fabricated by DXRL technology on exciting the low permittivity DRA are outstanding. Since more coupling energy and low loss can be obtained, it can be widely applied into low permittivity DRA array design, making the array have not only

wideband operation but also high gain and high efficiency.

6.2 Further Work

Although this research work accomplishes the desired objectives, there are lots of directions for improvement, discussed as following:

1. There are many suitable microwave materials that can be used in the deep XRL fabrication to exert the benefits for RF design, especially in the microwave area due to the smaller size. The permittivity value of the substrate can be reduced or increased by selecting the appropriate material. However, this action will result in many issues not only bringing the difficulties during the fabrication process but also impacting the RF performance. For example, the higher permittivity value of the substrate will result in the lower characteristic impedance and confine the field inside the substrate area, lowering the coupling level to the DRA element. However, if the permittivity value of the substrate is very low, although it can be applied to the wide band structure, the impact which results from the surface wave could become more serious, and especially when this material is applied to array design, the radiation pattern will be disturbed. The EBG approach could be applied to reducing this effect in such a situation and can enhance antenna efficiency [70].

In addition, the conductor material also can be replaced by the other materials, such as copper. However, it requires further development to improve the electroplating yield.

2. The advantages of these tall microstrip line novel feeding schemes can be seen from the simulation results. However, only one application cannot exhibit the benefits of the taller

microstrip line and its unique features. For example, through adjusting the distance between the DRA and the feeding line, the side coupling feeding structure can also be applied into the array design which is similar as the array design in [69]. Since the tall feeding line can supply more couplings than the normal microstrip line, the wide band antenna array is expected.

Furthermore, the direct feeding scheme can be used into the corporate feeding linear array design due to its special structure. By adjusting the width or the height of the tall microstrip line, the current amplitude can be assigned intentionally, producing the different radiation pattern [71]; besides, the radiation efficiency and the bandwidth can be enhanced due to the low loss comparing with the corporate array which was made by the normal microstrip line [27]. These examples might exemplify the advantages of the deep XRL on RF device design and will be exploited further.

3. In this research work, 20dB 6 elements Dolph-Chebyshev DRA array was designed and the simulation results have shown good radiation pattern and the RF performance, indicating the T shape feeding structure was very effective on exciting the DRA with the low permittivity value. However, the radiation pattern has a little distortion which resulted from suboptimal phasing of the excitation due to the high level mutual coupling between the array elements [27]. This issue can be improved through two approaches. The first one is using the DRA elements with higher permittivity value [69]. Since the fields will be better confined inside of the resonator, the mutual coupling can be reduced, producing the better radiation pattern. Besides, since the high permittivity material DRA is applied, the height of the tall microstrip line can be decreased; easing the fabrication work, but bandwidth would be narrower than presented here. The

alternative way is using the array with transposed configuration [72] to increase the distance between each element in the array. The design work in [73] has already shown the bandwidth can be improved as well as reducing mutual coupling between each DRA element in the array.

REFERENCES

[1] A. Petosa and A. Ittipiboon, “Dielectric Resonator Antennas: A Historical Review and the Current State of the Art”, IEEE Antennas and Propagation Magazine, Vol. 52, No. 5, pp. 91-116, Oct. 2010.

[2] J-W Baik, S-M Han, C Jeong, J Jeong, and Y-S Kim, “Compact Ultra-Wideband Bandpass Filter with EBG Structure”, IEEE Microwave and Wireless Components Letters, Vol. 18, No. 10, pp. 671-673, Oct. 2008.

[3] H. Issa, J-M. Duchamp, S. Abou-Chahine, and P. Ferrari, “Loaded Miniature Transmission Lines Compatible with Low Cost Substrates: Q-Factor Improvement”, Proceedings of the 40th European Microwave Conference, pp. 1218-1221, Sep. 2010, Paris, France.

[4] F. X. Huang, S. Fouladi, and R. R. Mansour, “High- Q Tunable Dielectric Resonator Filters Using MEMS Technology”, IEEE Transaction on Microwave Theory and Techniques, Vol. 59, No. 12, pp. 3401-3409, Dec. 2011.

[5] A. A. Kachayev, D. M. Klymyshyn, S. Achenbach, V. Saile, “High Vertical Aspect Ratio LIGA Microwave 3-dB Coupler”, 2003 International Conference on MEMS, NANO, and Smart Systems, pp. 38-43, Jul. 2003, Banff, Canada.

[6] H. C. Jayatilaka and D. M. Klymyshyn, “Half Wavelength Open Loop Bandpass Filters with Transmission Zeros”, Proc. 19th Asia-Pacific Microwave Conference (APMC 2007), pp. 2213-2217, Dec. 2007, Bangkok, Thailand.

[7] S. Achenbach, D. Klymyshyn, D. Haluzan, T. Mappes, G. Wells, and J. Mohr, “Fabrication of

RF MEMS variable capacitors by deep X-ray lithography and electroplating", Microsystem Technologies, Vol. 13, No. 3- 4, pp. 343, Jun. 2007.

[8] A. Rashidian, D. M. Klymyshyn, M. T. Aligodarz, M. Boerner, J. Mohr, "SU-8 Resonator Antenna", Antennas and Propagation Society International Symposium (APS/URSI), 2010 IEEE, July. 2010, Toronto, Canada.

[9] Ma, Z., D. M. Klymyshyn, S. Achenbach, M. Börner, N. Dambrowsky, "An Ultra-Deep High-Q Microwave Cavity Resonator Fabricated using Deep X-Ray Lithography", IEICE Transactions on Electronics, E90-C, pp. 2192-2197, 2007.

[10] W. Menz, J. Mohr, O. Paul, Microsystem Technology, WILEY-VCH Verlag GmbH, 2001.

[11] R. Zauner, "Micro powder injection molding", Microelectronic Engineering, No. 83, pp. 1442-44, 2006.

[12] A. Rashidian, "Photoresist-based Polymer Resonator Antennas (PRAS) with Lithographic Fabrication and Dielectric Resonator Antennas (DRAS) with Improved Performance", Ph.D thesis, University of Saskatchewan, 2010.

[13] Z. Ma, "LIGA Cavity Resonators and Filters for Microwave and Millimeter-wave Applications", Ph.D thesis, University of Saskatchewan, 2007.

[14] A. Rashidian, D. M. Klymyshyn, M. Boerner, and J. Mohr, "Deep X-ray Lithography Processing for Batch Fabrication of Thick Polymer-based Antenna Structures", Journal of Micromechanics and Microengineering, vol. 20, pp.11, Feb. 2010.

[15] A. Rashidian, D. M. Klymyshyn, M. T. Aligodarz, M. Boerner, J. Mohr, "Photoresist-based Polymer Resonator Antennas: Lithography Fabrication, Strip-fed Excitation, and Multimode

Operation", IEEE Antennas and Propagation Magazine, No. 53, pp. 16-27, 2011.

[16] A. Rashidian, D. M. Klymyshyn, M. T. Aligodarz, M. Boerner, J. Mohr, "Development of Polymer-based Dielectric Resonator Antennas for Millimeter-wave Applications", Progress In Electromagnetics Research (PIER C), No. 13, pp. 203-216, 2010.

[17] A. Rashidian, D. M. Klymyshyn, "On the Two Segmented and High Aspect Ratio Rectangular Dielectric Resonator Antennas for Bandwidth Enhancement and Miniaturization", IEEE Transactions on Antennas and Propagation, No. 57, pp. 2775-2780, 2009

[18] A. Rashidian, D. M. Klymyshyn, "Microstrip-fed high aspect ratio dielectric resonator antenna with dual-resonance broadband characteristics", IET Electronics Letters, No. 45, pp. 94-95, 2009

[19] M. J. Madou, "Fundamentals of Microfabrication: The Science of Miniaturization", CRC Press, Mar. 2002.

[20] E. Becker, W. Ehrfeld, D. Munchmeyer, H. Betz, A. Heuberger, S. Pongratz,W. Glashauser, H. Michel, and R. von Siemens, "Production of separation-nozzle systems for uranium enrichment by a combination of X-ray lithography and galvanoplastics", Naturwissenschaften, Vol. 69, No. 11, pp. 520- 523, 1982.

[21] E. Becker, W. Ehrfeld, P. Hagmann, A. Maner, and D. Munchmeyer, "Fabrication of Microstructures with High Aspect Ratios and Great Structural Heights by Synchrotron Radiation Lithography, Galvanoforming, and Plastic Moulding (LIGA process)", Microelectronic Engineering, Vol. 4, No. 1, pp. 35-56, 1986.

[22] H. Guckel, "High-Aspect-Ratio Micromachining Via Deep X-Ray Lithography",

Proceedings of the IEEE, Vol. 86, No. 8, pp. 1586-1593, August. 1998.

[23] S. Achenbach, “Optimization of the Process Conditions for the Fabrication of Microstructures by Ultra Deep X-ray Lithography (UDXRL)”, PhD thesis, Forschungszentrum Karlsruhe, Karlsruhe, Germany, 2000.

[24] F. Pantenburg and J. Mohr, “Influence of Secondary Effects on the Structure Quality in Deep X-ray Lithography”, Nuclear Instruments and Methods in Physics Research, Vol. B 97, pp. 551-556, 1995.

[25] T. L. Willke, S. S. Gearhart, “LIGA Micromachined Planar Transmission Line and Filter”, IEEE Trans on Microwave Theory and Technique, Vol. 45, No. 10, pp. 1681-1688, Oct. 1997.

[26] D. M. Klymyshyn, H. C. Jayatilaka, M Börner, H. Mohr, “High Aspect-Ratio Coplanar Waveguide Wideband Bandpass Filter With Compact Unit Cells”, IEEE Transaction On Microwave Theory and Techniques, Vol. 57, No. 11, pp. 2752-2760, Nov. 2009.

[27] A. Petosa, “Dielectric Resonator Antenna Handbook”, Artech House, Boston, 2007.

[28] T. H. Chang, J. F. Kiang, “Dualband Split Dielectric Resonator Antenna”, IEEE Transactions on Antennas and Propagation, Vol. 55, No. 11, pp. 3155-3162, Nov. 2007.

[29] S. Ghosh, A. Chakrabarty, “Ultrawideband Performance of Dielectric Loaded T-Shaped Monopole Transmit and Receive Antenna/EMI Sensor”, IEEE Antennas and Wireless Propagation Letters, Vol. 7, pp. 368-361, 2008.

[30] A. Buerkle, K. Sarabandi, H. Mosallaei, “Compact Slot and Dielectric Resonator Antenna with Dual-Resonance, Broadband Characteristics”, IEEE Transaction on Antennas and Propagation, Vol. 53, No. 3, pp. 1020-1027, Mar. 2005.

[31] T. H. Chang, Y. C. Huang, W. F. Su, and J. F. Kiang, “Wideband Dielectric Resonator Antenna With a Tunnel”, IEEE Antennas and Wireless Propagation Letters, Vol. 7, pp. 275-278, 2008.

[32] K. M. Luk and K.W. Leung (eds.), “Dielectric Resonator Antennas”, Baldock, England, Research Studies Press, 2003.

[33] S. A. Long, M. W. McAllister and L. C. Shen, “The resonant cylindrical dielectric cavity antenna”, IEEE Transaction on Antennas and Propagation, Vol. 31, pp. 406-412, May 1983.

[34] M. W. McAllister and S. A. Long, “Rectangular Dielectric Resonator Antenna”, IEE Electronics Letters, Vol. 19, pp. 218-219, Mar. 1983.

[35] M. W. McAllister and S. A. Long, "Resonant Hemispherical Dielectric Antenna", IEE Electronics Letters, Vol.20, pp. 657-659, Aug. 1984.

[36] R. K. Mongia, A. Ittipiboon, “Theoretical and Experimental Investigations on Rectangular Dielectric Resonator Antennas”, IEEE Transactions on Antennas and Propagation, Vol. 45, No. 9, pp. 1348-1356, Sep. 1997.

[37] R. K. Mongia, “Theoretical and Experimental Resonant Frequencies of Rectangular Dielectric Resonators”, Microwaves, Antennas and Propagation, IEE Proceedings H, Vol. 139, pp. 98-104, Feb. 1992.

[38] A. K. Okaya and L. F. Barash, “The Dielectric Microwave Resonator”, Progress In Electromagnetics Research, Vol. 50, pp. 2081-2092, Oct. 1962.

[39] D. M. Pozar, “Microwave Engineering”, Third Edition, John Wiley & Sons, Inc. 2005.

[40] T. Itoh, “Numerical Techniques for Microwave and Millimeter-Wave Passive Structures”,

John Wiley and Sons, 1989.

[41] K. J. Binns and P. J. Lawrenson, “Analysis and Computation of Electric and Magnetic Field Problems”, Pergamon Press, Oxford, 1973.

[42] R. E. Collin, “Foundations for Microwave Engineering”, New York: McGraw Hill, 1966.

[43] D. Guha, Y. M. M. Antar, A. Ittipiboon, A. Petosa, and D. Lee, “Improved Design Guidelines for the Ultra Wideband Monopole Dielectric Resonator Antenna”, IEEE Antennas and Wireless Propagation Letters, Vol. 5, pp. 373 – 376, Dec. 2006.

[44] K. M. Luk, M. T. Lee, K. W. Leung and E. K. N. Yung, “Technique for Improving Coupling between Microstrip Line and Dielectric Resonator Antenna”, IEEE Electronics Letters, Vol. 35, No. 5, pp. 357-358, Mar. 1999.

[45] Y. Gao, B. L. Ooi, W. B. Ewe, and A. P. Popov, “A Compact Wideband Hybrid Dielectric Resonator Antenna”, IEEE Microwave and Wireless Components Letters, Vol. 16, No. 4, pp. 227-229. Apr. 2006.

[46] R. Kranenberg, S. A. Long and J. T. Williams, “Coplanar Waveguide Excitation of Dielectric-Resonator Antennas”, IEEE Transactions on Antennas and Propagation, Vol. 39, pp. 119-122. Jan. 1999.

[47] S.M, Deng, et al., “CPW-Fed Ceramic Dielectric Resonator Antennas with High Profile”, IEEE Antennas & Propagation Symposium Digest AP-S 2004, Vol. 1, pp. 1098-1101, Monterey CA.

[48] M. S. Al Salameh, Y. M. M. Antar, and G. Seguin, “Coplanar-Waveguide-Fed Slot-Coupled Rectangular Dielectric Resonator Antenna”, IEEE Transactions on Antennas & Propagation, Vol.

50, No. 10, pp. 1415-1419, Oct. 2002.

[49] I. Eshrah, A. A. Kishk, “Theory and Implementation of a Dielectric Resonator Antenna Excited by a Waveguide Slot”, IEEE Transactions on Antenna and Propagation, Vol. 53, No. 1, pp. 483-494, Jan. 2005.

[50] K. W. Leung, and K. K. So, “Rectangular Waveguide Excitation of Dielectric Resonator Antenna”, IEEE Transactions on Antenna and Propagation, Vol. 51, No. 9, pp. 2477-2481, Sep. 2003.

[51] R. A. Kranenburg, and S. A. Long, “Microstrip Transmission Line Excitation of Dielectric Resonator Antennas”, IEE Electronics Letters, Vol. 24, No. 18, pp. 1156-1157, Sep. 1988.

[52] R. K. Mongia, P. Bhartia, “Dielectric Resonator Antennas - A Review and General Design Relations for Resonant Frequency and Bandwidth”, International Journal of Microwave and Millimeter-Wave Computer-Aided Engineering, Vol. 4, Issue 3, pp. 230–247, July. 1994.

[53] I. J. Bahl and D. K. Trivedi, “A Designer’s Guide to Microstrip Line”, Microwaves, pp. 174-182, May. 1977.

[54] M. Schneider, “Microstrip Lines for Microwave Integrated Circuits”, Bell System Technical Journal, pp. 1421-1444, May-June. 1969.

[55] M. A. R. Gunston and J. R. Weale, “Variation of Microstrip Impedance with Strip Thickness”, IEEE Electronics Letters, Vol. 5, pp. 697-698, Dec. 1969.

[56] H. A. Wheeler, “Transmission-Line Properties of a Strip on a Dielectric Sheet on a Plane”, IEEE Transactions on Microwave Theory & Techniques, Vol. 25, No. 8, pp. 631-647, Aug. 1977.

[57] L. G. Maloratsky, “Reviewing the Basics of Microstrip Lines”, Microwaves & RF, March. 2000.

[58] “Ansoft HFSS^{TM} 8.5 Advanced Tutorial on Port Setting”.

[59] “Ansoft HFSS^{TM} 9.1 reference manual”.

[60] “Ansoft HFSS^{TM} 10 User Guide”.

[61] G. D. Makwana, D. Ghodgaonkar, “Wideband Stacked Rectangular Dielectric Resonator Antenna at 5.2 GHz”, International Journal of Electromagnetics and Applications, pp. 41-45, 2012.

[62] M. Saed and R. Yadla, “Microstrip-fed Low Profile and Compact Dielectric Resonator Antennas”, Progress In Electromagnetics Research, PIER 56, pp. 151–162, 2006.

[63] G. Bit-Babik, C. Di Nallo, and A. Faraone, “Multimode dielectric resonator antenna of very high permittivity”, IEEE Antennas and Propagation Society International Symposium, Vol. 2, pp. 1383-1386, June. 2004.

[64] C. A. Balanis, “Antenna Theory: Analysis and Design”, Third Edition, New York, 2005.

[65] W. L. Stutzman, G. A. Thiele, “Antenna Theory and Design”, 2nd Edition, Wiley, 1997.

[66] C. L. Dolph, “A Current Distribution for Broadside Arrays Which Optimizes the Relationship Between Beamwidth and Side-Lobe Level”, Progress In Electromagnetics Research, PIER, pp. 335-348, June. 1946.

[67] R. Garg, P. Bhartia, I. Bahl, A. Ittipiboon, “Microstrip Antenna Design Handbook”, Chap 12，Artech House, 2001.

[68] M. J. Ehrlich, “Slot-antenna array”, in Jasik, H.(Ed.): “Antenna Engineering Handbook”,

Chap.9, McGraw-Hill, New York.

[69] A. Petosa, R. K. Mongia, A. Ittipiboon, J. S. Wight, “Design of Microstirp-fed Series Array of Dielectric Resonator Antennas”, Electronics Letters 3rd, Vol. 31, No. 16, pp. 1306-1307, Aug 1995.

[70] M. N. Aktar, M. S. Uddin, “Enhanced Gain and Bandwidth of Patch Antenna using EBG Substrates”, International Journal of Wireless & Mobile Networks, Vol. 3, No. 1, pp. 62-69, Feb 2011.

[71] A. Petosa, R. Larose, A. Ittipiboon, and M . Cuhaci, “Microstrip-Fed Array of Multisegment Dielectric Resonator Antennas”, IEE Proceedings on Microwaves, Antennas, and Propagation, Vol. 144, No. 6, pp. 472-476, Dec. 1997.

[72] R. P. Owens, “Microstrip Antenna Feeds”, in Handbook of Microstrip Antennas, Vol. 2, J. R. James and P. S. Hall(Eds.), Peter Peregrinus, London, UK, 1989.

[73] A. Petosa, A. Iittipiboon, M. Cuhaci, and R. Larose, “Bandwidth Improvement for a Microstrip-Fed Series Array of Dielectric Resonator Antennas”, IEE Electronics Letters, Vol. 32, No.7, pp. 608-609, Mar .1996.

[74] D. M. Klymyshyn, M. Boerner, D. Haluzan, E. G. Santosa, M. Schaffer, S. Achenbach, and J. Mohr, “Vertical High-Q RF-MEMS Devices for Reactive Lumped Element Circuits”, IEEE Transactions on Microwave Theory and Techniques, Vol. 58, No. 11, pp. 2976-2986, 2010.

[75] B. Ghosh, et al., “CPW Feed to Rectangular DRA”, Microwave and Optical Technology Letters, Vol. 5, No. 3, pp. 210-216, May. 2005.

[76] http://www.ntktech.com/product_detail.asp?productid=91

Appendix A

The general fabrication processes for both types of structures is introduced as following.

The first step for fabricating metal structures is coating a thin metal film on the substrate as shown in Fig. A.1(a). The substrate can be of different materials, such as quartz, silicon, and alumina. This thin film is known as the seed layer and serves as a plating base for later electroplating. In addition, this thin layer can reduce or even avoid the stress which is introduced by the thermal expansion after coating the resist on the seed layer in the next step or by the polymerization step. This stress may result in cracking the resist after development.

The second step is applying the photoresist on the "seed layer". For deep XRL technology, there are two types of photoresist for different purposes: positive photoresist and negative photoresist. The differences between them are after exposure under the X-ray radiation, the negative photoresist becomes hard and difficult to dissolve in a suitable developer, while the property of the positive resist is the reverse of the negative photoresist; the exposed areas get soluble in the developer. SU-8^{TM} and Polymethylmethacrylate (PMMA) are two examples of common negative and positive photoresists respectively.

In the resist step, the traditional way is using the spin coating method to spread resist layer on the substrate uniformly. Unfortunately, this process is not suitable for the thick resist layer because the intrinsic stress will increase with increasing the thickness of the resist layer. This stress may result in a non-uniform penetration of the developer into the resist layer and cracking the resist layer [10]. In this research, the solid polymethylmethacrylate (PMMA) is used as the resist layer.

It is either polymerized directly onto the substrate or the polymerized PMMA plate is glued onto the substrate. One of the approaches is using the thin monomer layer which contains adhesion conductive components to spread onto the substrate and then the polymerized PMMA resist layer is glued on this thin adhesion layer by using the pressure, bonding the resist layer with the substrate (Fig. A.1(b)) .

After the resist preparation, the resist plate which is covered by the mask with the object pattern will be put under the collimated high-energy X-ray radiation exposure. Since the PMMA is sensitivity to the X-ray source, the photons with high energy will break the molecule chains of photoresist in the exposed region. After exposure, the patterns on the mask will transfer to the PMMA resist. This process is shown in Fig. A.1(c).

The following step is development. The exposed PMMA resist layer can be dissolved by some special organic developer easily since its long molecular chain is broken during this process. Once the irradiated parts are removed as shown in Fig. A.1(d) after the development process, the new 3-dimensional resist plate will be formed and used as the electroplating mold. The metal such as copper, nickel or gold is deposited in the void space forming the structure of the target object. Finally the remaining photoresist will be removed by the X-ray flood irradiation which is one more step of photoresist development. The revealed “seed layer” will be removed by using hydrofluoric (HF) acid and reactive ion etching (RIE), finally forming the target object. The last two steps are presented in Fig. A.1(e)&(f).

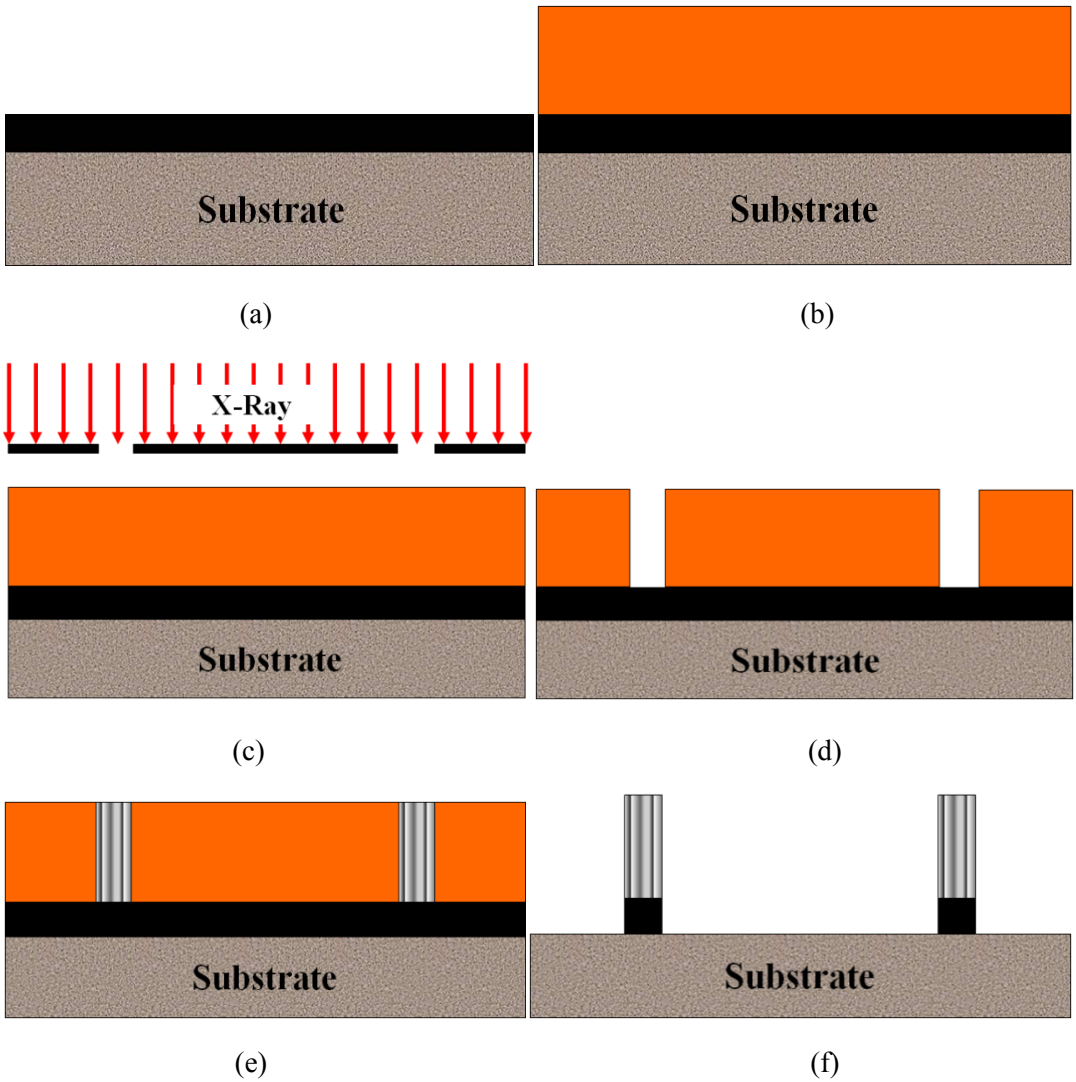

Fig. A.1 Deep XRL Process for fabrication of metal structures:

(a) Coating the "seed layer" on the substrate

(b) Application of the photoresist on the "seed layer"

(c) X-Ray exposure

(d) Photoresist development (positive photoresist)

(e) Metal deposition by Electroplating

(f) Removal of photoresist and seed layer

For ceramic fabrication, one of the common fabrication methods is referred as micro powder injection molding [11]. Different than the metal structure fabrication, this way needs the

sacrificial plastic to mold the target object, facilitating the fabrication processes. It includes three main steps [12]. The first step is deep X-ray lithography which is similar as procedures in Fig. A.1(a)~(c) of metal structure. However, the differences between them are the PMMA will be used as the sacrificial layer and it will be removed after molding the object structure; furthermore, the inversed structure to the PMMA frame can be produced after development as shown in Fig. A.2(a) by using the opposite tone resist. Additionally, a thin carbon layer will be sputtered on the substrate rather than a thin metallic layer in the first step. Since the low adhesion of this carbon layer, the final structure can be released by gently bending the silicon substrate.

In the second step, a composite of SU-8 and alumina micro powder is injected into the PMMA frame in Fig. A.2(b). After the soft baking process, the structure is flood exposed under the X-ray in Fig. A.2(c). The PMMA mold can be removed by using the GG developer in Fig. A.2(d), since the long molecular chains of PMMA are broken down, making it soluble to developer. Finally, the final structure will be released from the carbon layer and shown in Fig. A.2(e). [12] shows some dielectric structures using this fabrication method.

Since the synchrotron X-ray source will be utilized as the lithographic light source, there are many advantages that can be offered. For example, very high patterning resolution can be obtained due to the short wavelength of the X-ray photons. Structures in polymer photoresists with lateral dimension from several micrometers to centimeters, and moreover, the well collimated X-ray beams can achieve high quality structure transferring from the mask. Vertical structures with aspect ratios of up to 100 and optical quality sidewall surface roughness (typically 20 to 30nm) can be achieved [13].

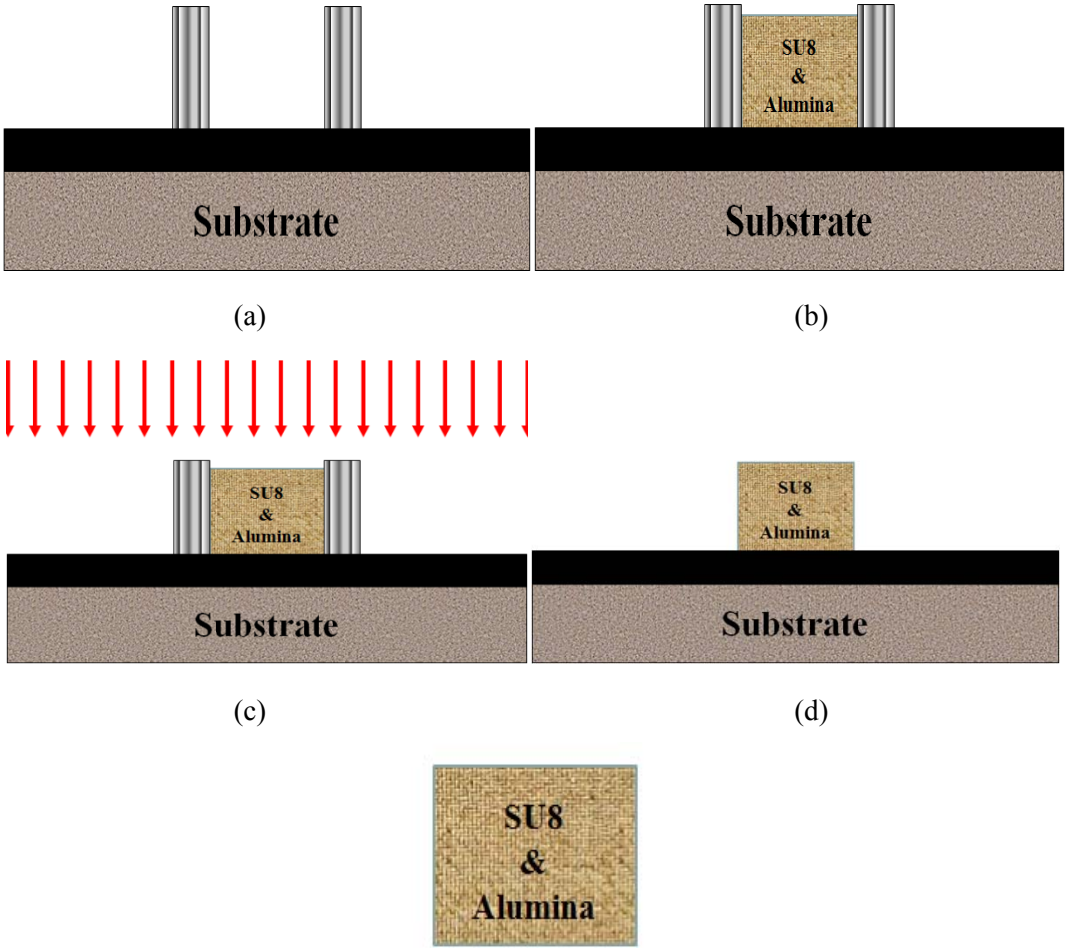

Fig. A.2 Deep XRL process for fabrication ceramic structure

(a) Developed PMMA structure

(b) Fill PMMA frame with SU8&alumina

(c) Flood exposure

(d) Removed PMMA frame

(e) Releasing the final structure by bending the silicon substrate